UNIVERSITY OF OKLAHOMA

GRADUATE COLLEGE

BARITE SAG UNDER DYNAMIC AND ELEVATED TEMPERATURE CONDITIONS: EXPERIMENTAL STUDIES AND MATHEMATICAL MODELING

A DISSERTATION

SUBMITTED TO THE GRADUATE FACULTY

in partial fulfilment of the requirements for the

Degree of

DOCTOR OF PHILOSOPHY

By

MUILI FEYISITAN FAKOYA
Norman, Oklahoma
2019

BARITE SAG UNDER DYNAMIC AND ELEVATED TEMPERATURE CONDITIONS: EXPERIMENTAL STUDIES AND MATHEMATICAL MODELING

A DISSERTATION APPROVED FOR THE
MEWBOURNE SCHOOL OF PETROLEUM AND GEOLOGICAL ENGINEERING

BY

Dr. Ramadan Ahmed, Chair

Dr. Harold Stalford

Dr. Subhash Shah

Dr. Catalin Teodoriu

Dr. Saeed Salehi

Dedication

To God who makes a Way
(Isaiah 43:19)

Acknowledgements

A heartfelt expression of gratitude goes to my advisor and doctoral-committee chair, Dr. Ramadan Ahmed, for the support and high-quality mentorship he afforded me throughout my Ph.D. program at The University of Oklahoma. His availability for research discussions, and provision of insightful suggestions are deeply appreciated. I am thankful to Dr. Harold Stalford, my outside doctoral-committee member, for his contribution towards the success of my study. I would like to say thank you to Dr. Subhash Shah for serving as a member on my doctoral committee, and for the support and research training I received from him during my M.S. program in Petroleum Engineering at The University of Oklahoma. Though, I have successfully completed this M.S. program since 2012; but, the experience of that journey is still helpful. Also, it laid the strong foundation for my Ph.D. program. I am thankful to Dr. Catalin Teodoriu and Dr. Saeed Salehi for serving as members on my doctoral committee. Your time and comments are pivotal to the success of this research.

I would like to say thank you to the Faculty and Staff of the Mewbourne School of Petroleum and Geological Engineering (MPGE). Special thanks to Sonya Grant for her continuous assistance, and interest in my well-being and that of my family. Many thanks to Dr. Deepak Devegowda, Dr. Mashhad Fahes, Dr. Ali Tinni, Gary Stowe, and Danika Hines-Barnett. I am thankful to Jeff McCaskill for his help regarding my experimental setups at the Well Construction Technology Center (WCTC). Also, I appreciate all the researchers at WCTC.

The absolute support and understanding of my lovely wife, Saratu Fakoya, are outstanding, and for these, I say thank you very much. To our great daughters, Flourish M. Fakoya and Moyinoluwa F. Fakoya, daddy says thank you. The Ph.D. journey was demanding, but we made it together only by the grace of God. I deeply appreciate my mother, Abosede

Fakoya, for her love, support, and prayers. Also, my profound gratitude goes to my sisters (Nike Toki, Kemi Ojediran, and Wemimo Jayeoba) and their husbands, my brother (Kunle Fakoya) and his wife (Agnes Fakoya), and my nieces and nephews. My wife's family are not left out; I thank you all.

I would like to say thank you to Dr. Tayo Omosebi, Kolapo Asafa, Dr. Seyi Ogunsola, Afolabi Igandan, Femi Lawson, Dr. Chukwudi Chukwudozie, Dipo Odutayo, Christian Olotu, Lanre Aboaba, Dele Adediji, Yinka Solaru, Ojuewa Solaru, Dare Adedokun, Lekan Ogunbanwo, Segun Babalola, Eghosa Ebohon-Ero, Joshua Ukaps, Stephen Ekwunife, Raphael Adebusoye, Gadi Ogbogu, Bose Fadayomi, Bankole Aderemi, James Morgan, Dr. Rida Elgaddafi, Dr. Olawale Fajemidupe, Dr. Prince Zogli, Lekan Ajayi, Kachi Ogbonnaya, Dr. Lekan Seriki, Seyi Fadipe, Dr. Uvirkaa Akumaga, Tobi Olorunsola, Dr. Taiwo Omotoso, Tolu Babarinde, Emmanuel Omojuwa, Femi Alademehin, Lekan Shobayo, Tunde Babayemi, Dr. Peter Ezeakacha, Folarin Kolawole, just to name a few. I am thankful to my church family at the Redeemed Christian Church of God (RCCG) Praise Center, the members of RCCG On Campus (ROC), and my friends in Norman.

Table of Contents

List of Tables

List of Figures

Abstract

Barite sag is an undesired occurrence that causes density variation in the wellbore. It is a problem that is related to both fluid property (mainly rheology) and drilling practices, and it arises mostly in invert emulsion muds. Due to the complexity of barite sag, the mechanisms that initiate and exacerbate its occurrence are still not completely understood. Drilling problems such as lost circulation, wellbore instability, and stuck pipe result from this undesired phenomenon. Drilling operations are capital-intensive projects, thus, more solution-driven researches are needed for barite sag minimization.

The objective of this research is to study barite sag from the perspective of particle size, mud rheology, rotational speed, and inclination angle, and also, develop a mathematical model for barite sag predictions. Thus, the investigation includes different experimental approaches (fluid rheology tests and barite sag investigations using rotational viscometer and flow loop) and mathematical modeling.

In order to establish a relationship between barite sag, and shear rate and temperature, experimental investigations were conducted on the rheology of oil-based mud (OBM) and its continuous phase at different shear rates and temperatures. Organophilic clay concentration and the oil-water ratio (OWR) were varied during the investigation. For comparison purposes, the rheology of water-based mud (WBM) was also studied. In rotational viscometer experiments, different barite types were prepared by sieving regular API barite. The prepared barite samples were used to make weighted oil-based muds (OBMs). Then, barite sag investigations were performed by applying the Viscometer Sag Shoe Test (VSST) method at different particle sizes and rotational speeds. The flow loop investigations were conducted to better understand the effects of pipe rotation and inclination angle on barite sag under dynamic condition.

Furthermore, barite sag occurring in a vertical mud column is modeled by adopting the sedimentation-consolidation model. The new model has incorporated the shearing (dynamic) effect and the non-Newtonian behavior of OBM. Model solution was obtained using the fully implicit finite difference method.

The OBMs exhibit shear-thinning behavior that is best fitted with the Herschel-Bulkley model. The outcomes show remarkable trends of apparent viscosity and rheological parameters as temperature, organophilic clay concentration, and OWR increase. Rheological models are developed using nonlinear regression analysis, and reasonable predictions of OBM apparent viscosities are made. The rheological parameters and apparent viscosity of OBM and WBM are normalized, and their comparison shows why OBM is more vulnerable to barite sag events than WBM. The VSST results indicate that barite sag increases with increasing average particle diameter and rotational speed. The normalized mud densities obtained from the flow loop results reveal interesting trends in the top and bottom sections of the mud column as pipe rotational speed and inclination angle increase. The developed barite sag model gives reasonable predictions of the VSST results. Parametric studies show that barite sag will decrease with decreasing particle size, but, will increase as the unweighted OBM rheological parameters decrease.

This research provides a comprehensive approach to study barite sag. The combination of OBM and continuous phase rheology, particle size distribution effect, rotational speed, and inclination angle will facilitate a better understanding of barite sag and minimize its occurrence.

Chapter 1: Introduction

1.1. Overview of Barite Sag

Barite is the main material utilized in the oil and gas industry for drilling mud density increment. However, other weight-materials exist and these include ilmenite and hematite. If certain situations are present, barite particles will settle and amass on the low side of an annular section. This occurrence is called barite sag, and it happens mainly in invert emulsion muds. According to Zamora and Bell (2004), the phenomenon of barite sag is complicated and still not thoroughly understood. Originally, barite sag was comprehended as a problem that happens under a static condition because of the density variation in directional wells after circulation was stopped for a long time (Zamora, 2009). Now, the general agreement is that it occurs predominantly when dynamic conditions are present and the wellbore is in an inclined position.

Barite sag causes bottom hole density fluctuations, and subsequently, it leads to drilling problems such as lost circulation, wellbore instability, and stuck pipe. Lost circulation contributes to operational downtime, thus, an increase in drilling cost is inevitable (Ezeakacha and Salehi, 2019a, 2019b). The accumulation of barite particles caused by sagging is illustrated in Fig. 1.1. Barite settling is a problem that is related to mud properties, wellbore geometry and drilling parameters. The density variation that results from barite sag leads to pressure imbalance and fluctuations in downhole equivalent circulating density (ECD). The record (at the surface) of mud weight during drilling and tripping generally indicates the development of barite settling if variations are noticed in the mud weight profile (Fig. 1.2). A temperature increase results in fluid viscosity reduction, and thus, encourages barite sag (Parvizinia et al., 2011). Besides, high shear rates reduce mud viscosity owing to shear thinning, and the rate of weight-material settling is expected to increase with shear rate. Apart from the settling of heavy solid

particles owing to their weight, the shear that the drilling mud is subjected to may also encourage the detachment of the particles from the drilling mud structure (Parvizinia et al., 2011).

Fig. 1.1: Barite sag solids removed from Well CC (McNerlin and Oakey, 2011)

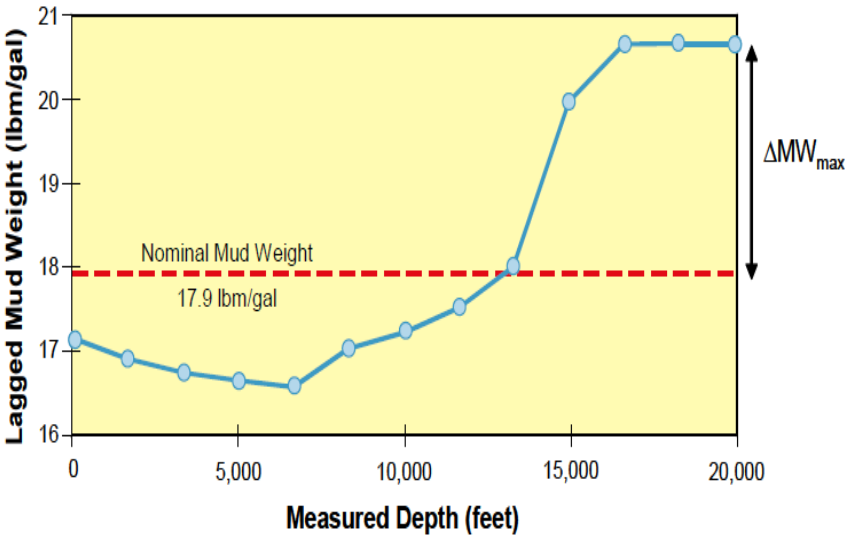

Fig. 1.2: Illustration of surface density profile obtained from bottoms-up data (Bern et al., 2010)

Barite settling should not be misunderstood for a situation where the weight-materials settle in a drilling mud that has an inadequate rheological property, and in a static condition (Hemphill, 2009). Rather, it means the sedimentation of weight-materials in a drilling mud that

has an adequate rheological property. Furthermore, Hemphill (2009) said that a mud with a sufficient rheological property and in a static mode shows little or no settling propensity. Rather, barite settling occurs when low-shear dynamic conditions and inclination angles of 40 – 75° are present. According to Nguyen et al. (2014), the shear caused by low-dynamic events destroys the fluid structure and promotes particle settling. The contribution of dynamic settling is more than that of static settling (Hanson et al., 1990). The circulation of drilling mud, and fluid movements that occur owing to drill pipe, logging tool, and casing are dynamic conditions (Hanson et al., 1990).

Invert emulsions show more vulnerability to settling than water-based drilling muds (Omland et al., 2006; Nguyen, 2009; Fakoya and Ahmed, 2018). According to Tehrani et al. (2004), observations in the oilfields and laboratory examination of barite settling from flow loop data indicate that the seriousness of sagging is worsened in a situation where viscosity and annular velocity are low. The sliding of barite beds occurs at inclination angles in the range of 30 – 60° (Skalle et al., 1999), and mainly at 40 – 50° (Zamora and Jefferson, 1994). The start of sliding is mostly determined by inclination angle, particle size and shape, and wetting of particle surfaces (Skalle et al., 1999).

At low shear rates, weight-material settling is worse; therefore, it is preferable to estimate it at these low shear rates with an instrument that measures mud weight directly (Zamora and Bell, 2004). Additionally, Tehrani et al. (2011) emphasized the need for reliable dynamic measurement techniques since flow loop experiments and oilfield experience have indicated that barite sag occurrences are favored by dynamic conditions.

For the minimization of barite settling, many studies have dwelled on mud rheology (low-shear rheology, gel structure, and viscoelastic characteristics). Many mud additives have

been designed for managing mud rheological characteristics; however, mud viscosity increased when these additives were used (Massam et al., 2004). To restore a mud that has experienced barite sag, circulation and conditioning are usual practices, and these consume a lot of rig time, and obviously, lead to higher cost of drilling (Dye et al., 2001). The attempts to link barite sag to various fluid and drilling parameters have not produced good correlations (Hemphill and Rojas, 2004).

It is easier to reduce barite sag during drilling because mud viscosity, flow rate, and pipe rotation can be increased. But, these options are rarely available during completion operations due to restrictions that come from the setting tools or the equipment that is being installed in the wellbore (McNerlin and Oakey, 2011). Barite sag potential is very high in open hole completion when sand screens are sent downhole in conditioned muds of low densities (McNerlin and Oakey, 2011).

1.2. Statement of Problem

The full extent of the mechanism of barite sag is unknown at the moment because this phenomenon cannot be tied to a single cause. Though, many experimental investigations have been carried out, there are still some disparities. Majority of the experimental works dwelled on mud rheology, and the attempts to correlate different rheological parameters to barite sag have not yielded a generally-acceptable solution. Also, the mechanisms that initiate and exacerbate this problem are still not completely understood. Additionally, a comprehensive approach is not available for barite sag studies. The unavailability of such approach has limited the understanding of barite sag. Logically, the availability of a comprehensive study can spur the development of mud designs that can minimize sagging. Besides, just a few mathematical modeling endeavors are available.

1.3. Research Objectives

The main objective of this research is to understand barite sag, and provide valuable information that would help the oil and gas industry in tackling this problem. The precise objectives are:

- To study the rheology of OBMs at ambient and elevated temperatures, and learn why OBMs are more vulnerable to barite sag than water-based muds (WBMs).
- To understand the effect of particle size distribution on barite sag.
- To understand the effect of rotation on barite sag.
- To understand the effect of mud rheological parameters on barite sag.
- To understand the effect of inclination angle on barite sag.
- To study sag profile under static and dynamic conditions.
- To develop a mathematical model for field and laboratory barite sag predictions, barite sag simulation studies, and development of effective mud formulations.

1.4. Research Methodology

The comprehensive study-approach that is adopted in this investigation is classified into three groups. These are:

- Theoretical Studies: An in-depth literature review has been conducted to learn the oil and gas industry's perspective on barite sag. This has provided the opportunity to study the evolution of barite sag research. The knowledge of the current state of research laid the foundation for the experimental designs and studies, and mathematical modeling that is performed in this investigation.
- Experimental Studies: The laboratory tasks that were performed are rheological tests, particle size analysis, Viscometer Sag Shoe Test (VSST), and flow loop sag testing. The test results are analyzed and discussed.

- Mathematical Modeling: An existing sedimentation-consolidation model has been adopted to analyze barite sag. A solution for the model is obtained numerically using the fully implicit finite difference method. The numerical solution is implemented in MATLAB program and results are verified by previously published results. Barite particle properties, shear rate, and mud rheological parameters are incorporated into the model through settling velocity calculations. The adapted model gave reasonable predictions of barite sag when compared with experimental measurements.

1.5. Scope of Study

In this study, the rheological behaviors of OBMs and WBMs, and barite sag were investigated. In studying rheological behaviors of the muds, OBMs were prepared with different organophilic clay concentrations of 2.9, 8.6, and 17.1 g/L. Three oil-water ratios (65/35, 75/25, and 85/15) were considered. For the preparation of WBMs, bentonite concentrations of 71.3 and 79.9 g/L were used. Rheological measurements were conducted at temperature and shear rate ranges of 24 – 87°C and 5.11 – 1021.8 s^{-1}, respectively, except for WBMs that had a temperature range of 24 – 66°C. In order to study barite sag, the VSST and flow loop approaches were utilized. The VSST studies were performed (at 49°C) with weighted OBMs prepared with organophilic clay concentration of 8.6 g/L, OWR of 75/25, and barite concentration of 736.5 g/L. Three barite types with different particle sizes (45, 63, and 82 μm average particle diameters) were used. Additionally, rotational speeds of 1, 10, and 100 rpm were used in the VSST studies. Using mud formulation used in the VSST investigation and regular barite particles (82 μm average particle diameter), additional sag studies were conducted (at 49°C) in a flow loop at different pipe rotational speeds (0 and 46 rpm) and inclination angles (0, 25, and 50°).

Chapter 2: Literature Review

2.1. Overview

Over the years, barite sag investigations have been performed to better understand its mechanisms and establish predictive models. It is important to comprehend the behavior of fluid medium in which a particle settles. Therefore, this review starts with the discussion of oil-based drilling fluids. Then, the mechanisms of barite settling in a vertical and inclined fluid column are presented. The fundamental concept of barite settling in sheared non-Newtonian fluid is discussed. Also, the various sag measurement techniques that are used in the laboratory and the field are examined. Mainly, barite sag happens under dynamic conditions and it occurs due to combinations of factors (mud rheology, particle characteristics, and drilling operational parameters). Thus, the effects of these factors on particle settling are reviewed. The occurrence of barite settling is undesirable, therefore, the various ways to detect, mitigate, and remediate it are explored. Lastly, the study of sag modeling is presented.

2.2. Oil-Based Muds

When two immiscible fluids are mixed, emulsions are created (Jha et al., 2014). They are used in many industries such as pharmaceutical, paint, food, cosmetic, and petroleum. Generally, emulsions are grouped into oil-in-water (O/W) and water-in-oil (W/O) emulsions. For O/W emulsions, the oil droplets form the dispersed (or internal) phase while the water represents the continuous (or external) phase. On the other hand, the water droplets create the dispersed phase in W/O emulsions while the oil represents the continuous phase. A W/O emulsion can also be called an invert emulsion. The kind and quantity of surfactants and surface-active solids facilitates emulsion stability (Smith and Arnold, 1987).

Based on the structure of emulsion systems, Tadros (2013) stated that the following groupings can be made: macroemulsions (size range: 0.1 – 5 μm), microemulsions, nanoemulsions (size range: 20 – 100 nm), double and multiple emulsions (these are emulsions-of-emulsions), and mixed emulsions (the presence of two immiscible dispersed phases in a continuous medium).

According to Ihenacho et al. (2016), the type of drilling fluid to be used affects the success of drilling and completion program implementations. Today, invert emulsions are frequently used in the petroleum industry owing to their outstanding performance, especially at high pressure and high temperature (HPHT) conditions and in highly sensitive shale formations. In the presence of formation fluids, invert emulsions show more stability in their properties compared to WBMs. Also, they provide a superior lubricity and promote wellbore stability (Caenn and Cillingar, 1996). Invert emulsions ensure a high rate of penetration when drilling through shale formations (Wagle et al., 2012). Many offshore wells now have high lateral displacements for the purpose of maximizing the reservoir drainage area. However, the adequate shale inhibition and lubrication needed in these wells cannot be delivered by WBMs. The use of OBMs, in these instances, has been effective in facilitating the safe and economic achievement of well targets (McKee et al., 1995). Petroleum products such as mineral oil and diesel serve as the base fluids for the preparation of OBM (Growcock et al., 1994).

In the work of Ackerson (1990), high concentration of solid suspensions were investigated. These solid suspensions exhibited a crystalline structure that are solid-like in nature. In complex fluids, colloidal particles are organized into crystals (Gast and Russel, 1998). There is a difference in the process of gel development in WBM and OBM. In WBM, gelling develops in the presence of static condition owing to different natural occurrences (such as

polymer-polymer and polymer-solid entanglements, electrical double layer forces, and electrical charge on the surface of polymers. In OBM, the formation of invert-emulsion structure was reported by Saasen (2002). The structure appeared as gel formation and yielding at very small shear rates.

Invert emulsions prepared with non-aromatic base oils are less hostile to the environment than synthetic-based muds (SBMs). However, the environment has more tolerance for synthetic-based mud (SBM) compared to OBM (Saasen et al., 2001). The application of biodiesel as a possible base oil for preparing a cheap and environmentally friendly drilling fluid was researched by Li et al. (2016). SBM finds a wider usage than OBM; however, OBM gives superior results at elevated temperatures. Growcock and Frederick (1996) investigated the characteristics of SBMs and their base fluids, and also, made a comparison with OBMs and Low-Toxicity Mineral Oils (LTMOs). In comparison to SBM, the better performance of OBM at higher temperatures was revealed. Surprisingly, the base fluids of many SBM show superior viscosity values compared to the base fluids of OBM at ambient temperature; nonetheless, they thin faster as temperature rises.

The invert emulsions applied in drilling operations are often non-Newtonian fluids, and they exhibit strong shear thinning and yielding behavior. When a shearing force is applied on these fluids, they will not flow until the yield stress is exceeded. In drilling operations, pressure drop in the pipe and annulus, suspension and transportation of cuttings, and fluid loss are affected by drilling fluid rheology (Tehrani, 2007).

2.2.1. Rheological Models

The rheology of emulsions has been a popular topic for a long time because of its wide usage in many industries. The description of their rheological properties is complex due to different factors. Some of the factors are size and shape of the dispersed phase, concentration, effect of

shearing on the dispersed phase, and continuous phase viscosity under temperature and pressure conditions. Different rheological models have been developed for emulsions and invert emulsions.

2.2.1.1. Newtonian Models

Einstein (1906) showed that the size of rigid spherical molecules, in a dilute suspension, can be found from the viscosities of the suspension and pure solvent. His studies involved the motion of fluid that contained some suspended spherical molecules. The solution of mechanics of the fluid motion resulted in:

$$\eta_s = \eta_o(1 + 2.5\phi_d) \quad (2.1)$$

where η_s is suspension viscosity; η_o is continuous phase viscosity; ϕ_d is volume fraction of the dispersed phase.

Equation 2.1 can be expressed in another form.

$$\eta_r = 1 + 2.5\phi_d \quad (2.2)$$

where $\eta_r = \eta_s/\eta_o$ = relative viscosity.

This equation can be adopted for emulsion, if the dispersed solid molecules are replaced with liquid droplets. This was the extension Taylor (1932) made to the work of Einstein (1906) when he derived a mathematical expression for the rheology of dilute emulsions. His derivation includes the velocity equations of Lamb (1895) that are developed for the slow motion of viscous fluids. The final expression that describes the rheology of dilute emulsions (Taylor, 1932) is:

$$\eta_s = \eta_o\left[1 + 2.5\phi_d\left(\frac{\eta_{ld}+\frac{2}{5}\eta_o}{\eta_{ld}+\eta_o}\right)\right] \quad (2.3)$$

where η_{ld} is viscosity of the liquid drops (or dispersed phase).

If $\eta_{ld} >> \eta_o$, emulsion turns into a suspension and Eq. 2.3 reduces to Eq. 2.1. Contrarily, if $\eta_{ld} << \eta_o$, emulsion turns into a foam-like body (Derkach, 2009), and Eq. 2.4 is obtained.

$$\eta_r = 1 + \phi_d \tag{2.4}$$

The rheology of concentrated emulsions and suspensions was studied by Yaron and Gal-Or (1972). The motion around rigid and deformable uniformly-sized particles was analyzed mathematically. For the work, consideration was given to a Couette, uniform, and hyperbolic shear field. When a uniform shear field is involved, they discovered that $\eta_r = 0$. However, in the presence of a Couette or a hyperbolic shear field, the equation below was obtained.

$$\eta_r = 1 + 5.5\gamma^3\psi \tag{2.5}$$

where $\psi = \frac{4\gamma^7 + 10 - \frac{84}{11}\gamma^2 + 4\beta_2(1-\gamma^7)}{10(1-\gamma^{10}) - 25\gamma^3(1-\gamma^4) + 10\beta_2(1-\gamma^3)(1-\gamma^7)}$ (2.6)

$$\beta_e = \frac{\eta_o}{\eta_d + \tilde{\gamma}_e} \tag{2.7}$$

where γ is ratio of radii of particle and cell; ψ is equation parameter; β_e is viscosity parameter; η_d is viscosity of the dispersed phase (which is η_{ld} in the case of an emulsion); $\tilde{\gamma}_e$ is interfacial retardation viscosity; e is an integer.

But, ϕ_d is given as:

$$\phi_d = \gamma^3 \tag{2.8}$$

Then, Eqs. 2.5 and 2.6 becomes:

$$\eta_r = 1 + 5.5\phi_d\psi \tag{2.9}$$

where $\psi = \frac{4\phi_d^{7/3} + 10 - \frac{84}{11}\phi_d^{2/3} + 4\beta_2(1-\phi_d^{7/3})}{10\left(1-\phi_d^{10/3}\right) - 25\phi_d\left(1-\phi_d^{4/3}\right) + 10\beta_2(1-\phi_d)(1-\phi_d^{7/3})}$ (2.10)

Likewise, Phan-Thien and Pham (1997) derived a solution for the viscosity of concentrated suspension of droplets. Both the droplet and continuous phases are Newtonian fluids, and also, is the resulting emulsion. The solution of their droplet model is expressed as:

$$\phi_d = 1 - \left(\frac{\eta_o}{\eta_s}\right)^{2/5}\left(\frac{2\eta_o + 5\eta_{ld}}{2\eta_s + 5\eta_{ld}}\right)^{3/5} \tag{2.11}$$

Rearranging Eq. 2.11 and substituting η_s/η_o with η_r, this becomes:

$$(\eta_r)^{2/5}\left(\frac{2\eta_s+5\eta_{ld}}{2\eta_o+5\eta_{ld}}\right)^{3/5} = (1-\phi_d)^{-1} \quad (2.12)$$

If η_{ld} approaches ∞, the droplets become rigid. Then, Eq. 2.12 gives:

$$\eta_r = (1-\phi_d)^{-5/2} \quad (2.13)$$

In the limit of small ϕ_d, Eq. 2.13 reduces to Einstein (1906) equation presented in Eq. 2.2. If η_{ld} approaches 0, the droplets become bubble-like, and Eq. 2.12 becomes:

$$\eta_r = (1-\phi_d)^{-1} \quad (2.14)$$

Similarly, in the limit of small ϕ_d, Eq. 2.14 reduces to Eq. 2.4.

2.2.1.2. Non-Newtonian Models

The invert emulsions utilized during drilling do possess some yield stress, and efforts have been made to derive non-Newtonian models for them. Due to the simplicity of the Bingham Plastic ($\tau = \tau_y + \mu_p\dot{\gamma}$) and Power-Law ($\tau = K\dot{\gamma}^n$) models, the petroleum industry is accustomed to using them in predicting the effective viscosity of drilling fluids in pipe and annulus (Muherei, 2016). In these models, τ is shear stress; K is consistency index; $\dot{\gamma}$ is shear rate; n is fluid behavior index; τ_y is yield stress; μ_p is plastic viscosity. However, majority of these drilling fluids are best fitted with the Herschel-Bulkley model ($\tau = \tau_y + K\dot{\gamma}^n$), especially at low shear rates (Hemphill et al., 1993; Kenny and Hemphill, 1996; Hemphill and Larsen, 1996; Herzhaft et al., 2003; Khalil and Mohamed Jan, 2012). Furthermore, Vajargah et al. (2016) said that the Herschel-Bulkley model better fits the rheological data of majority of drilling, completion, and cementing fluids. The importance of achieving accurate rheological parameters from the models cannot be undermined. Wellbore hydraulics is important for the optimization of drilling, and the accuracy of its execution greatly relies on the correctness of rheological parameters (Vajargah et al., 2016).

The rheology of the OBM studied by Houwen and Geehan (1986) best fits the Herschel-Bulkley and Casson ($\tau^{\frac{1}{2}} = k_o + k_1\dot{\gamma}^{\frac{1}{2}}$) models, where k_o and k_1 are fluid rheological parameters. The Casson yield stress, $\tau_y = (k_o)^2$, and the Casson plastic viscosity, $\mu_p = (k_1)^2$. However, to simplify hydraulic models, the Bingham Plastic model, which is not accurate at low shear rates, is often used in modeling OBMs. Davison et al. (1999) investigated the rheology of OBM, SBM, and WBM under simulated deepwater drilling conditions. Both the Casson and Herschel-Bulkley models fairly matched the rheological data of OBM and SBM whereas the Herschel-Bulkley model gave a better description of the flow behavior of WBMs including salt/polymer fluids and unweighted bentonite-based mud. Another study (Dingsøyr et al., 2004) also reported the appropriateness of Herschel-Bulkley model for describing the rheological behavior of OBMs.

2.2.2. Effects of Temperature and Pressure

The rheological properties of OBM usually experience a significant change with temperature. De Wolfe et al. (1983) investigated the influence of temperature and pressure on the rheological properties of OBM. Below 93°C, the results revealed that temperature has strong effect on viscosity. Also, temperature shows dominance over pressure in influencing OBM viscosity. Furthermore, Herzhaft et al. (2001) and Politte (1985) examined the effects of temperature and pressure on the viscous properties of OBMs. The results of Herzhaft et al. (2001) revealed that the apparent viscosities of the OBMs and base oils decreased with temperature. Besides, an increase in pressure led to higher apparent viscosity values.

Amani (2012) studied the rheology of OBM under HPHT situations (maximum temperature and pressure: 288°C and 241 MPa). The results revealed that viscosity, yield point, and gel strength reduced as temperature increased. Considering the effect of pressure, increases

in viscosity and yield point were noticeable as pressure was increased. The variation of viscosity with temperature or pressure followed exponential functions given below.

$$\mu = ae^{b/T} \tag{2.15}$$

$$\mu = ae^{bP} \tag{2.16}$$

where μ is viscosity; a and b are empirical constants; T is temperature; P is pressure.

Hermoso et al. (2014) investigated the viscosity of drilling muds in the presence of temperature and pressure. Viscosity and yield stress reduced as temperature increased, but, the yield stress of one of the fluid samples increased when a particular temperature value was exceeded (this was ascribed to the structural changes caused by thermally induced gelling). Yield stress showed a linear increase with pressure due to compression of the organoclay microstructures developed in the fluid. Using a factorial WLF-Barus model, the following expression was obtained.

$$\mu_p(P,T) = \mu_{pa} 10^{\left(-\frac{c_1(T-T_o)}{c_2+(T-T_o)}\right)} e^{[\beta(T)(P-P_o)]} \tag{2.17}$$

where $\beta(T) = \beta_o + \beta_1(T - T_o)$. μ_{pa} is plastic viscosity at atmospheric pressure condition; T_o is reference temperature (40°C); P_o is atmospheric pressure; c_1 and c_2 are empirical constants; β(T) is piezo-viscous coefficient; β_o and β_1 are empirical parameters.

2.3. Mechanisms of Barite Sag

Depending on the position of a settling column, the mechanisms that govern sedimentation varies. The movement of displaced fluid and particle interaction (hindered settling) are other important considerations in settling.

2.3.1. Settling in Vertical Ducts

The three settling zones (or regimes) in a vertical tube are displayed in Fig. 2.1a. The remaining few particles in the clarification zone settle with minimal interference from adjacent particles and tube walls. Stokes' law is applicable in this regime. The downward movement of a single particle in a Newtonian fluid under laminar flow (creeping flow) condition is explained by Stokes' law as expressed below.

$$v_\infty = \frac{(d_s)^2(\rho_s - \rho_f)g}{18\mu_f} \tag{2.18}$$

where v_∞ is settling velocity of a particle without hydrodynamic interference; d_s is particle diameter; ρ_s is particle density; ρ_f is fluid density; g is acceleration due to gravity; μ_f is fluid viscosity.

In the hindered settling zone, particle-particle interference occurs due to the huge number of particles. Unlike in the clarification regime, the settling velocity of particles reduces in this zone. If the particles aggregate, the settling velocity can increase due to size increment. The compaction zone has the highest number of particles per volume. As the solids bed gets compacted, excess fluid is discharged very slowly in the upward direction.

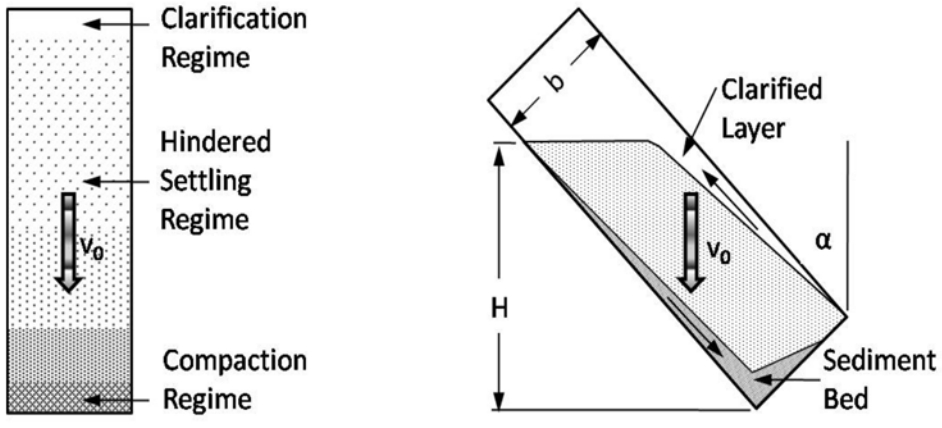

(a) **(b)**

Fig. 2.1: Settling under static condition: a) vertical pipe; and b) inclined pipe (Zamora, 2009)

2.3.2. Settling in Inclined Duct

According to Boycott (1920), blood corpuscles fall quickly when a narrow tube is in an inclined position compared to when its position is vertical. The settling mechanism differs in an inclined tube as illustrated in Fig. 2.1b. Though, particles still settle in the vertical direction; however, their travelling path to the low-side of the tube is shorter. The clarified layer (zone) develops rapidly, and moves in the upward direction owing to buoyancy (Zamora, 2009). As particles settle, the displaced fluid gathers and travels upward quickly owing to the inclined passage generated by the clarified zone. Ultimately, a bed is formed, and thereafter, it slides downward.

For Boycott settling description, Hanson et al. (1990) stated that a slim clarified fluid zone forms quickly beneath the upper wall. Also, another clarified zone develops above the fluid. Particle settling occurs in the suspension zone, and a bed is formed. Then, this bed slides in the downward direction. The sliding creates a cross-sectional density variation that generates a pressure difference. Hence, convection currents are created in the suspension zone. These currents move the lighter fluid up and the bed downward, therefore speeding up sedimentation in this zone.

2.4. Fundamental Concepts of Barite Sag in Non-Newtonian Fluid

According to Saasen (2002), fluid density creates two factors that affect barite settling in a drilling fluid. When a particle falls, a counter-flow of displaced fluid occupies the volume that the particle once filled. If the weight-material concentration is low, then, the counter-flow velocity will be minimal. However, if the weight-material concentration is high, then, more particles are available for settling. Therefore, large volumes of fluid will be displaced. Consequently, the counter-flow will pose more opposition to settling velocity. This shows that barite sag decreases as mud density or particle concentration increases.

The yield stress is a vital rheological parameter for static sag occurrence. According to Dedegil (1987), the vertical component of the yield stress force acting on a spherical particle is:

$$T_{\tau ys} = \left(\frac{\pi}{2} d_s\right)^2 \tau_y \tag{2.19}$$

Knowing that $\rho_s = \frac{m_s}{V_s} = \frac{F_g}{V_s g}$ (2.20)

Thus, $F_g = \rho_s V_s g$ (2.21)

Also, $F_b = \rho_f V_s g$ (2.22)

Under equilibrium condition, $F = F_g - F_b$ (2.23)

Therefore, $F = (\rho_s - \rho_f) V_s g = \Delta\rho V_s g$ (2.24)

Volume of a sphere, $V_s = \frac{4\pi r_s^3}{3} = \frac{\pi d_s^3}{6}$ (2.25)

Substituting Eq. 2.25 into Eq. 2.24 gives:

$$F = \Delta\rho \frac{\pi d_s^3}{6} g \tag{2.26}$$

From Eq. 2.19, $\tau_y = \frac{4}{\pi^2} \frac{T_{\tau ys}}{d_s^2}$ (2.27)

Under static condition, $T_{\tau ys} = F$. Therefore, the yield stress needed to prevent sag in a static mode is:

$$\tau_y \geq \frac{2}{3\pi} \Delta\rho d_s g \tag{2.28}$$

where $T_{\tau ys}$ is the vertical component of the yield stress force acting on a spherical particle; F_g is gravity force; F_b is buoyancy force; F is the net force acting on the particle; $\Delta\rho$ is density difference between particle and base fluid; V_s is particle volume; r_s is particle radius; m_s is particle mass.

2.5. Sag Measurement Techniques

Over the years, different methods have been created for the quantification of sag in the invert-emulsions used during drilling operations.

2.5.1. Test Cell Method

In static sag testing, mud sample is poured into a tube or steel cell. Then, the cell is allowed to stay unperturbed for a specified amount of time. Barite sag is more of a problem under dynamic conditions. However, no dynamic condition is considered in a static method. Omland et al. (2006) aged mud samples in steel containers at 50°C for 16 hours. For analysis of mud weight measurements at the end of testing period, a sag factor was calculated with Eq. 2.29. A sag factor of 0.5 signifies that no settling happened, while a value greater than 0.5 indicates sag occurrence. This sag factor does not consider the quantity of the top free liquid, hence, sag can be under-predicted.

$$Sag\ Factor = \frac{MW_{bottom}}{MW_{bottom}+MW_{top}} \tag{2.29}$$

A consideration for the separated free water was made by Omland et al. (2004) by the introduction of a dynamic sedimentation index as expressed below.

$$S_D(t) = \frac{MW_{bottom}}{2MW_{initial}} \tag{2.30}$$

where MW is mud weight; $S_D(t)$ is dynamic sedimentation index; $S_D(0) = 0.5$.

Parvizinia et al. (2011) investigated barite settling in OBMs when static and dynamic conditions are present. The authors used a cylindrical sag-testing cell that had a rotating disk. To provide temperature, a copper-coil heating tube was installed for the circulation of hot water. Pressure profiles were measured with respect to time with pressure sensors positioned on the wall of the sag-testing cell. Results showed pressure reduction with time due to the sagging. The upper part of the OBMs experienced the highest pressure reduction. With increasing disc

rotation, more pressure reduction was recorded at the top of the mud column. Besides, pressure decreased as temperature increased. In comparison to disk rotation speed, the effect of temperature on density change was more noticeable.

2.5.2. Viscometer Sag Test (VST)

Jefferson (1991) introduced the VST measurement technique as a method of estimating the outcome of dynamic situations on settling at the time the petroleum industry was starting to acknowledge weight-material settling as a dynamic event. A regular rotational viscometer and thermocup is utilized for the VST. The thermocup is filled with mud sample, and both are heated to 49 or 66°C while shearing the mud at 100 rpm for 30 minutes. The shearing represents a dynamic condition. A syringe is used to retrieve mud samples (10 or 20 mL depending on the technique of density determination) from the bottom of thermocup before and after testing, and then weighed on a sensitive balance. The recorded increase in mud density is due to sagging. Apart from syringe, a pycnometer or a retort cup can also be used.

2.5.3. Viscometer Sag Shoe Test (VSST)

The suitability of sag measurement equipment for oilfield application is very important. Also, the achievement of correct results in a limited amount of time is required considering the swift nature of oilfield tasks. The VST is a direct sag-indicator test, but in spite of its simplicity and low cost, it lacks a wide acceptance by the petroleum industry (Zamora and Bell, 2004). In an attempt to improve the VST, Zamora and Bell (2004) presented the VSST. The improvement made by the authors was the introduction of a Sag Shoe (or thermoplastic Shoe). According to Zamora (2011), this modification improved the reliability of the regular VST method.

The geometries of VST and VSST methods are compared in Fig. 2.2. The inclined surface of the Sag Shoe expedites barite settling, and also, facilitates the gathering of settled

weight-materials into the collection well (Fig. 2.3). This well permits the removal and replacement of bed samples, and also, permits the investigation of the test mud's ability to pick-up a particle bed. The inclined surface of the Sag Shoe has two sections (Fig. 2.3). The "lip" that results from the misalignment of the two sections disallows the picking-up of settled barite during a sag test (Zamora and Bell, 2004). Contrarily, the height of the lip allows the picking-up of a barite bed during a bed pick-up experiment.

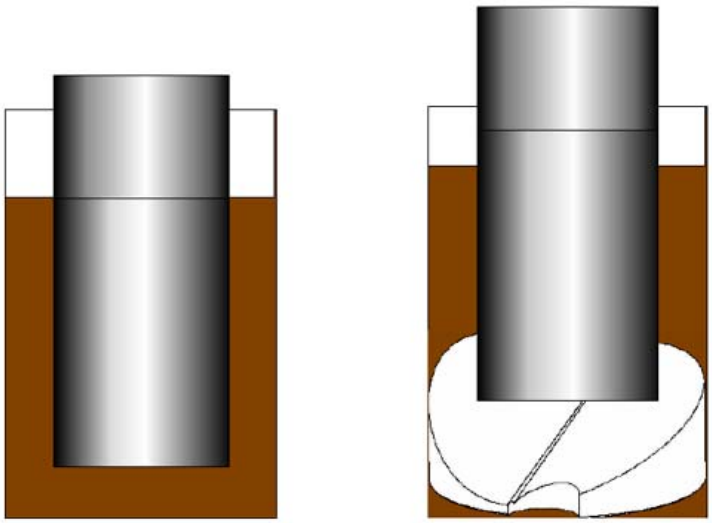

(a) **(b)**

Fig. 2.2: Schematic of the geometry of: a) VST method; and b) VSST method (adapted from Zamora and Bell, 2004)

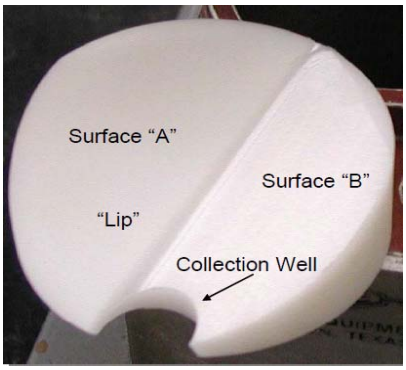

Fig. 2.3: Sag Shoe (Zamora and Bell, 2004)

Due to the expansion of a thermoplastic material, a temperature of 49°C was deemed the most suitable for Sag Shoe application. At higher temperatures, the Sag Shoe was hard to remove from the thermocup. The dissimilarities in VSST and flow loop geometries disfavor the comparison of results from these two sag measurement techniques. Therefore, Zamora and Jefferson (1994) developed a modified sag register in order to ensure a reliable comparison. The expression is:

$$S_R = exp\left(-k\frac{\Delta MW_b}{MW_{initial}}\right) \quad (2.31)$$

where S_R is sag register; k is correlation constant; ΔMW_b is difference of the maximum and minimum mud weight obtained during bottoms-up circulation. The negative sign ensures that $0 < S_R \leq 1$. There is no sag when S_R is 1, but lower values signify sag occurrence. According to Zamora and Bell (2004), k is around 10 for VSST and 50 for flow loop.

With field and numerous flow loop data, Zamora (2009) used the method of Jefferson (1991) to obtain the sag index constants (Table 2.1) for the VSST method. The constants can be changed and new ones can be included to allow usage at different locations (Zamora, 2009). The sag index is obtained by multiplying mud weight difference by the product of four severity factors (Jefferson, 1991). Zamora (2009) expressed the sag index, S as:

$$S = \Delta MW \times Ka \times Kv \times Kr \times Kz \quad (2.32)$$

where ΔMW is mud weight difference derived from a VSST, lbm/gal; Ka is the constant representing inclination angle; Kv is the constant representing annular velocity; Kr is the constant representing rotary speed; Kz is the constant representing well section length. A comparison should be made between the sag index and the difference between the maximum and the nominal mud weight obtained during bottoms-up circulation.

Table 2.1: Sag index constants for VSST method (Zamora, 2009)

Angle (°)	Ka
<5	0
5-10	0.03
10-30	0.3
30-40	0.7
40-70	1.0
70-80	0.8
80-90	0.6

Ann Vel (ft/min)	Kv
<2	1.0
2-50	1.2
50-100	0.9
100-150	0.6
150-250	0.3
>250	0.1

Rotary (rpm)	Kr
<5	1.0
5-75	1.1
75-100	0.8
100-150	0.5
>150	0.3

Length (ft)	Kz
<1000	0.5
1000-2000	0.7
2000-5000	1.0
>5000	1.2

2.5.4. Flow Loop Test

The application of flow loop for sag quantification helps in the gathering of reliable data (Omland, 2009). Nevertheless, the replication of exact downhole situations (such as hole geometry, drill string rotation, and temperature effects) is often challenging (Omland et al., 2007). The requirement of advanced equipment, substantial mud volume, and large space are the drawbacks of this method. Hanson et al. (1990) used inclined flow loop in their laboratory studies of field muds, and reported the formation of barite bed during circulation. The bed solidified when flow was halted, and later slumped to create density differences. The slumping of bed occurred at 30 – 60° at low flow rates, but was more at 40 – 50° and stopped at higher inclination angles. Saasen et al. (1995) created a flow loop that resembled the one designed by Hanson et al. (1990), and developed a method of obtaining settling information from rheological data. Dynamic condition was created by the movement of small logging tools, and this promoted bed slumping.

Dye et al. (2001) conducted flow loop tests at a temperature of 49°C, shear rates of 0.1 – 10.4 s^{-1}, inclination angles of 45 – 60°, and drill pipe eccentricity of 0.7. In another flow loop investigation, Dye et al. (2003) examined the connection between shearing and dynamic settling

in invert emulsions at various inclination angles (25 – 70°), flow rates (0 – 40 gpm), and eccentricity (0 – 100%). Bern et al. (1998) investigated barite settling in 20 different fluids with the use of a special flow loop. They considered annular velocity, inclination angle, eccentricity, and pipe rotation.

A flow loop was used by Hashemian (2012a) to examine the effect of key drilling parameters on barite settling. The length of the annular section and the volume of the mud tank was 35 ft and 50 gal, respectively. Also, mud circulation was achieved with a centrifugal pump (Fig. 2.4). The design allowed the variation of eccentricity, annular velocity, pipe rotation, and inclination angle. Coriolis densitometers, placed at the entry and exit of test section, was used to record density. Nguyen et al. (2014) conducted dynamic sag experiments in a flow loop, and examined various combinations of inclination angle, pipe rotation, eccentricity, and annular velocity. They found annular velocity to be the highest contributor to barite sag prevention.

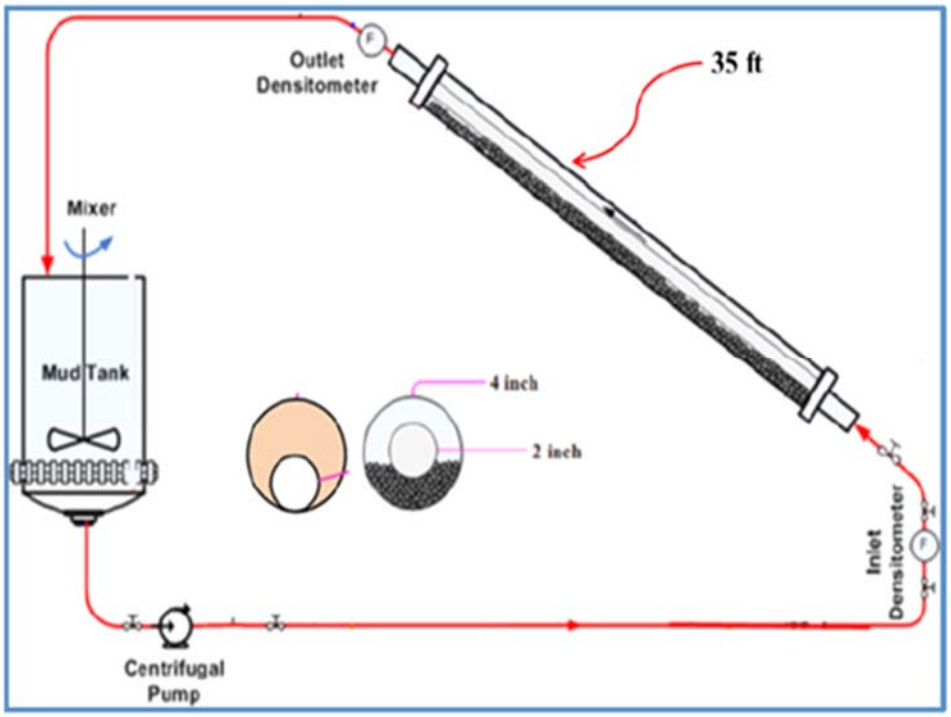

Fig. 2.4: Flow loop design (Hashemian, 2012a)

2.5.5. Dynamic High-Angle Sag Tester (DHAST)

Jamison and Clements (1990) introduced a laboratory measurement technique that aided the automation of static settling evaluations. Now that the industry recognizes barite sag as a dynamic issue, Murphy et al. (2006, 2008) added an inner rotating-pipe to the setup of Jamison and Clements (1990). The device was named a Dynamic High-Angle Sag Tester (DHAST). Murphy et al. (2008) reported that the DHAST (Fig. 2.5) operates at a maximum temperature and pressure of 177°C and 69 MPa, respectively. Also, only a small volume of test sample is required. It is furnished with a pressurization chamber, and inclination angle variations. An external magnetic field is used to balance the sample cell in the chamber, and a shear bob rotates inside the sample cell. Testing time is 3 hours, and sag rate measurements are performed every 30 minutes.

Fig. 2.5: A Dynamic High-Angle Sag Tester (DHAST) (Halliburton, 2006)

2.6. Factors Affecting the Settling Behavior of Barite Particles

The settling behavior of barite particles in drilling muds is affected by various factors such as mud properties (rheology, particle concentration, and particle size and distribution), drilling operational parameters, flow regime, and hole diameter (Tehrani et al., 2009; Bern et al., 1996; Nguyen et al., 2011; Hashemian et al., 2014). The effects of most of the fluid properties are incorporated in the Stokes' law. However, this law cannot fully describe the phenomenon of barite sag due to its complexity resulting from involvement of different physical processes that include shear enhanced sedimentation, lateral settling, sediment bed formation and sliding, formation of secondary flows due to density differences, and hindered settling (Tehrani et al., 2009). Many studies have focused on connecting barite sag to mud rheology.

2.6.1. Effects of Rheology, Mud Components, and Shearing on Barite Settling

The types of materials in a mud, and the shear that the mud experiences will affect its rheological properties. Since barite particles settle in a mud, it is obvious that the rheological properties of that mud will influence the settling rate. Also, the properties of the weight-material will control its sagging rate.

2.6.1.1. Rheological Parameters

Tehrani et al. (2004) investigated the link between rheological characteristics and dynamic settling in drilling muds using two modified conventional VST methods. They observed a decrease in density change as low-shear-rate viscosity, elastic modulus (G′), and complex viscosity (V*) increased (Fig. 2.6 through 2.8). Also, Saasen et al. (1995) investigated barite sag in an inclined sag cell that was furnished with a reciprocating rod (for mimicking axial motion). Their outcomes illustrated that static settling decreased as 10-minute gel increased. Besides, dynamic sag decreased as 3 rpm reading increased.

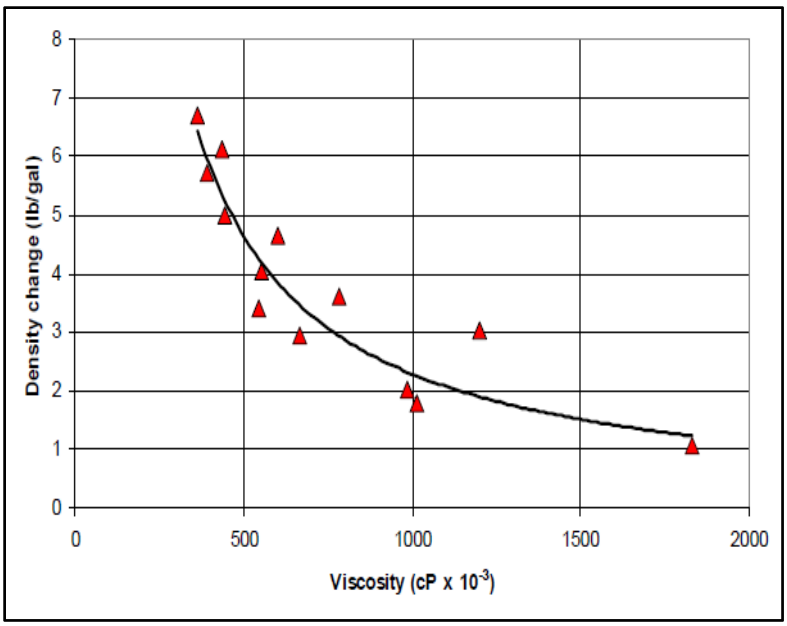

Fig. 2.6: Dynamic sag in organoclay-based muds versus low-shear-rate viscosity at 10^{-3} s^{-1} - data from VST2 at 20°C (Tehrani et al., 2004)

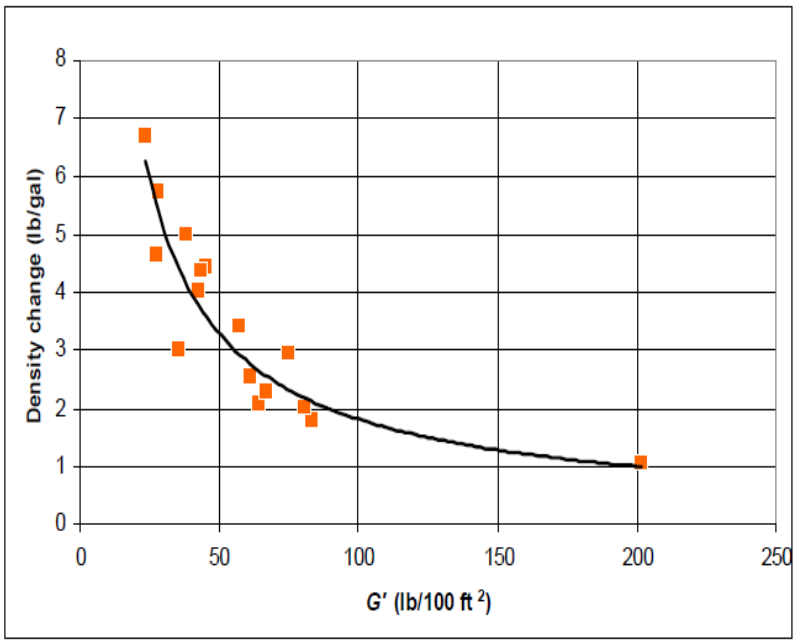

Fig. 2.7: Dynamic sag in organoclay-based muds versus G′ at 1 Hz - data from VST2 at 20°C (Tehrani et al., 2004)

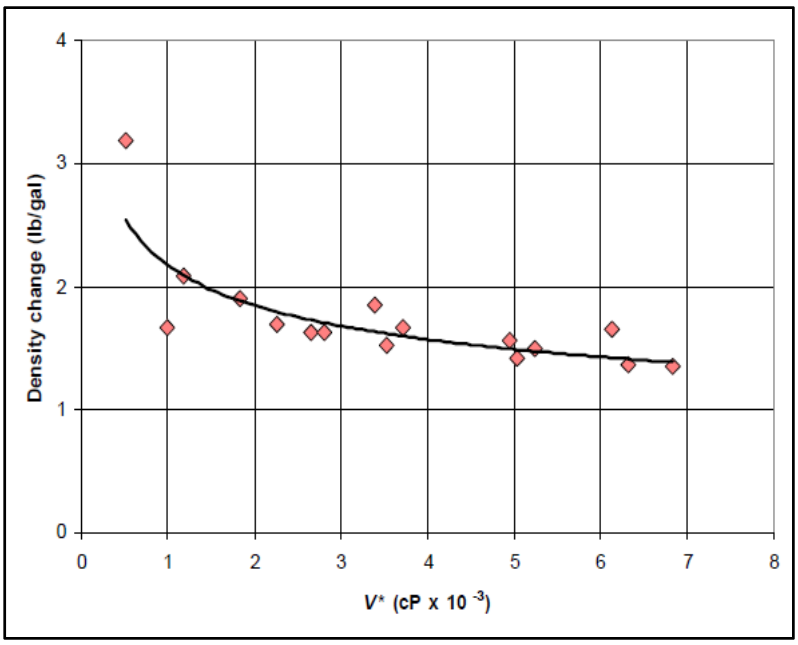

Fig. 2.8: Dynamic sag in organoclay-based muds versus complex viscosity at 1 Hz - data from VST1 at 50°C (Tehrani et al., 2004)

Nguyen et al. (2011) investigated dynamic barite settling in OBM samples using a modified rotational viscometer. The change in mud weight was calculated as the difference between the weights of mud samples taken at the bottom and at the surface of the thermocup. From their results, OBDF2 (mud with the higher yield stress) resisted sagging at static condition (Fig. 2.9). Tehrani et al. (2009) investigated dynamic sag in drilling muds at 49°C using the VSST method. Their results showed the ability of yield stress in reducing sag at low speeds. As shear rate increased, this ability declined and the reduction of barite sag is facilitated by viscosity. Thus, they linked dynamic settling to the product of viscosity and yield stress as presented in Fig. 2.10. The work of Savari et al. (2013), conducted with DHAST at 130°C and 14 MPa, showed a correlation between sagging and dynamic yield stress. Their results revealed that the OBM sample with the lowest sag tendency had the highest dynamic yield stress.

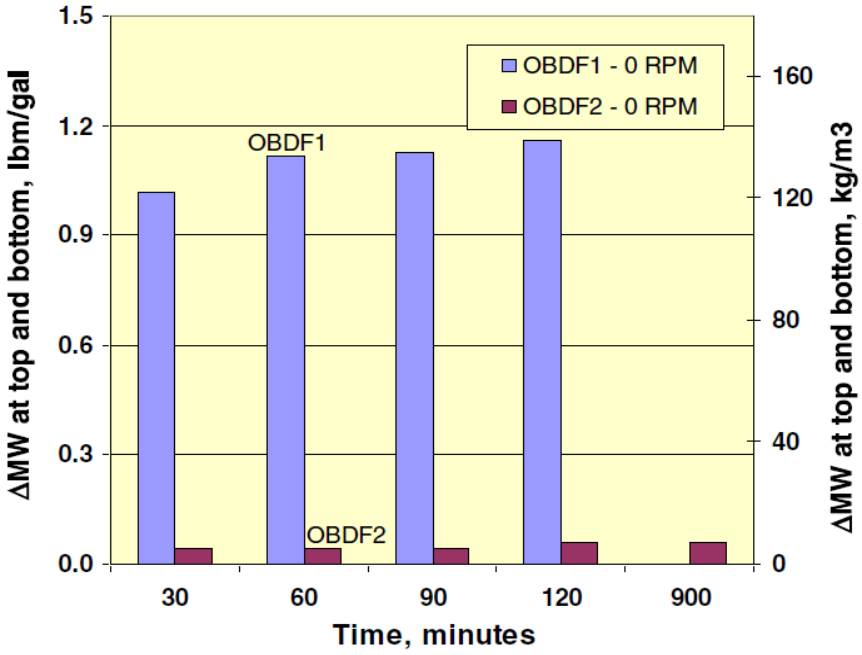

Fig. 2.9: Change in mud density under static condition – effect of yield stress (Nguyen et al., 2011)

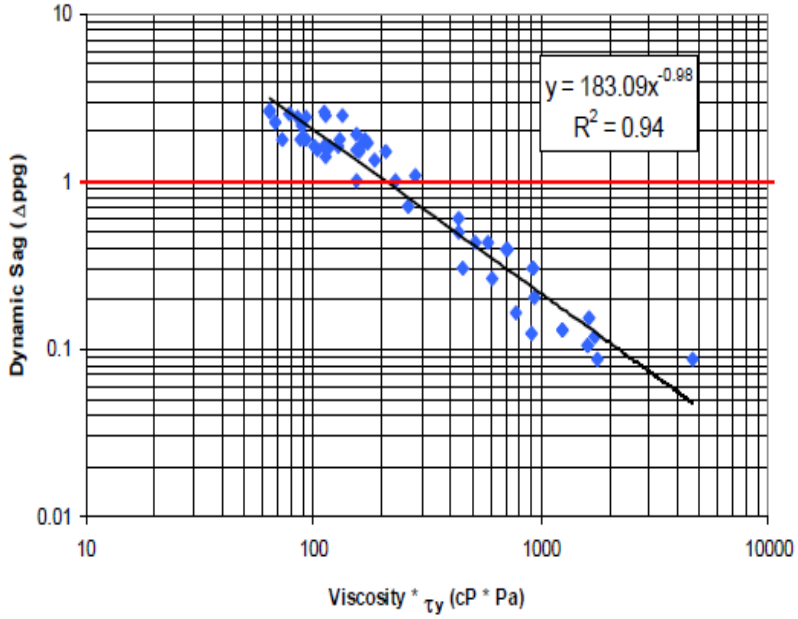

Fig. 2.10: Correlation of dynamic sag to the product of viscosity and yield stress (Tehrani et al., 2009)

2.6.1.2. Particle Density, Size Distribution, and Concentration

Each weight-material type has its own density and size distribution. Thus, the type used in a mud design has an influence on settling rate. Lately, fine and ultra-fine weight-materials have been used (Taugbøl et al., 2005; Gregoire et al., 2009; Al-Bagoury and Steele, 2012; Fimreite et al., 2004; Elkatatny et al., 2012; Massam et al., 2004; Xiao et al., 2013; Al-Bagoury, 2014). These materials are usually referred to as Micronized Weight Material (MWM). The settling velocity is influenced by particle concentration. In the presence of a static mode, a higher settling velocity will be obtained if the particle concentration is low compared to when its high. At high particle concentrations, hindered settling sets in owing to particle interactions. This leads to a reduction in settling velocity (Fig. 2.11).

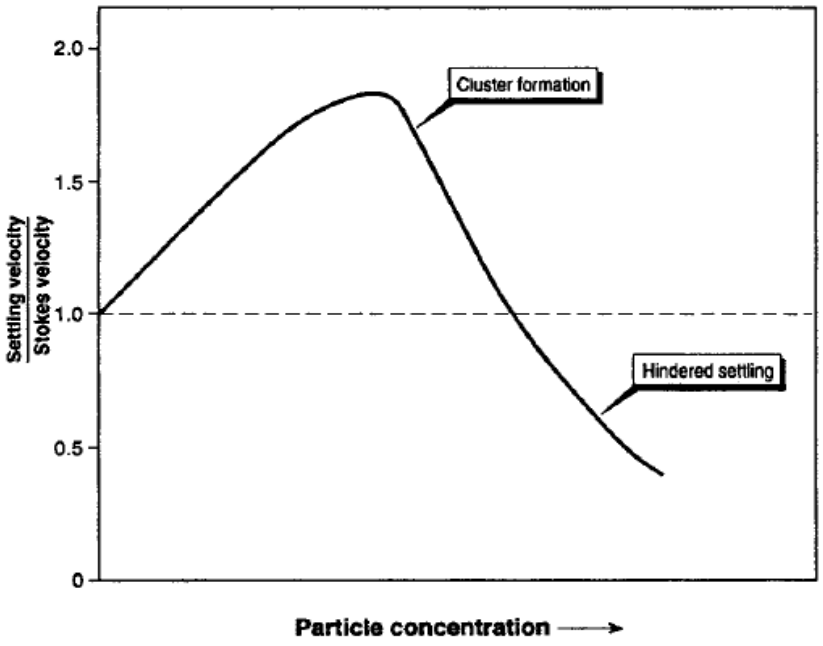

Fig. 2.11: Variation of static settling with particle concentration (Bern et al., 1996)

2.6.1.3. Internal or Brine Phase Treatment and Type, and Base Fluid Viscosity

Tehrani and Popplestone (2007) measured dynamic sag with the VSST, and their results showed that the addition of brine viscosifiers to the internal (or brine) phase can enhance low-end rheology and sag resistance. In explaining the results, they stated that the treated internal phase displayed its influence through two processes. First, the well-dispersed internal phase behaved like inert solid particles and this led to rheological enhancement. The second mechanism involved the alteration of the brine droplets' surface chemistry. The alteration eased the interaction of the brine phase with the additives (such as clay particles) that were distributed in the oil phase.

Omland et al. (2006) used calcium chloride ($CaCl_2$), sodium formate (HCOONa), potassium formate (HCOOK), and ammonium calcium nitrate [$NH_4Ca(NO_3)$] for the internal phases of SBMs and OBMs. The base fluids used were linear paraffin, mineral oil, ester, and linear-alpha-olefin (LAO). For static experiments conducted at 50°C, mud samples were stored for 16 hours in steel containers. Regardless of the base fluid type, the application of $NH_4Ca(NO_3)$ in brine phase prompted the smallest sag factors (Fig. 2.12). Hence, they inferred that $NH_4Ca(NO_3)$ promoted emulsion stability and emulsifier efficiency. Additionally, they observed that the mud samples made with thinner base fluids manifested the smallest viscosities and highest sag factors.

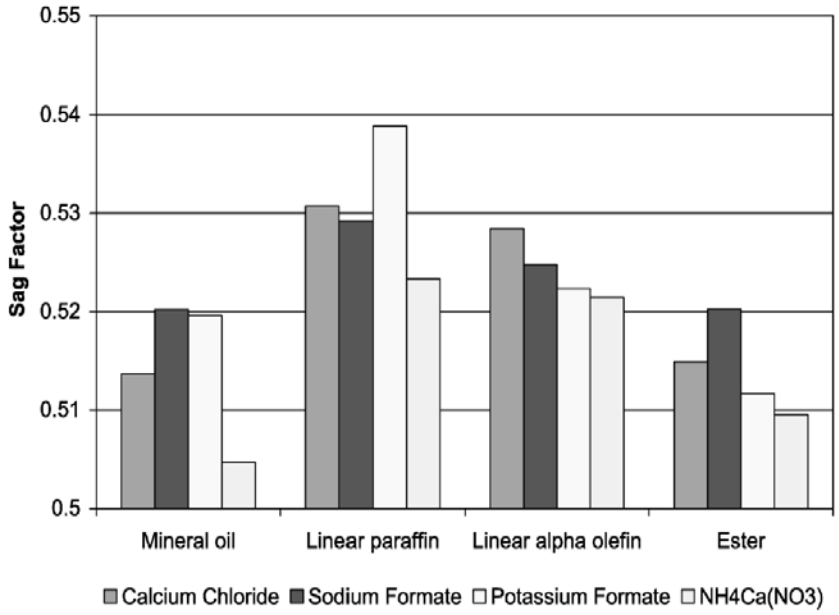

Fig. 2.12: Effect of brine phase type on sag factor (Omland et al., 2006)

2.6.1.4. Shear and Shear History

The level of shear used in creating emulsion considerably influences droplet size and emulsion stability. Also, the stability of emulsion improves as droplet size reduces. The results of the experimental investigation of Omland et al. (2004) showed that fluid viscosity and electrical stability measurements increased with shearing energy.

Shearing also influences the sagging process. A study (Nguyen et al., 2011) conducted using a modified rotational viscometer reported an increase in dynamic barite sag as rotational speed increased from 0 to 100 rpm (Fig. 2.13). The increase in barite sag was attributed to shear thinning. However, another barite sag study (Tehrani et al., 2009) conducted using the VSST method indicated significant reductions in barite settling at 300 rpm (Fig. 2.14). Similar observation was reported by Hemphill (2009) who used the results from DHAST to emphasize some vital information peculiar to a mud manifesting barite sag. First, when tested under dynamic condition, sag rate rapidly increased and this revealed the susceptibility of the mud

sample to barite sag. For the tested mud sample, the highest sag rate of 8 mm/hr was observed at a shear rate of 0.35 s^{-1} (Fig. 2.15). The case was classified as severe because of this high value. Below 2 s^{-1}, most of the high sag rates occurred. Above 2 s^{-1}, sag rates reduced and these were attributed to enhanced particle mixing. In addition to shearing, the studies of Kulkarni et al. (2014) also indicated the impact of shear history on barite sag.

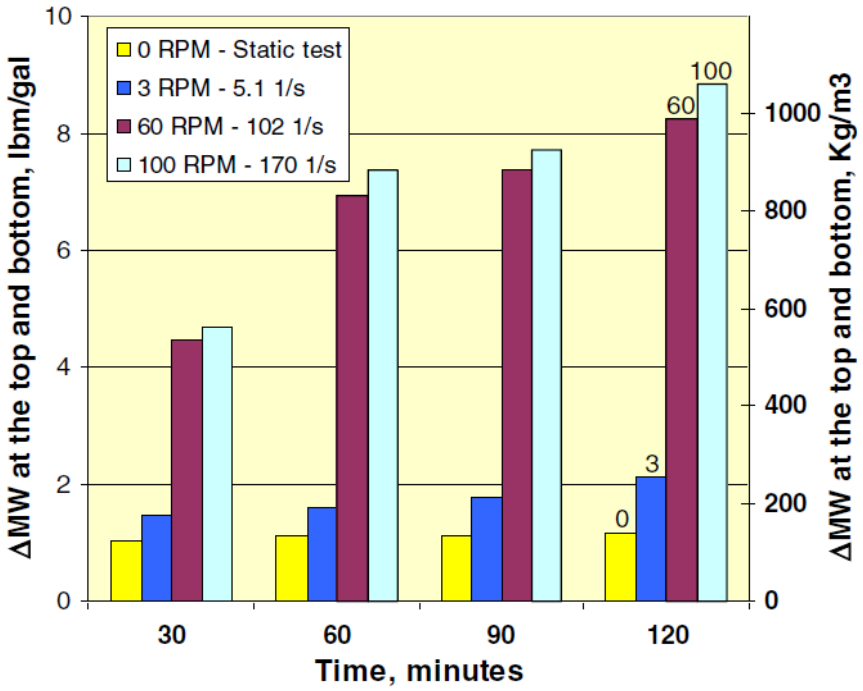

Fig. 2.13: Change in mud density of OBDF1 under dynamic condition – effect of rotational speed (Nguyen et al., 2011)

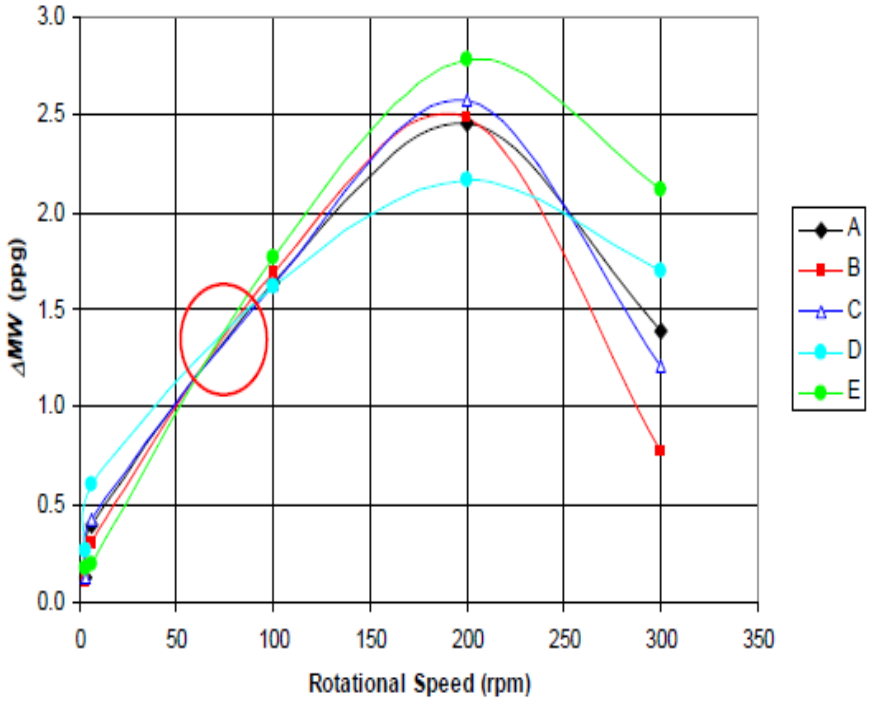

Fig. 2.14: Dynamic sag at different rotational speeds for different fluids at 49°C (Tehrani et al., 2009)

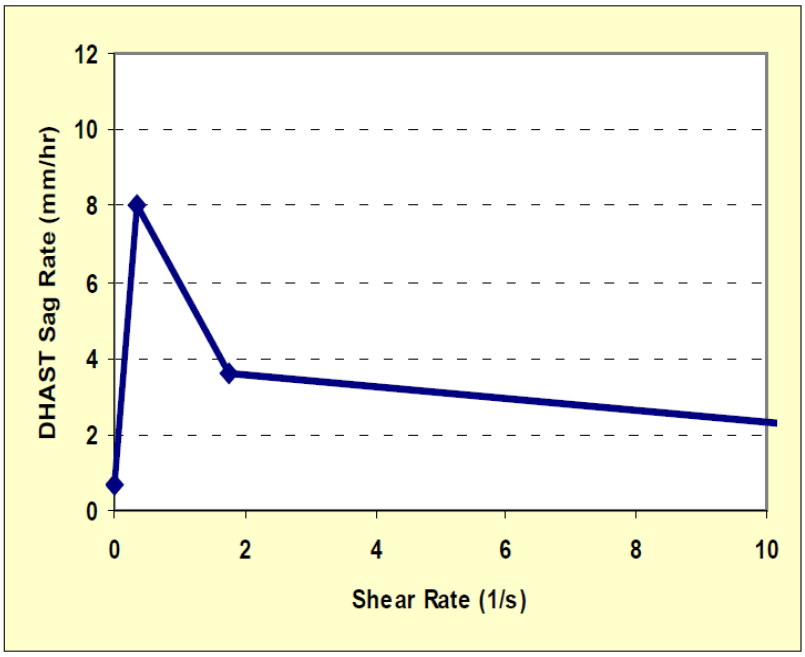

Fig. 2.15: Dynamic sag rate versus shear rate measured with the DHAST (Hemphill, 2009)

2.6.2. Effects of Drilling Operational Parameters

Besides fluid properties, operational parameters also substantially affect barite sag (Bern et al., 1996; Skalle et al., 1999; Dye et al., 2001). According to Bern et al. (1996), sag is more serious between 60 and 75° inclination angles (Fig. 2.16). An increase in pipe rotation promoted barite sag reduction. Additionally, sag tendency decreased as annular velocity increased and almost vanished at 100 ft/min. Furthermore, sag was exacerbated when the drill pipe was stationary and in fully eccentric position. Pipe rotation in an eccentric annulus led to the reduction of barite sag. The proximity of the pipe to the settled bed enhanced the rotational effect that eased the resuspension of settled particles.

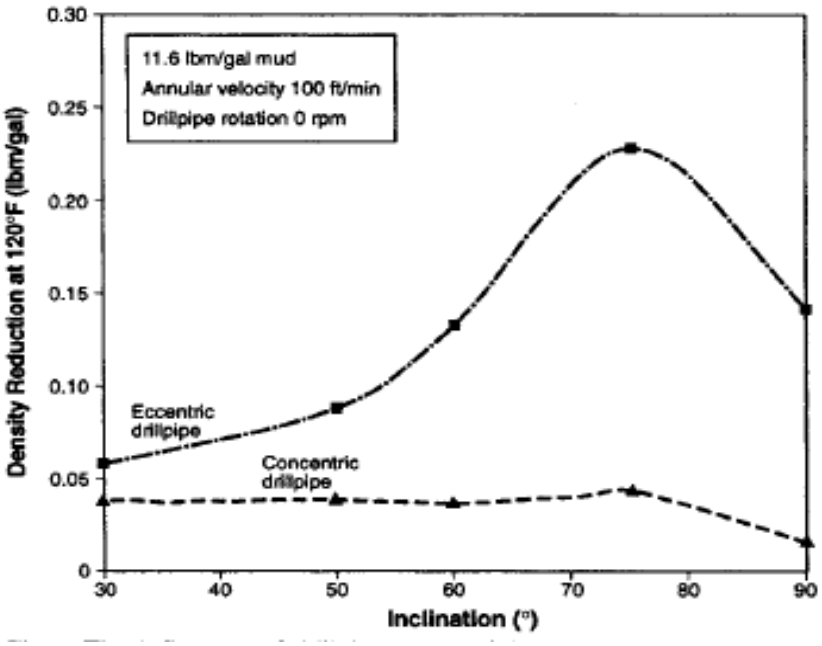

Fig. 2.16: Effect of drill pipe eccentricity on barite sag with no rotation (Bern et al., 1996)

A barite sag study (Skalle et al., 1999), performance under dynamic condition, reported that the circulation at laminar flow condition intensified barite sagging rate and bed sliding compared to static condition. Besides, muds that showed stability under static condition

exhibited sagging and bed sliding under flow condition. A similar study (Dye et al., 2001) reported more dynamic sag at 60° inclination than at 45°. Also, Dye et al. (2003) observed the (Fig. 2.17) disappearance of dynamic sag at high annular velocities (above 100 ft/min). A reduction in inclination angle assisted in lowering dynamic settling at low annular velocities. Recent barite sag studies (Hashemian, 2012a; Hashemian et al., 2014) also demonstrated a reduction in barite settling with declining inclination angle (Fig. 2.18). Furthermore, they reported an increase in sagging at low annular velocities. At both stationary and rotating pipe condition, a considerable sag reduction was realized in eccentric annulus compared to a concentric one (Fig. 2.19). However, the observations reported by Bern et al. (1996) and Nguyen et al. (2011) indicated the exacerbation of barite sag when annular velocity is low, and pipe is stationary (nonrotating) and eccentric (Figs. 2.16, 2.20 and 2.21).

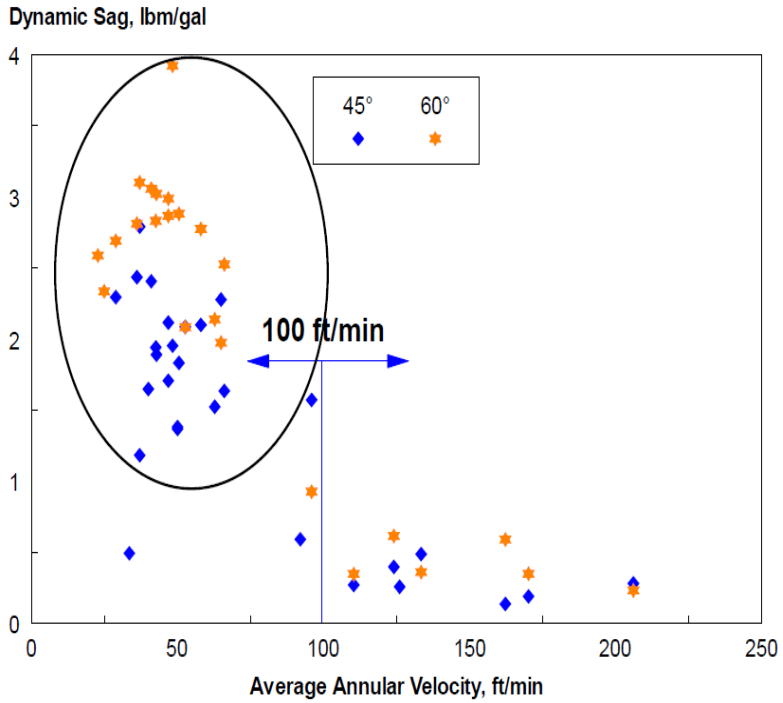

Fig. 2.17: Dynamic sag and annular velocity comparison from flow loop results (Dye et al., 2003)

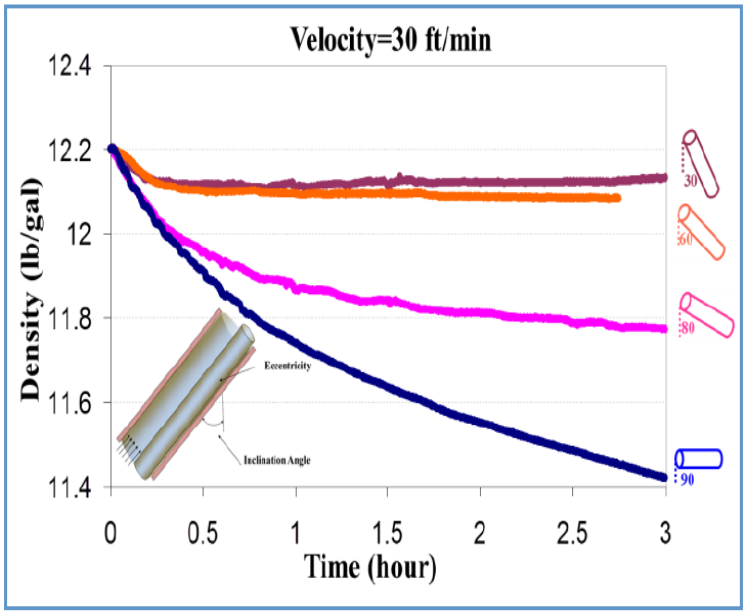

Fig. 2.18: Density profile in an eccentric annulus: a) effect of inclination; and b) effect of eccentricity (Hashemian, 2012a)

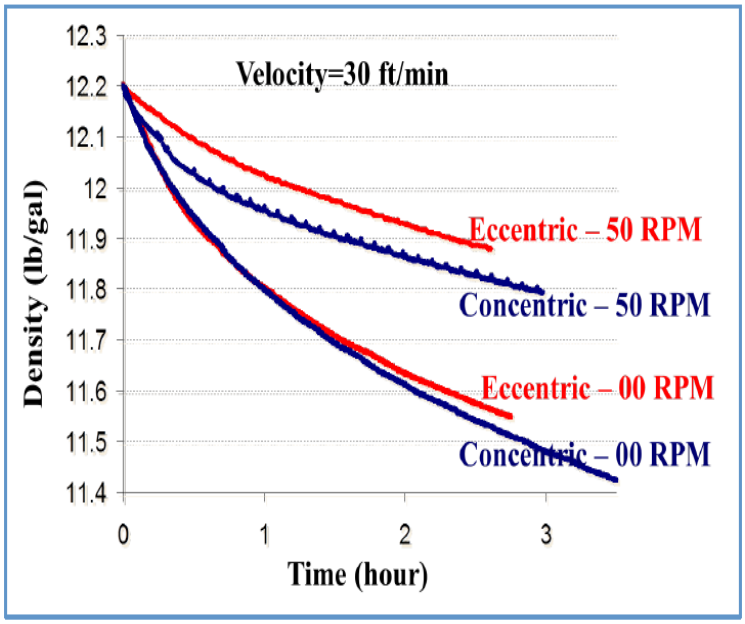

Fig. 2.19: Density profile in a horizontal configuration for eccentric and concentric annulus with/without rotation (Hashemian, 2012a)

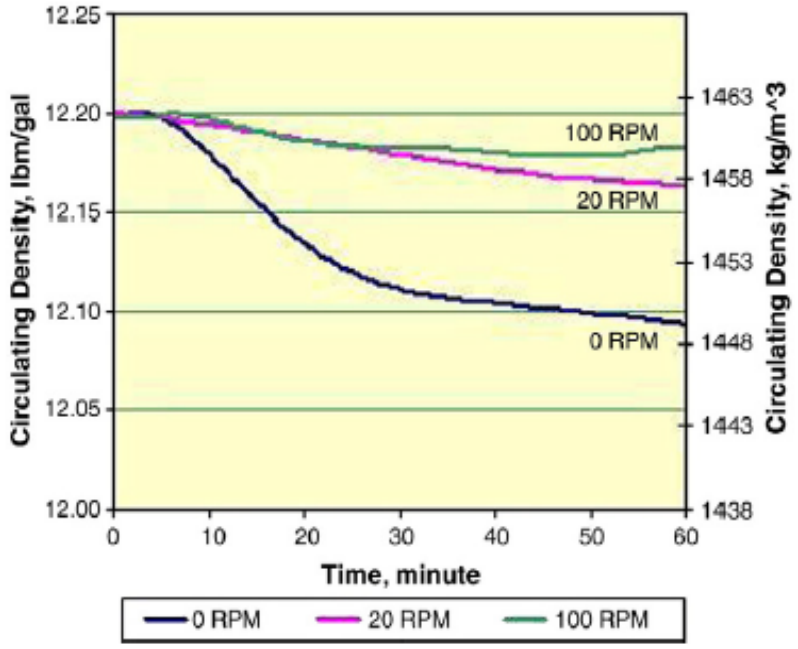

Fig. 2.20: Influence of pipe rotation on barite settling for a fully eccentric pipe at 60° inclination and annular velocity of 16.34 ft/min (Nguyen et al., 2011)

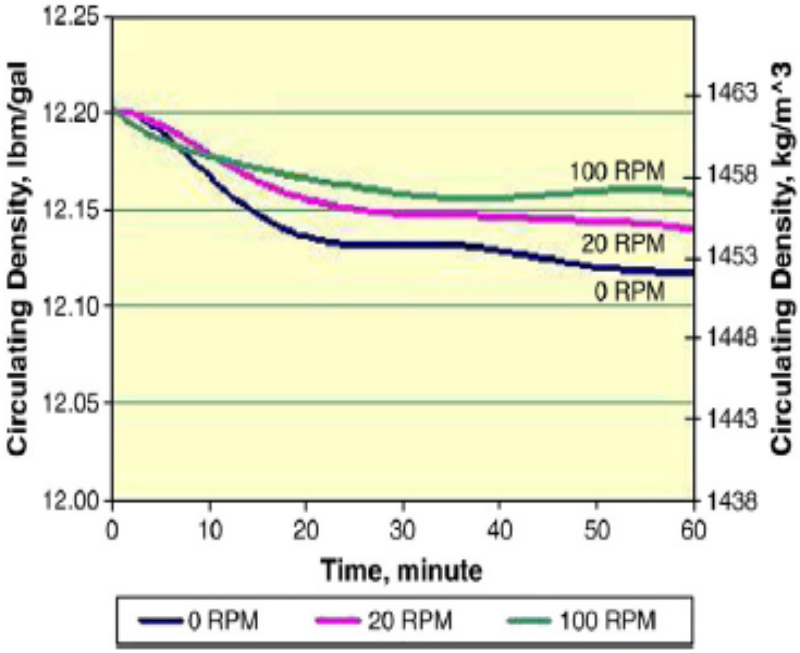

Fig. 2.21: Influence of pipe rotation on barite settling for a concentric pipe at 60° inclination and annular velocity of 16.34 ft/min (Nguyen et al., 2011)

2.7. Operational Procedures to Detect, Mitigate, and Remediate Barite Sag

During bottoms-up circulation, the continuous monitoring of annular density variations will help in the detection of barite sag (Zamora, 2009). The significance of constant vigilance of drilling process and suitable rig-site measurements cannot be underrated in executing effective monitoring plans (Bern et al., 1998). Rig-site monitoring can be attained through mud weight measurements, record of standpipe pressure, and torque and drag observation.

The execution of a technically drafted operational recommendation will facilitate the mitigation of barite sag. Mud rheological properties play a critical part in barite sag management (Zamora, 2009). Annular velocity is affected by wellbore geometry and flow rate. A high annular velocity will alleviate sag, and also, ease the resuspension of a weight-material bed. Clay-free invert emulsions can decrease sag occurrence (Van Zanten et al., 2012). Their stability was investigated from three areas, namely emulsifier concentration, effect of shear history, and presence of colloidal fines. The improvement in gel structure was ascribed to the properties of the internal phase. Clay-free invert emulsions should have a suitable emulsifier content, be prepared at high shear rates, and possibly contain a little quantity of colloidal fines (Van Zanten et al., 2012). According to Carbajal et al. (2009) and Burrows et al. (2004), clay-free invert emulsions have the ability to promote the control of ECD.

If a barite bed is suspected, proper procedures can be followed to prevent a barite sag event. For instance, bed resuspension can be initiated. According to Scott et al. (2004), a sagged mud can be reconditioned by performing a pilot test for the optimization of additives. Afterwards, mud treatment can be launched by applying the result of the pilot test.

2.8. Barite Sag Modeling

An emulsion can be treated as a continuum fluid (uniform viscosity and density) when the size of settling particles is much larger than the sizes of oil droplets (Beydoun et al., 1998). The authors used the continuum approximation to estimate settling velocity in their experimental work, but, they stated that this approximation may become invalid as droplet size increases and/or size of settling particles decreases. Using a laser granulometer, Herzhaft et al. (2003) measured the mean size of clay particles in an OBM test sample. The equipment showed that the size distribution concentrated around a mean value of 1.2 μm. Besides, a scanning electron microscope was used to perform a cryo-microscopic analysis and the results indicated that the mean size of the emulsion droplets was around 1 μm as illustrated in Fig. 2.22. Clearly, the emulsion droplets are much smaller than barite particles. Hence, the continuum approach can be used for modeling barite sag. The dispersion of clay particles in the continuous phase prevented their recognition, hence, Herzhaft et al. (2003) could not display them (Fig. 2.22).

Paslay et al. (2007) modeled barite settling using continuum mechanics. The settling time, based on Stokes' law, was the starting point for the modeling work. Subsequently, the sliding of barite bed in an inclined wellbore was modeled. Afterwards, the model was adapted for a Bingham Plastic drilling fluid. When circulation and pipe rotation are halted, it is possible for particles to settle in a drilling mud (Paslay et al., 2007). Therefore, the authors assumed a no-circulation condition. For model development, the settling particles were considered to have contact and they created a layer of slurry called the "lower layer". The fluid above this layer is called the "upper layer". For a zero net movement along the length of the inclined annulus, the sliding of the lower layer results in the upward movement of the upper layer. To model the

mechanism, stress and velocity equations were written for the upper and lower layers, and the interface between them.

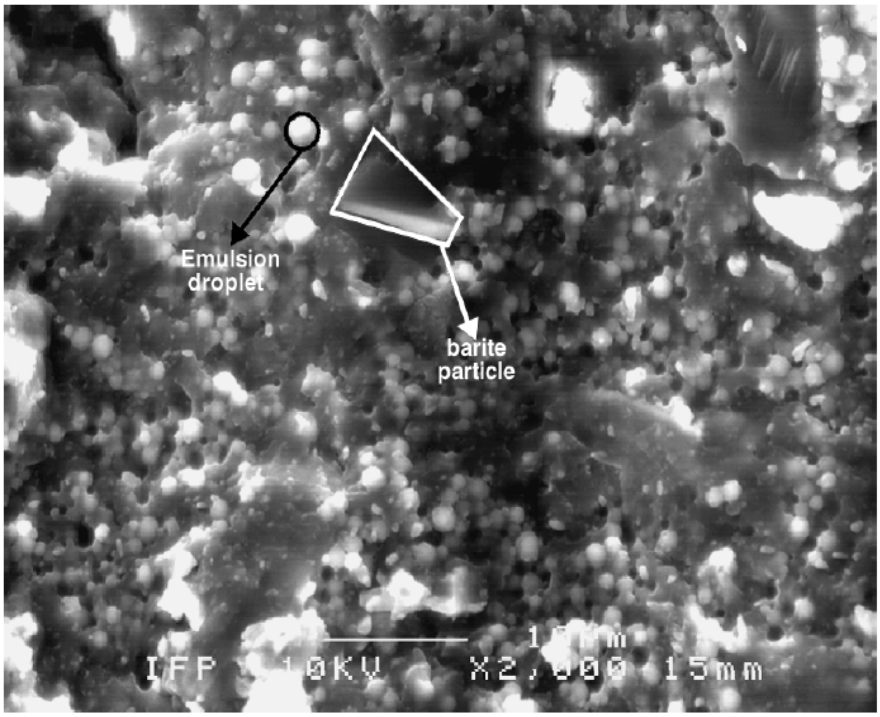

Fig. 2.22: Cryo-microscopic image of an OBM at X2500 magnification (Herzhaft et al., 2003)

Nguyen (2009) used the continuum method to model barite settling in Newtonian fluids. The Eulerian method was utilized for the two-phase (solid and liquid) particulate flow in an inclined pipe. For numerical solution, the resulting coupled and non-linear partial differential equations were discretized using the explicit scheme of the finite difference method.

The simulation of barite settling in horizontal and inclined annular sections was attempted by Hashemian (2012b). For modeling in a horizontal annulus, the laminar velocity profile of Herschel-Bulkley fluid in an eccentric annulus was obtained. The equation of motion for axial laminar flow is:

$$\frac{\partial}{\partial x}\left(\mu\frac{\partial w}{\partial x}\right)+\frac{\partial}{\partial y}\left(\mu\frac{\partial w}{\partial y}\right)=\frac{\partial P}{\partial z} \tag{2.33}$$

For axial flow, the shear rate is:

$$\dot{\gamma} = \sqrt{\left(\frac{\partial w}{\partial x}\right)^2 + \left(\frac{\partial w}{\partial y}\right)^2} \tag{2.34}$$

The viscosity in Eq. 2.33 is apparent viscosity in this case. The apparent viscosity of a Herschel-Bulkley fluid is given as:

$$\mu_a = \frac{\tau_y}{\dot{\gamma}} + K\dot{\gamma}^{n-1} \tag{2.35}$$

where w is fluid velocity in axial direction; μ_a is apparent viscosity.

Then, a particle tracking method (named Particle Elimination Technique) was implemented. Particle travelling path was forecasted while considering annular length, and particle diameter and location. Particles that reached the bottom of the annulus were taken off by setting their positions to stationary. Hence, density values were regularly updated. A lift force was added to the model for the purpose of matching simulation and experimental results. To model barite sag in an inclined annulus, an existing solution that explains the falling velocity of a liquid film down an inclined plane was used to account for the sliding of barite bed. Later, the sliding model was combined with the horizontal model to complete the model formulation for an inclined annulus.

Chapter 3: Experimental Studies on the Rheology of Oil-Based Muds

3.1. Overview

The experimental investigation conducted on the rheology of OBM and its continuous phase, at different shear rates and temperatures, is presented. With the application of nonlinear regression analysis, empirical models that link OBM rheological parameters to the volume fraction of the dispersed phase, apparent viscosity of the continuous phase, and temperature are developed for predicting the apparent viscosity of OBM. The rheological parameters and apparent viscosities of OBM and WBM are compared, and the revelation of the responsiveness of their viscous properties to temperature and shear rate is presented. This revelation disclosed why OBM is more vulnerable to barite sag occurrences than WBM.

3.2. Test Materials

The materials used for the preparation of the continuous phase, OBM, and WBM samples are presented in Tables 3.1 and 3.2. As shown in the tables, actual field formulations were used in designing the OBM and WBM samples. The organophilic clay and the prepared WBM samples are amine-treated bentonite and simple bentonite muds, respectively. Also, the xanthan gum used is dispersible.

3.3. Equipment Used

The OBMs were mixed with a high-shear laboratory mixer (Silverson L5M-A) and a blender while the WBMs were mixed with a regular high-speed mixer. A rotational viscometer (OFITE Model 900) was used for gathering rheological measurements. This equipment is displayed in Figs. 3.1 and 3.2.

3.4. Preparation of Test Samples

The different organophilic clay concentrations and oil-water ratios (OWRs) that were considered for making the continuous phase and OBM samples are shown in Table 3.3. For the continuous phase preparation, mineral oil, Surfactant-1, Surfactant-2, organophilic clay, and lime were blended with a high-shear laboratory mixer at a small speed (or shear rate). Afterwards, a proper mixing was achieved by increasing the speed. All the continuous phase samples were prepared following these procedures. The dispersed phase was made independently by mixing water and calcium chloride in a blender, and later transferred into the continuous phase while blending. At the end of mixing, the OBM was formed. For WBM preparation, water, soda ash, and bentonite were mixed with a regular high-speed mixer. Thereafter, xanthan gum, lime, and caustic soda were added while blending. Two WBM samples, with bentonite concentrations of 71.3 and 79.9 g/L, were made.

Table 3.1: Continuous phase and OBM formulation

Material	Function	Concentration
Mineral oil (Drakeol® 10 LT)	Base fluid	Varied
Surfactant-1	Emulsifier	20 g/L
Surfactant-2	Wetting agent	8.6 g/L
Organophilic clay	Viscosifier	Varied
Lime	Alkalinity	20 g/L
Calcium chloride	Dispersed phase salinity	82.7 g/L
Water	Dispersed phase	Varied

Table 3.2: WBM formulation

Material	Function	Concentration
Water	Base fluid	Varied
Soda ash	Hardness control	0.4 g/L
Bentonite	Viscosifier	Varied
Xanthan gum	Viscosifier	2.9 g/L
Lime	Alkalinity	8.6 g/L
Caustic soda	pH control	1.4 g/L

(a) **(b)** **(c)**

Fig. 3.1: Equipment used for mixing: a) high-shear laboratory mixer (Silverson L5M-A); b) regular high-speed mixer; and c) blender

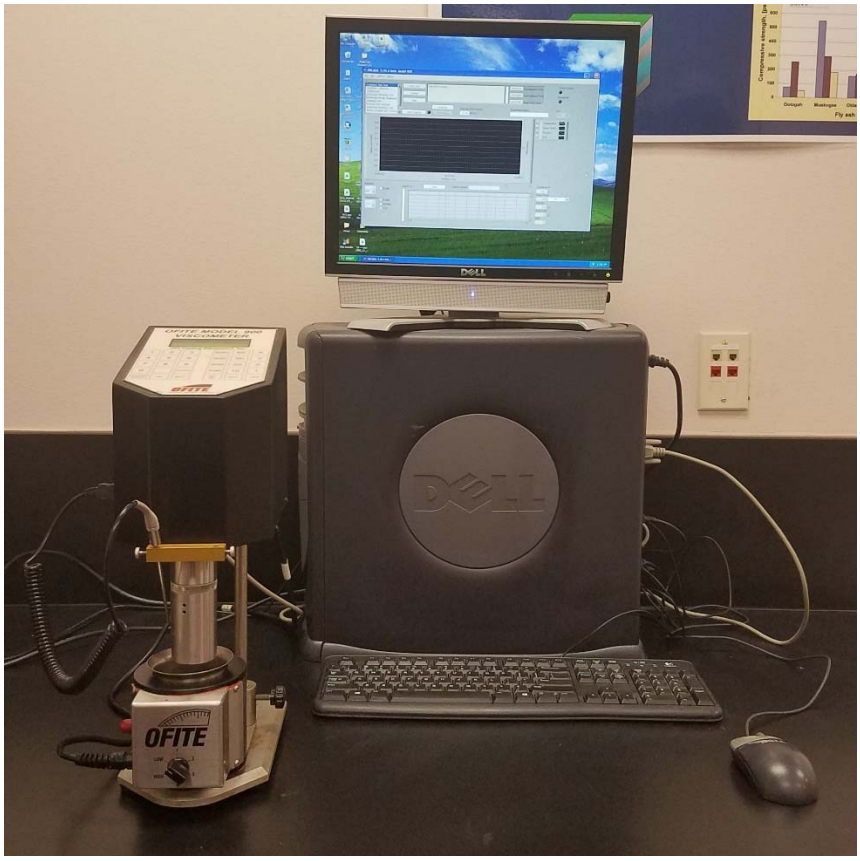

Fig. 3.2: Rotational viscometer (OFITE Model 900)

Table 3.3: Test matrix for continuous phase and OBM

Fluid system	Organophilic clay concentration (g/L)		
	2.9	8.6	17.1
Continuous phase for 65/35 OWR OBM	✓	✓	✓
Continuous phase for 75/25 OWR OBM	✓	✓	✓
Continuous phase for 85/15 OWR OBM	✓	✓	✓
OBM with 65/35 OWR	✓	✓	✓
OBM with 75/25 OWR	✓	✓	✓
OBM with 85/15 OWR	✓	✓	✓

3.5. Test Procedures

The rotational viscometer was calibrated with a standard fluid of known viscosity before rheological measurements were made. For each measurement, the test sample was poured into the test cup and set under the viscometer. Temperature and shear rate ranges of 24 – 87°C and

5.11 – 1021.8 s^{-1}, respectively were considered. However, a temperature range of 24 – 66°C was used for the WBMs. The reduced temperature range was due to water evaporation in the WBMs above 66°C, and this affected rheological measurements.

3.6. Results and Discussion

The flow behavior of OBM are studied. Also, the flow behavior of the continuous phase are examined to reveal the evolution of a rheological model for OBM fluid systems.

3.6.1. Rheology of Continuous Phase

The flow curves displayed in Figs. 3.3 and 3.4 demonstrate the effect of temperature on the flow properties of the continuous phase. The fluids manifest a small shear-thinning behavior that is describable with the Herschel-Bulkley model. All the continuous phases showed a viscosity reduction with temperature. Mineral oil is the major material in the continuous phase, and obviously, its response to an imposed situation will largely affect the flow behavior of the continuous phase. The viscosity of the mineral oil reduced as temperature increased; and as a result, the continuous phase became less viscous with temperature.

The effects of temperature and organophilic clay concentration on apparent viscosity of the continuous phase are shown in Figs. 3.5 and 3.6. Clearly, there is an improvement in apparent viscosity with increasing organophilic clay concentration. This trend is unsurprising because organophilic clay serves as a viscosifier. The shear-thinning behavior of the continuous phase improved as temperature increased. Additionally, the trend displayed in Figs. 3.5 and 3.6 was observed at other temperatures.

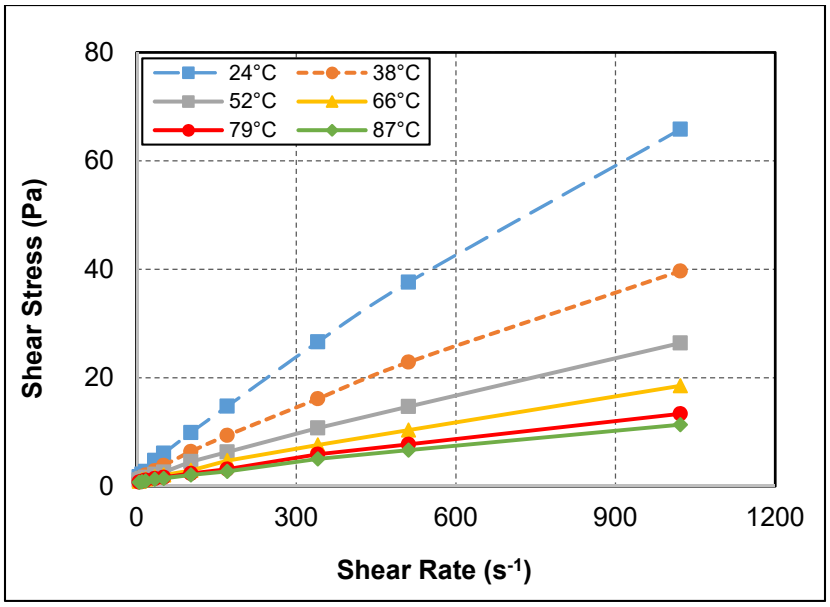

Fig. 3.3: Flow curves of the continuous phase for 65/35 OWR containing 17.1 g/L organophilic clay concentration

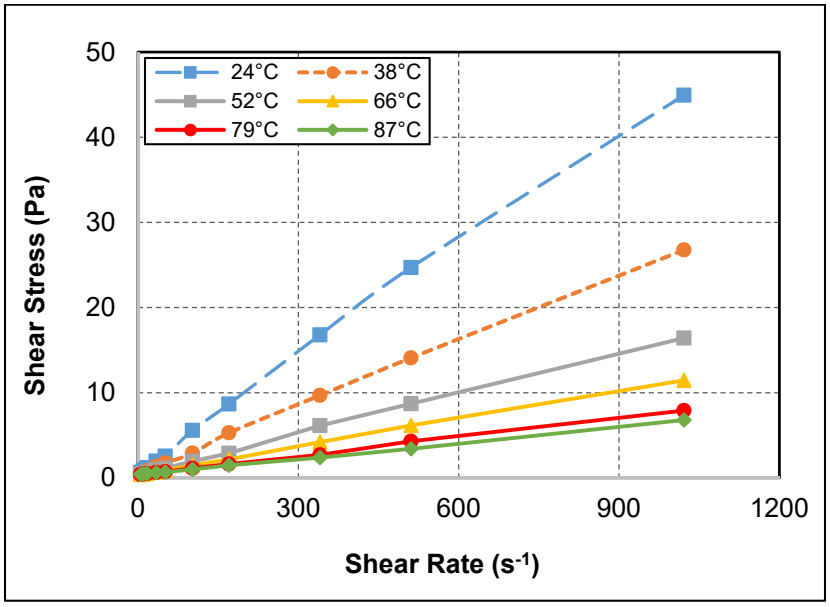

Fig. 3.4: Flow curves of the continuous phase for 85/15 OWR containing 8.6 g/L organophilic clay concentration

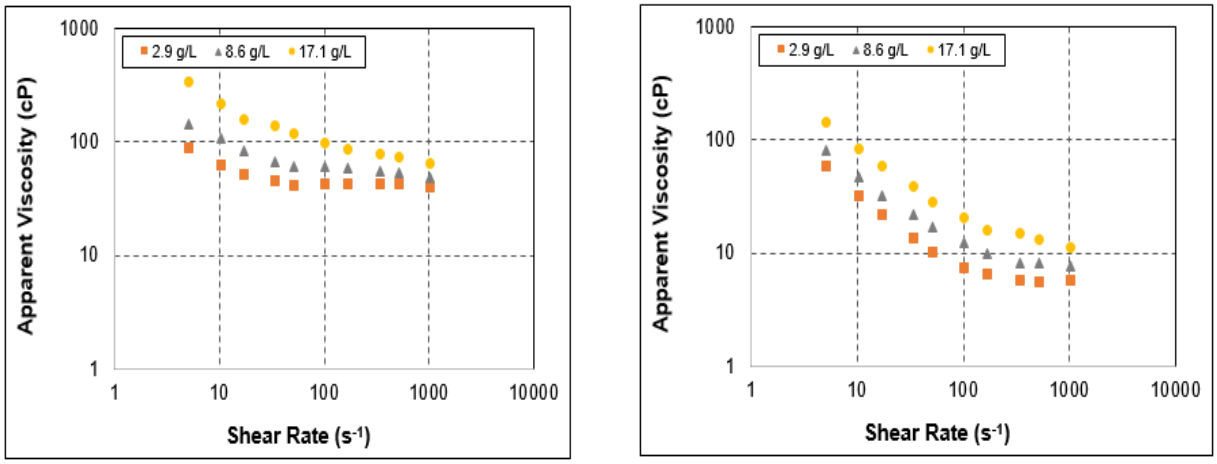

(a) (b)

Fig. 3.5: Apparent viscosity of the continuous phase (for 65/35 OWR) at various organophilic clay concentrations: a) at 24°C; and b) at 87°C

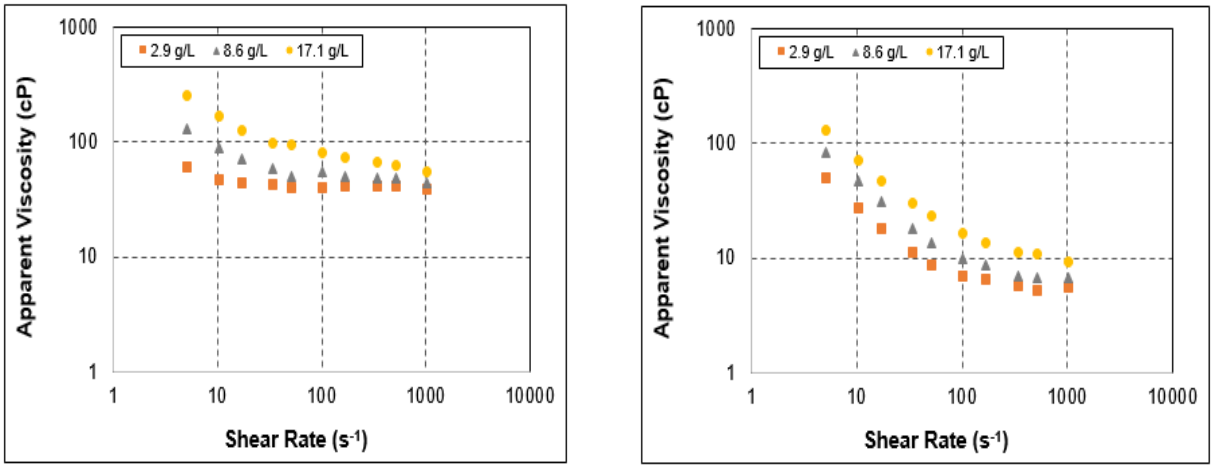

(a) (b)

Fig. 3.6: Apparent viscosity of the continuous phase (for 85/15 OWR) at various organophilic clay concentrations: a) at 24°C; and b) at 87°C

3.6.2. Rheology of Oil-Based Mud (OBM)

The flow curves presented in Figs. 3.7 and 3.8 show the effect of temperature on the flow properties of OBM. Evidently, the OBM samples exhibit a shear-thinning behavior that is best fitted with the Herschel-Bulkley model. All the OBMs showed a similar flow behavior with temperature. The flow properties of OBM rely on the continuous phase flow properties. Since

Figs. 3.3 and 3.4 show that the flow properties of the continuous phase reduced as temperature increased; thus, the observed trend of OBM flow properties with temperature is anticipated. Additionally, the solids added to OBM can undergo thermal degradation (Amani, 2012). According to Growcock and Frederick (1996), the surfactants can undergo thermal degradation too. Eventually, this can lead to a decrease in apparent viscosity.

The effects of organophilic clay concentration and OWR on the apparent viscosity of OBM are illustrated in Figs. 3.9 and 3.10. The trends in these figures are the same for all the tested OBMs at all temperatures. An increase in shear rate led to a decrease in the apparent viscosity of the continuous phase (Figs. 3.5 and 3.6). In the presence of a shear field, the water droplets can deform without breaking up into thin films (Sinclair, 1970). This deformation increases with increasing shear rate until a continuous film is created on the viscometer bob. The deformation is a result of flow induced changes in the droplets' structure, and it affects the emulsion's resilience to movement until a self-consistent dynamic steady condition is attained (Mason et al., 1996). An additional increase in shear rate would cause the water droplets to arrange themselves in strings and clusters, and the result would be a reduction in viscosity (Saasen, 2002). Apparent viscosity increased as organophilic clay concentration and OWR increased, but, the effect of OWR is greater (Figs. 3.9 and 3.10). In emulsions, the fluid droplets (even at low concentrations) display a behavior that is similar to the one exhibited by dispersion of solids in suspensions. According to Mason et al. (1996), this might be attributed to the surfactant's surface elasticity.

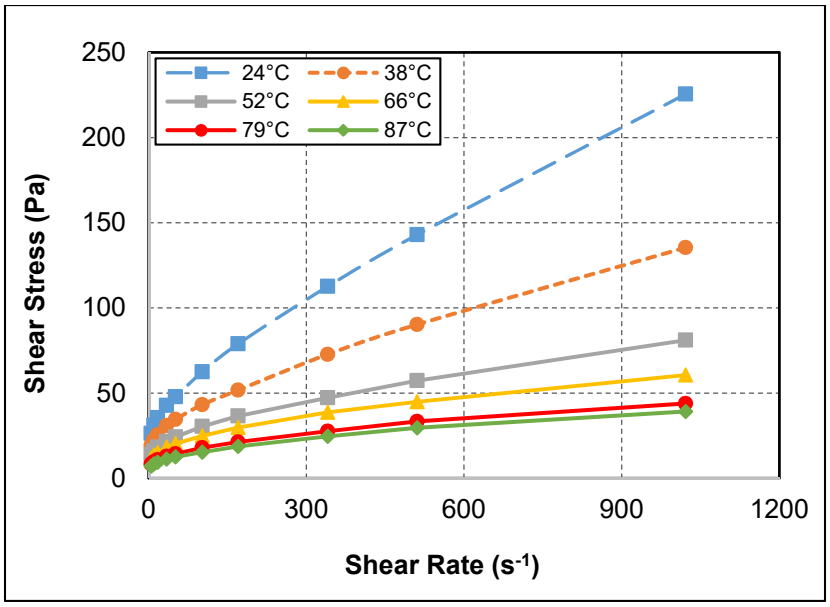

Fig. 3.7: Flow curves of OBM (with 65/35 OWR) containing 2.9 g/L organophilic clay concentration

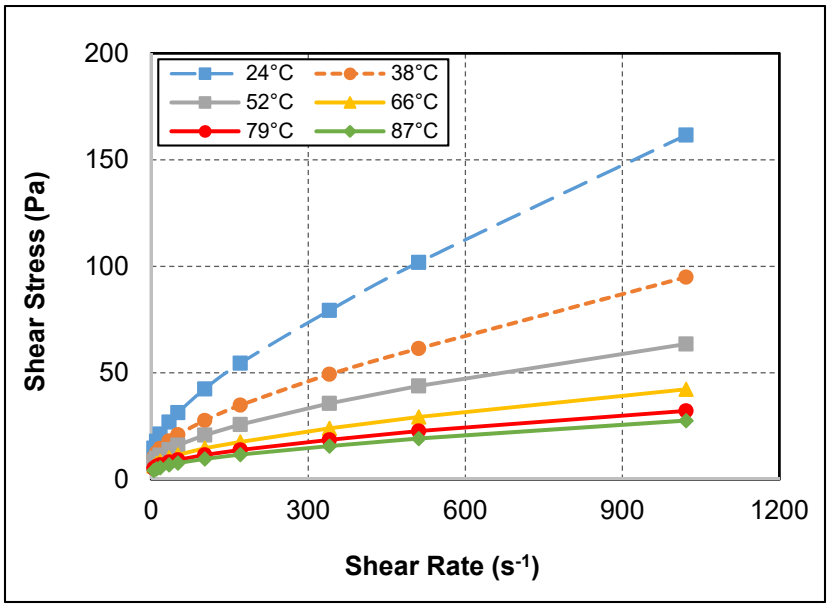

Fig. 3.8: Flow curves of OBM (with 75/25 OWR) containing 8.6 g/L organophilic clay concentration

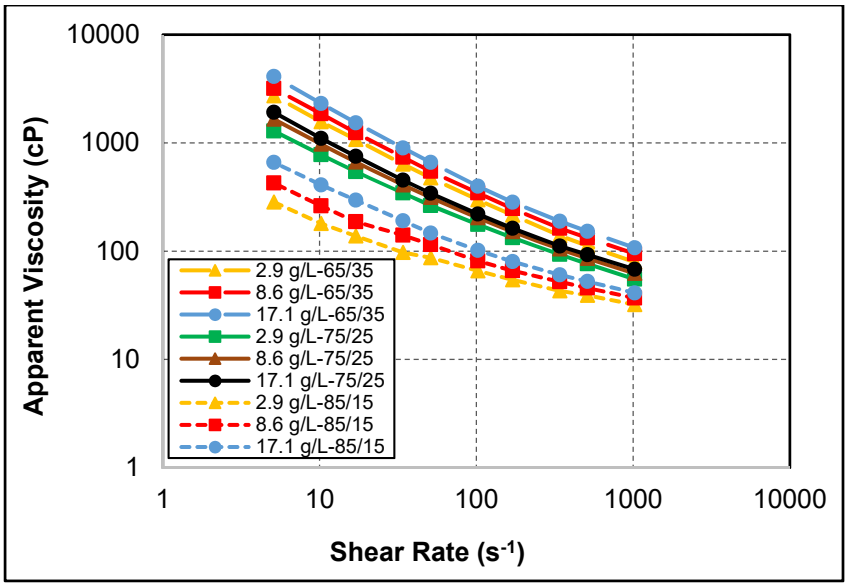

Fig. 3.9: Effects of organophilic clay concentration and OWR on the apparent viscosity of OBM at 52°C

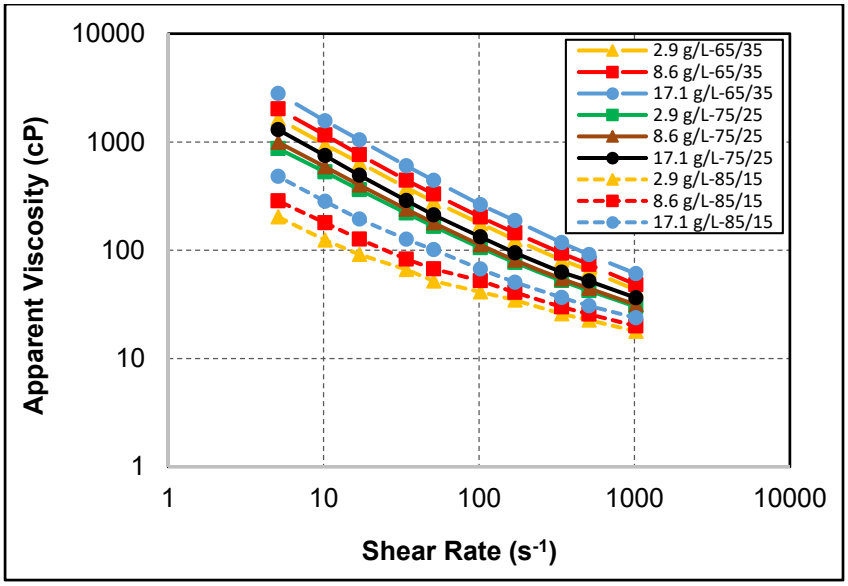

Fig. 3.10: Effects of organophilic clay concentration and OWR on the apparent viscosity of OBM at 79°C

3.7. Development of Rheological Models

The existence of predictive rheological models for OBM will minimize the amount of tests needed to design a new OBM system. Dimensionless OBM rheological parameters (normalized yield stress, normalized consistency index, and normalized fluid behavior index) are created

using nonlinear regression analysis. These parameters are connected to the volume fraction of the dispersed phase, apparent viscosity of the continuous phase at a reference temperature (24°C), and temperature. Since the volume fraction of the dispersed phase and the apparent viscosity of the continuous phase greatly affect OBM rheology, so, they are used for OBM modeling at the reference temperature. Afterwards, the empirical modeling was completed by including temperature. The rheological parameters of the investigated OBM samples are presented in Appendix A.

3.7.1. Modeling OBM Rheological Parameters at Reference Temperature

The volume fraction of the dispersed phase and the apparent viscosity of the continuous phase have a significant effect on OBM rheology at the reference temperature. Therefore, the rheological parameters at the reference temperature are linked to them. The yield stress at the reference temperature, τ_{yo}, is expressed as:

$$\tau_{yo} = A_{\tau yo}\phi_d^2 + B_{\tau yo}\phi_d + C_{\tau yo} \quad (3.1)$$

where the unit of τ_{yo} is Pa; ϕ_d is volume fraction of the dispersed phase; $A_{\tau yo}$, $B_{\tau yo}$, and $C_{\tau yo}$ are fluid parameters with the unit of Pa, and they are related to the apparent viscosity of the continuous phase (μ_{CP}) that is evaluated at the reference temperature and a shear rate of 511 s^{-1}. The unit of μ_{CP} is cP. The correlations are expressed as:

$$A_{\tau yo} = 1.6317\mu_{CP}^2 - 167.27\mu_{CP} + 4455.3 \quad (3.2)$$

$$B_{\tau yo} = -0.7263\mu_{CP}^2 + 75.347\mu_{CP} - 1903.1 \quad (3.3)$$

$$C_{\tau yo} = 0.0677\mu_{CP}^2 - 6.9433\mu_{CP} + 170.51 \quad (3.4)$$

Similarly, the consistency index at the reference temperature, K_o, is linked to ϕ_d and μ_{CP}. The correlation is given by:

$$K_o = A_{Ko}\phi_d - B_{Ko} \quad (3.5)$$

where the unit of K_o is Pas^n; A_{Ko} and B_{Ko} are fluid parameters with the unit of Pas^n, and they are connected to μ_{CP}. The correlations are expressed as:

$$A_{Ko} = -0.0006\mu_{CP}^2 + 0.1137\mu_{CP} + 2.8367 \quad (3.6)$$

$$B_{Ko} = 0.0037\mu_{CP} + 0.4574 \quad (3.7)$$

The fluid behavior index at the reference temperature, n_o, is mainly affected by phase composition. Hence:

$$n_o = A_{no}\phi_d^2 - B_{no}\phi_d + C_{no} \quad (3.8)$$

where the dimensionless fluid parameters are: A_{no} = 6.3351; B_{no} = 3.4843; C_{no} = 1.1774. Equations 3.1, 3.5, and 3.8 are valid for ϕ_d in the range of 0.14 – 0.32. Also, μ_{CP} is in the range of 41 – 68 cP.

The predictions from the yield stress and consistency index models are compared with the experimental data (Figs. 3.11 and 3.12). Evidently, reasonable predictions are made. There is no error in the prediction of n_o.

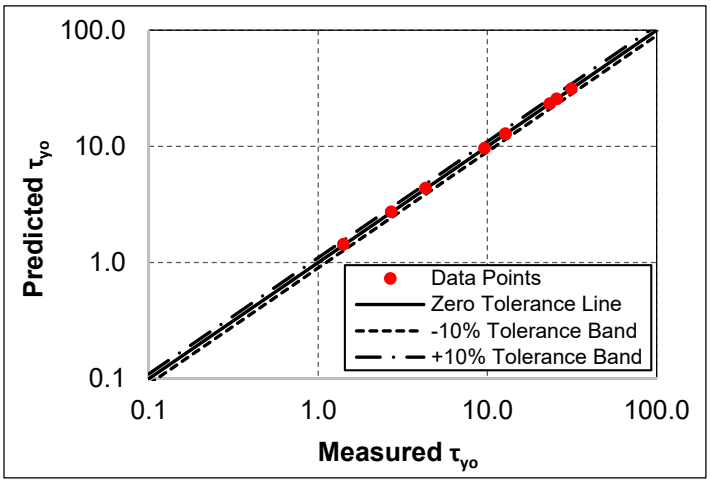

Fig. 3.11: Measured and predicted yield stress at the reference temperature

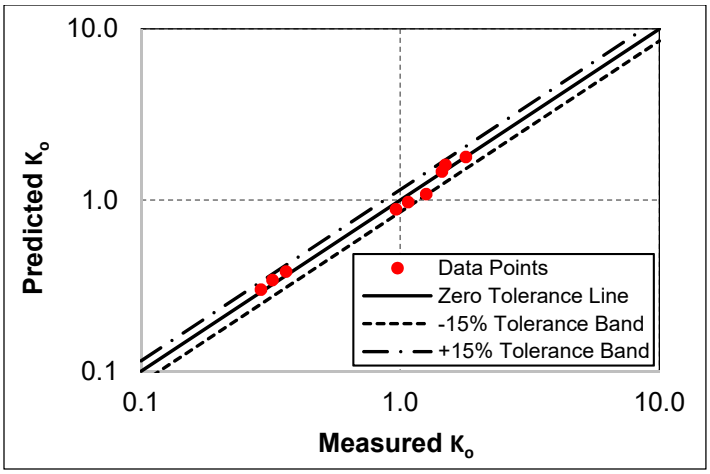

Fig. 3.12: Measured and predicted consistency index at the reference temperature

3.7.2. Modeling OBM Rheological Parameters at Elevated Temperature

The effect of temperature is significant on OBM rheology. Consequently, the rheological parameters of the mud show a considerable variation as temperature increased. The normalized yield stress is connected to temperature as:

$$\frac{\tau_y}{\tau_{yo}} = A_{\tau y} T^{-B_{\tau y}} \tag{3.9}$$

where τ_y is yield stress of the OBM at temperature T; $A_{\tau y}$ and $B_{\tau y}$ are fluid parameters that vary with ϕ_d. Hence:

$$A_{\tau y} = 167.8\phi_d^2 - 20.566\phi_d + 7.578 \tag{3.10}$$

$$B_{\tau y} = 1.426\phi_d + 0.445 \tag{3.11}$$

Likewise, the normalized consistency index is expressed as:

$$\frac{K}{K_o} = A_K - B_K T + C_K T^2 - D_K T^3 \tag{3.12}$$

where K is consistency index of the OBM at temperature T; A_K through D_K are fluid parameters that vary with ϕ_d. The relationships are expressed as:

$$A_K = 73.595\phi_d^2 - 28.695\phi_d + 4.2688 \tag{3.13}$$

$$B_K = 5.2708\phi_d^2 - 1.9874\phi_d + 0.2107 \quad (3.14)$$

$$C_K = 0.1116\phi_d^2 - 0.0407\phi_d + 0.00385 \quad (3.15)$$

$$D_K = \frac{1}{\alpha_K + \beta_K * \ln\phi_d} \quad (3.16)$$

where $\alpha_K = -1302609.92732119$; $\beta_K = -1206211.22427271$. The number of decimal places in the empirical constants (α_K and β_K) are retained because of the sensitivity of D_K, thus, accurate predictions are ensured.

Also, the normalized fluid behavior index is expressed as:

$$\frac{n}{n_o} = A_n T^2 - B_n T + C_n \quad (3.17)$$

where n is fluid behavior index of the OBM at temperature T; A_n, B_n, and C_n are fluid parameters that vary with ϕ_d as:

$$A_n = -0.0043\phi_d^2 + 0.0023\phi_d - 0.000242 \quad (3.18)$$

$$B_n = -0.3086\phi_d^2 + 0.1842\phi_d - 0.0171 \quad (3.19)$$

$$C_n = -4.7407\phi_d^2 + 3.1619\phi_d + 0.7076 \quad (3.20)$$

Equations 3.9, 3.12, and 3.17 are valid for a temperature range of 24 – 87°C.

The predictions of normalized rheological parameters are compared with the experimental data in Fig. 3.13. The minimal discrepancies between the predicted and measured values show the achievement of a reasonable agreement. For making predictions, OBM rheological parameters should be obtained from the normalized rheological parameters at a desired temperature. Thereafter, the Herschel-Bulkley model should be utilized in evaluating the apparent viscosity of OBM. The evaluation should be within the stated shear rate limits. Generally, the prediction of OBM apparent viscosity is found to be reasonable (Fig. 3.14).

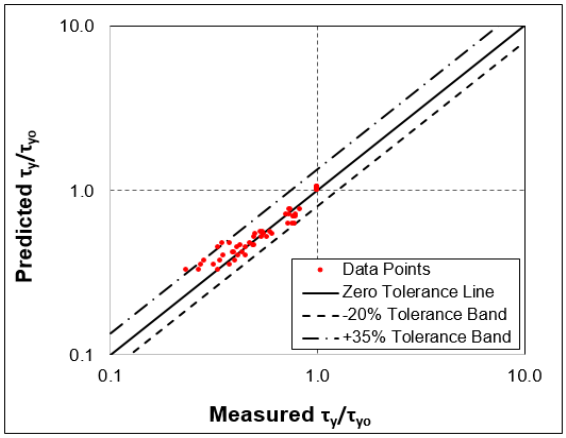

(a)

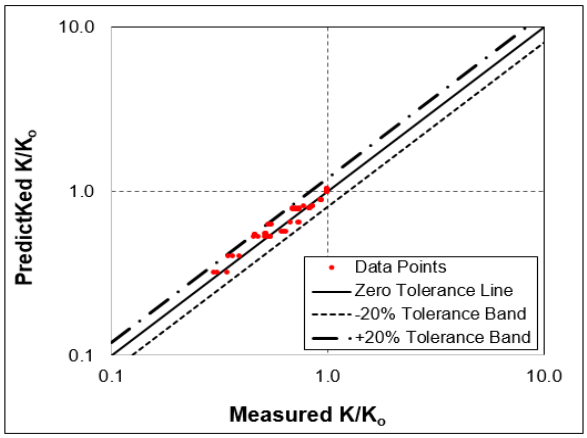

(b)

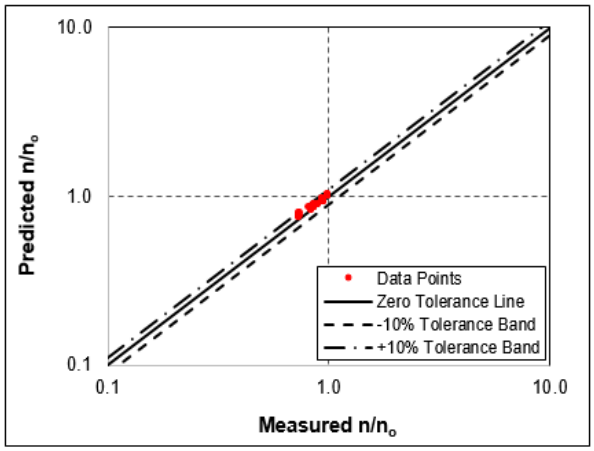

(c)

Fig. 3.13: Measured and predicted rheological parameters: a) normalized yield stress; b) normalized consistency index; and c) normalized fluid behavior index

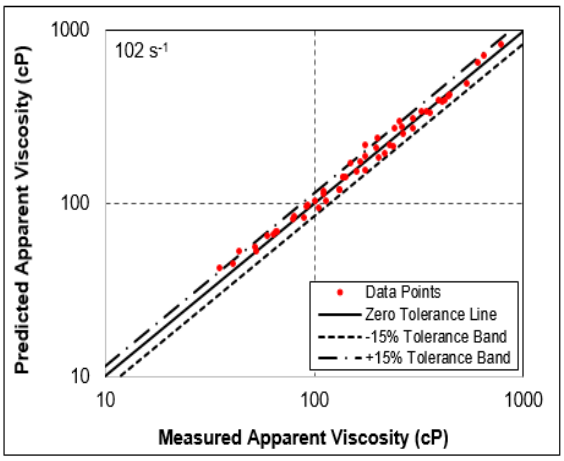

(a)

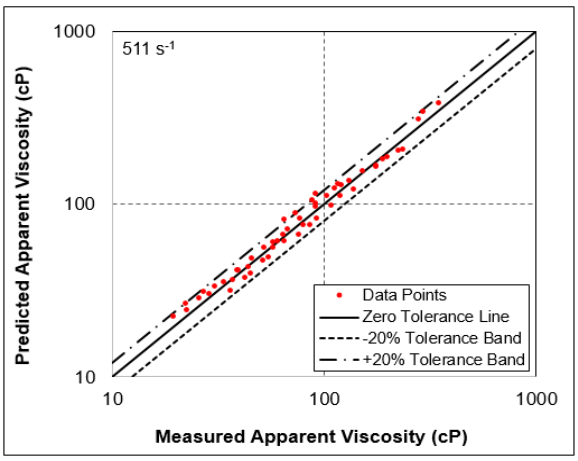

(b)

Fig. 3.14: Measured and predicted apparent viscosity of OBM: a) at 102 s^{-1}; and b) at 511 s^{-1}

3.8. Comparison of Rheological Parameters of OBM and WBM

Similar to the OBMs, the WBMs showed a shear-thinning behavior as displayed in Fig. 3.15. Two WBMs, with bentonite concentrations of 71.3 and 79.9 g/L, were investigated while changing temperature. The flow properties of the WBMs varied with temperature (Fig. 3.15). The apparent viscosity of the WBMs reduced with temperature. The Herschel-Bulkley model best describes the shear-thinning behavior of the WBMs at all temperatures.

A comparison of the normalized rheological parameters of OBMs and WBMs is shown in Fig. 3.16. These parameters reveal the responsiveness of the apparent viscosity of the muds to changes in temperature. The normalized yield stress of both OBM and WBM reduced as temperature increased; however, the rate of reduction is mostly higher for OBM (Fig. 3.16a). All the OBMs displayed this trend. In comparison to WBM, Fig. 3.16a suggests that the OBM experiences more loss in its ability to suspend solids as temperature increases. Another interpretation is that the OBM becomes more vulnerable to barite sag occurrences than WBM. Another fascinating observation is that the normalized consistency index of OBM reduced as temperature increased while that of WBM increased with temperature (Fig. 3.16b). All the OBMs displayed this trend. Again, this observation corroborates prior findings that suggest that the OBM loses its ability to suspend solids as temperature increases. For normalized fluid behavior index, both OBM and WBM manifested a similar trend with temperature ((Fig. 3.16c).

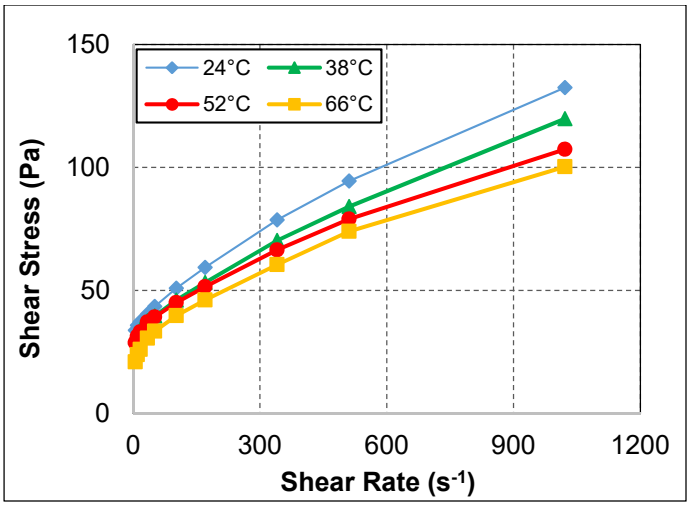

Fig. 3.15: Flow curves of WBM containing 79.9 g/L bentonite

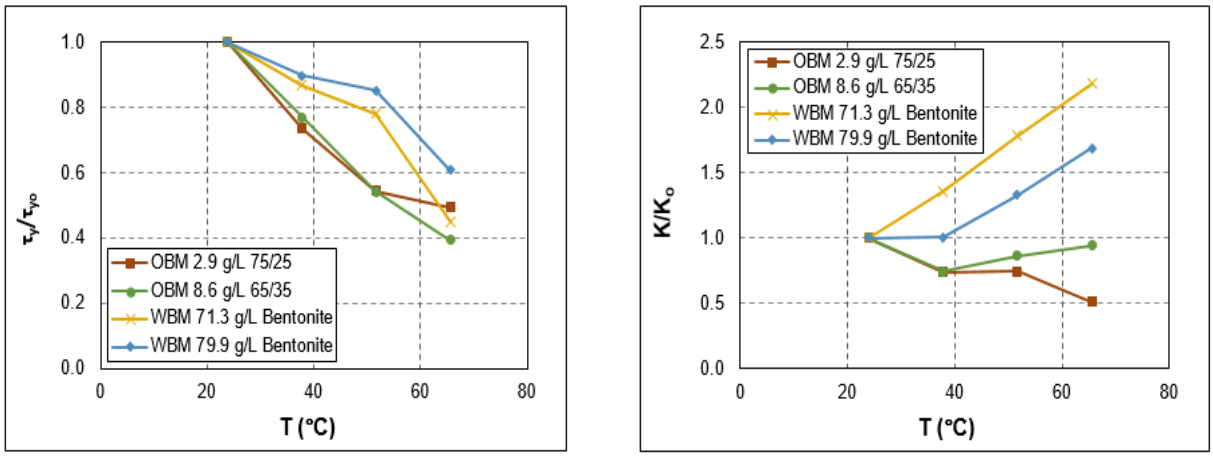

(a) **(b)**

(c)

Fig. 3.16: Rheological parameters of OBM and WBM as a function of temperature: a) normalized yield stress; b) normalized consistency index; and c) normalized fluid behavior index

For a more precise explanation, the apparent viscosities of both mud systems are further compared in terms of normalized apparent viscosity. Like before, the shear-thinning behaviors of the OBMs and WBMs are revealed in Fig. 3.17. Though, all the mud samples displayed this trend; but, the apparent viscosity of WBM showed stability with temperature. As temperature increased, the WBM resisted thermal-related thinning (Fig. 3.17a). The normalized apparent viscosity is independent of temperature up to 52°C (Fig. 3.17a). Also, Fig. 3.17a revealed that the rate of reduction in apparent viscosity, owing to shear deformation, reduced for WBM at elevated temperature (66°C). All the investigated WBMs showed this trend. Evidently, the WBM rheological parameters illustrated in Fig. 3.16 demonstrated a collaborative effect in Fig. 3.17a. For the OBMs, thermal thinning was observed with temperature, and this happened over the range of shear rate considered in this work (Fig. 3.17b through 3.17d). This means that the normalized apparent viscosity relies on temperature. All the OBMs displayed this trend, which agrees with the performance of the OBM rheological parameters illustrated in Fig. 3.16.

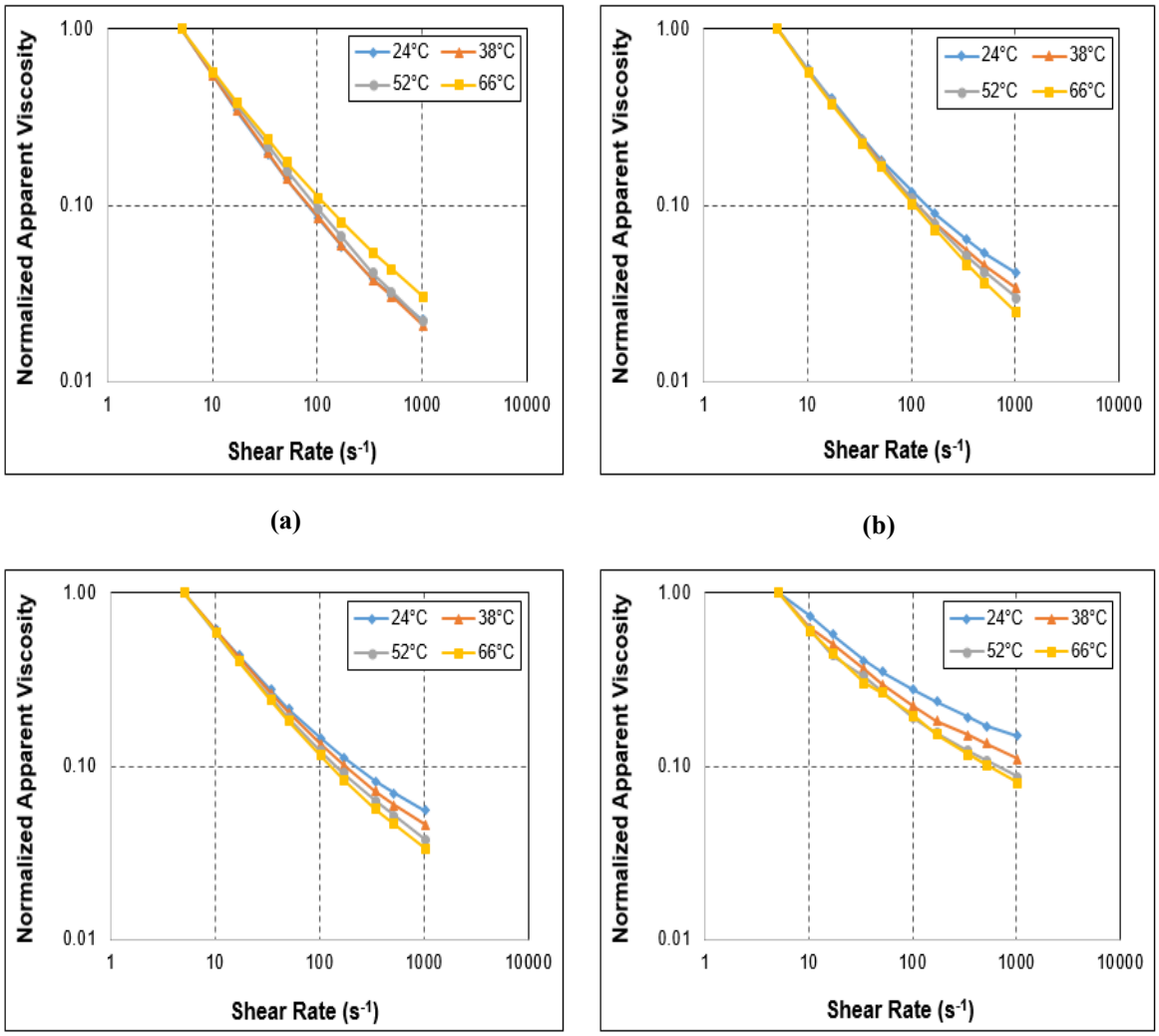

Fig. 3.17: Normalized apparent viscosity of: a) WBM containing 71.3 g/L bentonite; b) OBM with 8.6 g/L organoclay and 65/35 OWR; c) OBM with 8.6 g/L organoclay and 75/25 OWR; and d) OBM with 8.6 g/L organoclay and 85/15 OWR

Chapter 4: Study of Barite Sag using Rotational Viscometer

4.1. Overview

Barite samples with different particle size distribution were prepared by sieving commercial barite, and used to create weighted OBM samples that had varying particle size ranges. Apparent viscosity measurements of weighted OBMs were gathered with a rheometer. Then, barite sag studies were conducted (at 49°C) by applying the Viscometer Sag Shoe Test (VSST) method at varying mean particle size and rotational speed. The results are reported in this chapter.

4.2. Test Materials

The materials and the typical field formulation used for the preparation of the weighted OBM samples are presented in Table 4.1. Besides the regular barite (barite sample with untampered size distribution), two additional barite types were prepared by sieving. The details of the different barite types are shown in Table 4.2.

Table 4.1: OBM formulation for 75/25 OWR and 1413.8 kg/m^3 mud weight

Material	Function	Concentration
Mineral oil (Drakeol® 10 LT)	Base fluid	0.7001 L/L
Surfactant-1	Emulsifier	20 g/L
Surfactant-2	Wetting agent	8.6 g/L
Organophilic clay	Viscosifier	8.6 g/L
Lime	Alkalinity	20 g/L
Calcium chloride	Dispersed phase salinity	82.7 g/L
Water	Dispersed phase	0.2334 L/L
Barite	Weighting material	736.5 g/L

Table 4.2: Barite types used in this study

Barite type	Particle size range (µm)	D50 (µm)
Regular barite	0 – 425 µm	82
Medium barite	0 – 125 µm	63
Fine barite	0 – 75 µm	45

4.3. Equipment Used

A vibrating sieve-shaker equipped with 10 sieves (mesh sizes: 425, 250, 180, 125, 106, 90, 75, 53, 45, and 25 μm) was used to prepare barite samples with different particle size distributions. The unweighted OBMs were mixed with a high-shear laboratory mixer (Silverson L5M-A) and a blender. The weighted OBMs were mixed with a regular high-speed mixer. Apparent viscosity measurements were gathered with a rheometer (Bohlin). The VSST was conducted using the Sag Shoe, thermocup, syringe, cannula, timer, sensitive weight-balance, and rotational viscometer (OFITE Model 900). The Sag Shoe and the rotational viscometer are displayed in Figs. 2.3 and 3.2, respectively. The vibrating sieve-shaker and its sieves, Bohlin rheometer, thermocup, syringe, and cannula are shown in Figs. 4.1 through 4.3.

Fig. 4.1: Vibrating sieve-shaker and sieves

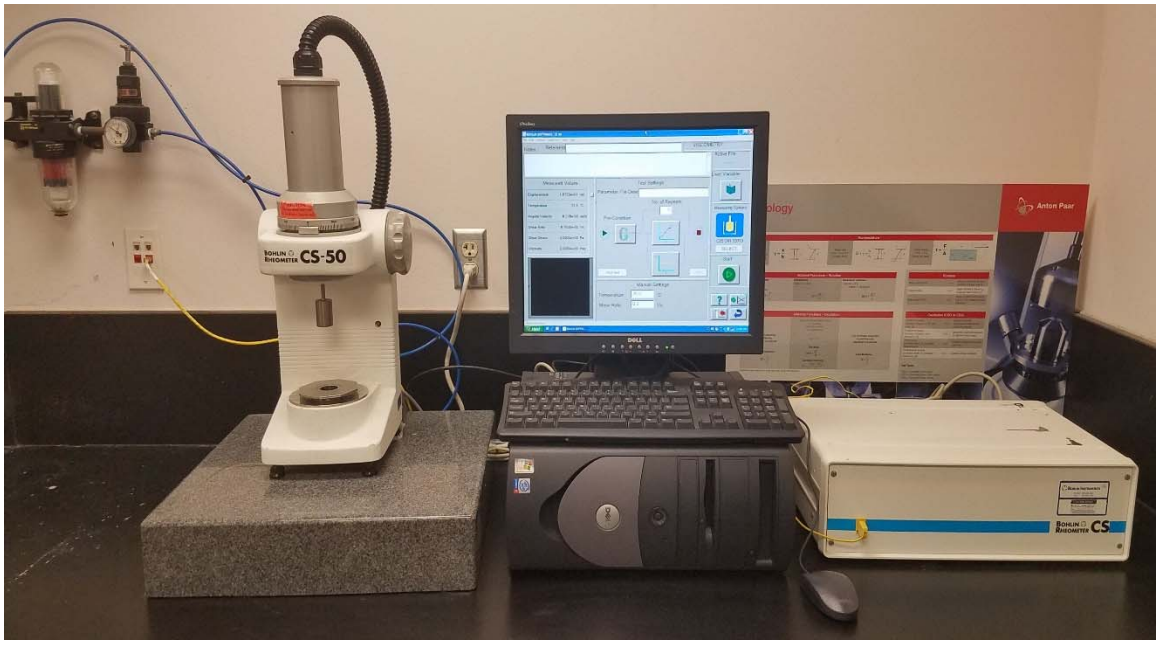

Fig. 4.2: Bohlin rheometer

(a) **(b)** **(c)**

Fig. 4.3: Equipment used for VSST: a) thermocup; b) syringe; and c) cannula

4.4. Preparation of Test Samples

The preparation procedures for the unweighted OBMs were described in Section 3.4. A OWR of 75/25 was used for all the OBM samples. After preparing an unweighted OBM, barite was added (at the concentration specified in Table 4.1) while mixing with a regular high-speed mixer. A weighted OBM was the result of the mixing. The different barite types resulted in the same mud weight of approximately 1413.8 kg/m^3.

4.5. Test Procedures

The test procedures followed during the investigation are described below.

4.5.1. Particle Size Distribution Test

The pan was placed at the bottom and sieves with different mesh sizes were stacked (starting with the smallest mesh size) on each other. The required mass of barite was loaded in the top sieve, and the stacked sieves were secured by clamping. Sieving time and amplitude was set, and testing commenced. At the end of sieving, the stack was unclamped and the mass of barite retained by each mesh and the pan was measured. These procedures were repeated for the other two barite types, and the undesired particle size ranges were sieved out.

4.5.2. Apparent Viscosity Measurements

The Bohlin rheometer was calibrated with a standard viscosity fluid before OBM viscosity measurements were gathered. The bob and cup geometry was used for testing fluid rheology at a temperature of 49°C. A 13 mL OBM sample was loaded in the cup, and tested at a target shear rate range of 0.05262 – 1022 s^{-1}.

4.5.3. VSST Method

For VSST, the procedures presented in Ofite Sag Shoe instruction manual were followed. The Sag Shoe was inserted in the thermocup, and both were placed on the plate of the rotational viscometer. The plate was raised and stopped when the top of the Sag Shoe touched the bottom of the rotor sleeve. The plate was locked in place, and the position of the top of the locking mechanism was marked on the support leg. The plate was released and lowered, and a distance of 7 mm was measured and marked in the downward direction from the first mark. With the Sag Shoe in the thermocup, both were pre-heated to 49°C. Also, the OBM sample was pre-heated to 49°C. A 140 mL OBM sample was poured into the thermocup, and the plate was raised and

locked in place when the top of the locking mechanism reached the lower mark. A rotational speed of 100 rpm and time of 30 minutes was set, and sag testing commenced. While testing was progressing, the syringe and the cannula was used to draw more than 10 mL sample from the original OBM sample. Then, the plunger was pushed to the 10 mL mark to eliminate entrapped air. The surfaces of the syringe and the cannula were cleaned, and the weight was measured on a sensitive weight-balance and recorded as WT1 in grams. When the testing time elapsed, the rotational viscometer was stopped and OBM sample was taken from the collection well of the Sag Shoe using the syringe and the cannula as explained above. This time, the weight measured was recorded as WT2 in grams.

4.6. Results and Discussion

The particle size ranges contained in the regular barite that was used is presented in Table 4.3. Also, two additional barite types were prepared. The apparent viscosity of OBM was obtained for a wide range of shear rate. The effects of particle size and rotational speed on barite sag were studied.

4.6.1. Particle Size Distribution

Table 4.3 shows the particle size distribution of regular barite. It is obvious from the results that large particle sizes in the range of 250 μm and above are fewer in the regular barite samples. Figure 4.4 shows the particle size distribution of regular barite that was obtained from the average results of the three experiments presented in Table 4.3. The D50 of regular barite is 82 μm (Fig. 4.4). The particle size distribution of the remaining two barite types, presented in Table 4.2, are illustrated in Fig. 4.5. The D50 of medium and fine barites, determined from Fig. 4.5, are 63 and 45 μm, respectively. The D50 values are derived from the data points (Figs. 4.4 and 4.5), but trend lines are fitted in order to have smooth curves.

Table 4.3: Particle size distribution of regular barite

Experiment number	1	2	3				
Initial weight (g)	500	500	500				
Mesh size (µm)	Mass retained (g)			Average mass retained (g)	% retained	Cumulative % retained	Cumulative% finer
425	0	0	0	0	0	0	100
250	8	9.6	8.5	8.7	1.74	1.74	98.26
180	28.5	31.5	35	31.7	6.33	8.07	91.93
125	60.2	60.6	67.4	62.7	12.55	20.62	79.38
106	70.6	67.3	74.8	70.9	14.18	34.80	65.20
90	39.4	42.8	50.9	44.4	8.87	43.67	56.33
75	66.5	64.5	64.7	65.2	13.05	56.72	43.28
53	28.9	28.1	40.4	32.5	6.49	63.21	36.79
45	76.4	80.7	59.2	72.1	14.42	77.63	22.37
25	88.9	88.1	75.9	84.3	16.86	94.49	5.51
Pan (< 25)	28.6	22.9	18.5	23.3	4.67	99.16	0.84
	496	**496.1**	**495.3**	**495.8**			

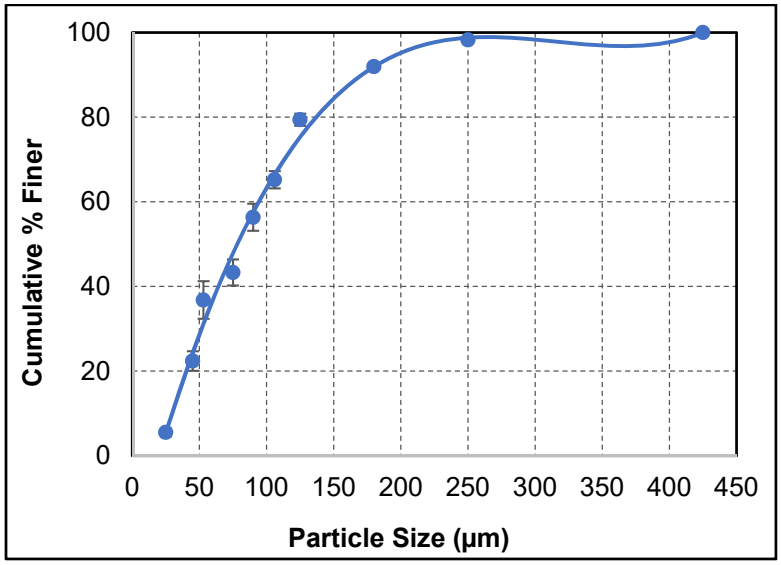

Fig. 4.4: Particle size distribution curve of regular barite (D50 = 82 µm)

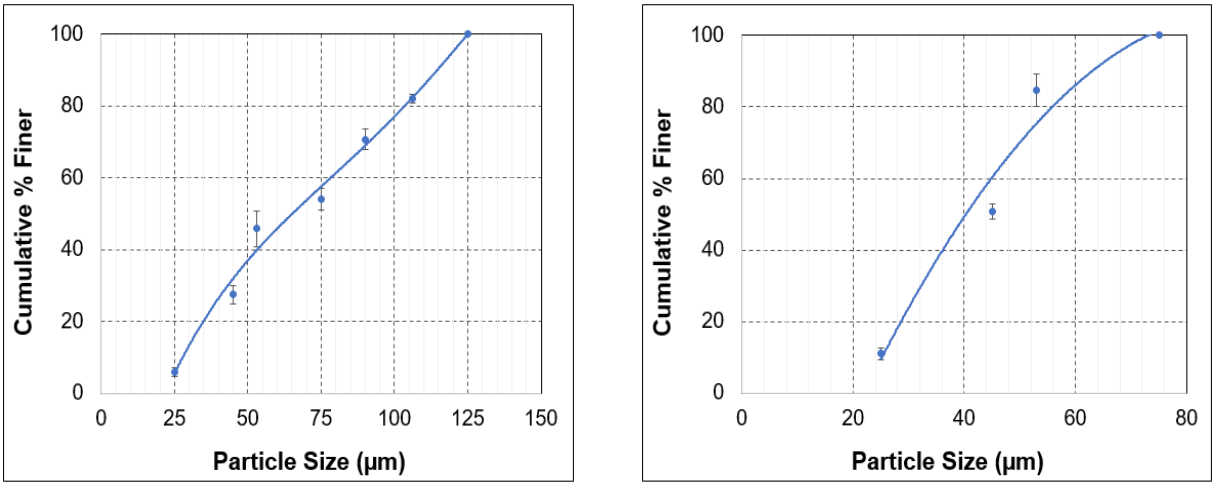

(a) **(b)**

Fig. 4.5: Particle size distribution curve of: a) medium barite (D50 = 63 µm); and b) fine barite (D50 = 45 µm)

4.6.2. Apparent Viscosity of OBM

The flow curves depicted in Fig. 4.6 show the effects of barite and particle size distribution on the apparent viscosity of the OBMs. Each apparent viscosity experiment was performed more than once, hence, average results are presented in Fig. 4.6. It is obvious that the addition of barite led to a significant increase in the apparent viscosity of the base mud. However, the type of barite used gave a minor change in apparent viscosity. The shear-thinning behavior of the OBM samples is evident in Fig. 4.6. The scientific explanation of OBM shear-thinning behavior has been presented in the work of Fakoya and Ahmed (2018).

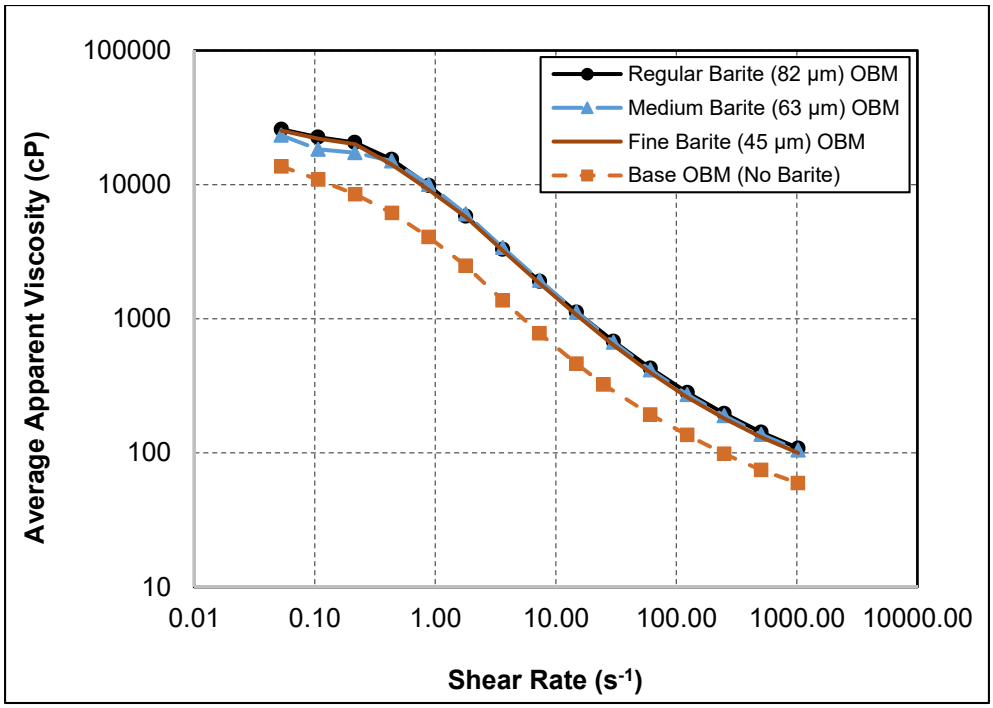

Fig. 4.6: Effects of barite and particle size distribution on the apparent viscosity of OBM at 49°C

4.6.3. Effects of Particle Size and Rotational Speed on Barite Sag

Figures 4.7 and 4.8 illustrate the effects of particle size and rotational speed on barite settling. In this method, the barite deposited at the bottom of the thermocup (collection well of the Sag Shoe) at the end of 30 minutes testing time is converted to VSST measurement according to the Ofite Sag Shoe manual [VSST (kg/m^3) = 100 (WT2 – WT1)]. Each sag experiment was performed more than two times, hence, average data points are presented in Figs. 4.7 and 4.8. Barite sag increased with particle size and rotational speed. From Fig. 4.6, it is evident that the apparent viscosity of the OBMs decreased with shear rate; thus, particles settled faster when rotational speed (shear rate) was increased due to the reduction of apparent viscosity.

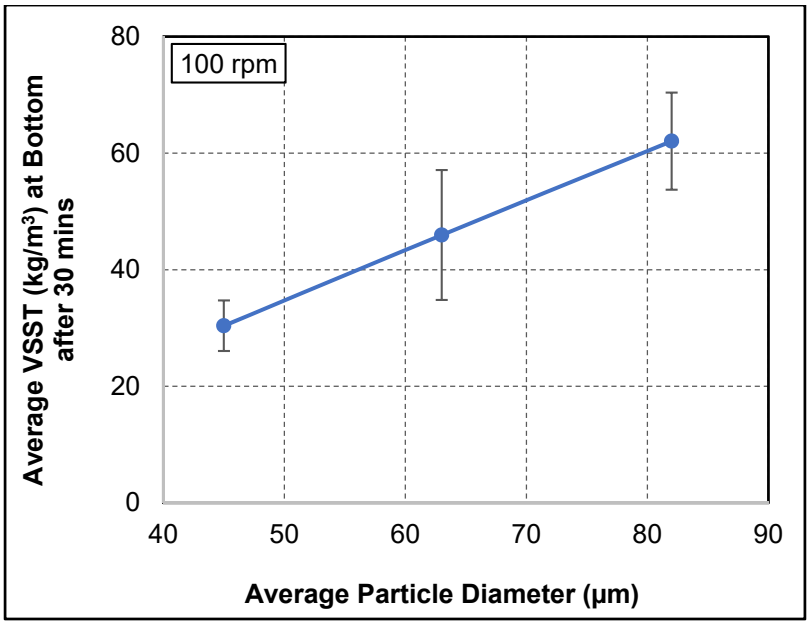

Fig. 4.7: Effect of particle size on barite sag at 49°C

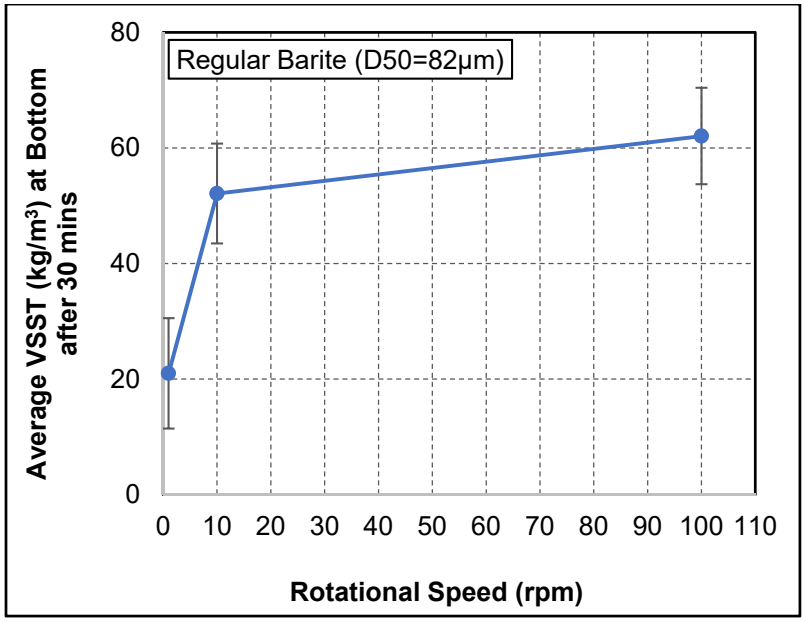

Fig. 4.8: Effect of rotational speed on barite sag at 49°C

Chapter 5: Experimental Studies of Barite Sag in Flow Loop

5.1. Overview

A flow loop was designed, and numerous weighted OBMs were prepared with regular barite to achieve the required volume of test sample. Barite sag studies were conducted (at 49°C) in the flow loop at different pipe rotational speeds and inclination angles. Normalized mud densities were calculated from differential pressure readings, and the results from the top and bottom sections of the mud column are presented.

5.2. Test Materials

The materials and the typical field formulation used for the preparation of weighted OBMs are presented in Table 4.1. For these tests, the barite type considered is the regular barite (barite sample with untampered size distribution), and with D50 of 82 μm.

5.3. Equipment Used

The unweighted OBMs were mixed with a high-shear laboratory mixer (Silverson L5M-A) and a blender. The weighted OBMs were mixed with a regular high-speed mixer. Barite sag studies were conducted with a flow loop.

5.4. Flow Loop Setup

The flow loop (Figs. 5.1 and 5.2) consists of: i) test section (ID = 0.0762 m) that is equipped with an inner rotating concentric-pipe (diameter = 0.0508 m) and a pivot point (for tilting the test section to different inclination angles, Fig. 5.3a); ii) air motor with gear reducer (Fig. 5.3b) for pipe rotation; iii) differential pressure (DP) transmitters for continuous measurement of pressure differences between ports; iv) temperature transmitter; v) 53-liter mud tank that is equipped with an agitator; vi) Moyno pump with variable frequency drive (VFD) for mud circulation; vii) Coriolis flow meter for flow rate and density measurements; viii) a heating system that is made

up of water tank, heater, pump with VFD, and copper coiled-tubing; and ix) data acquisition boards and a computer for monitoring and recording test parameters and measurements.

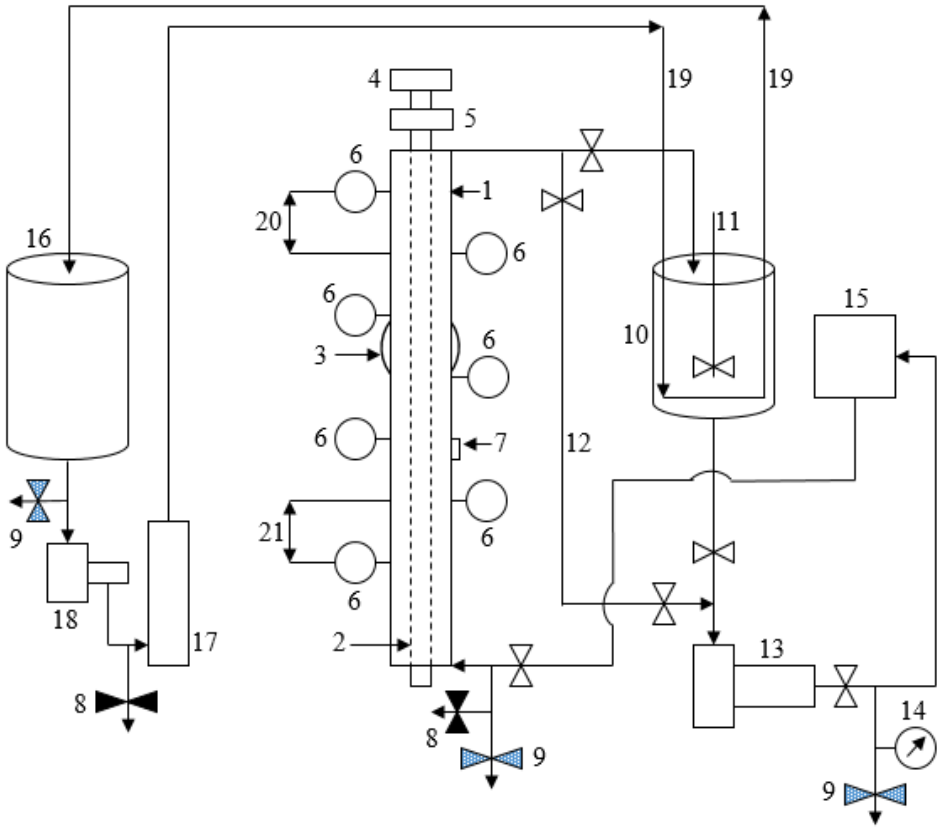

1) Test Section; 2) Inner Rotating Pipe; 3) Pivot Point; 4) Air Motor; 5) Gear Reducer; 6) DP Transmitter; 7) Temperature Sensor; 8) Relief Valve; 9) Drain Valve; 10) Mud Tank; 11) Agitator; 12) Bypass Line; 13) Moyno Pump; 14) Pressure Gauge; 15) Coriolis Flow Meter; 16) Water Tank; 17) Heater; 18) Pump; 19) Copper Coiled-Tubing; 20) Top Section; 21) Bottom Section

Fig. 5.1: Flow loop schematic

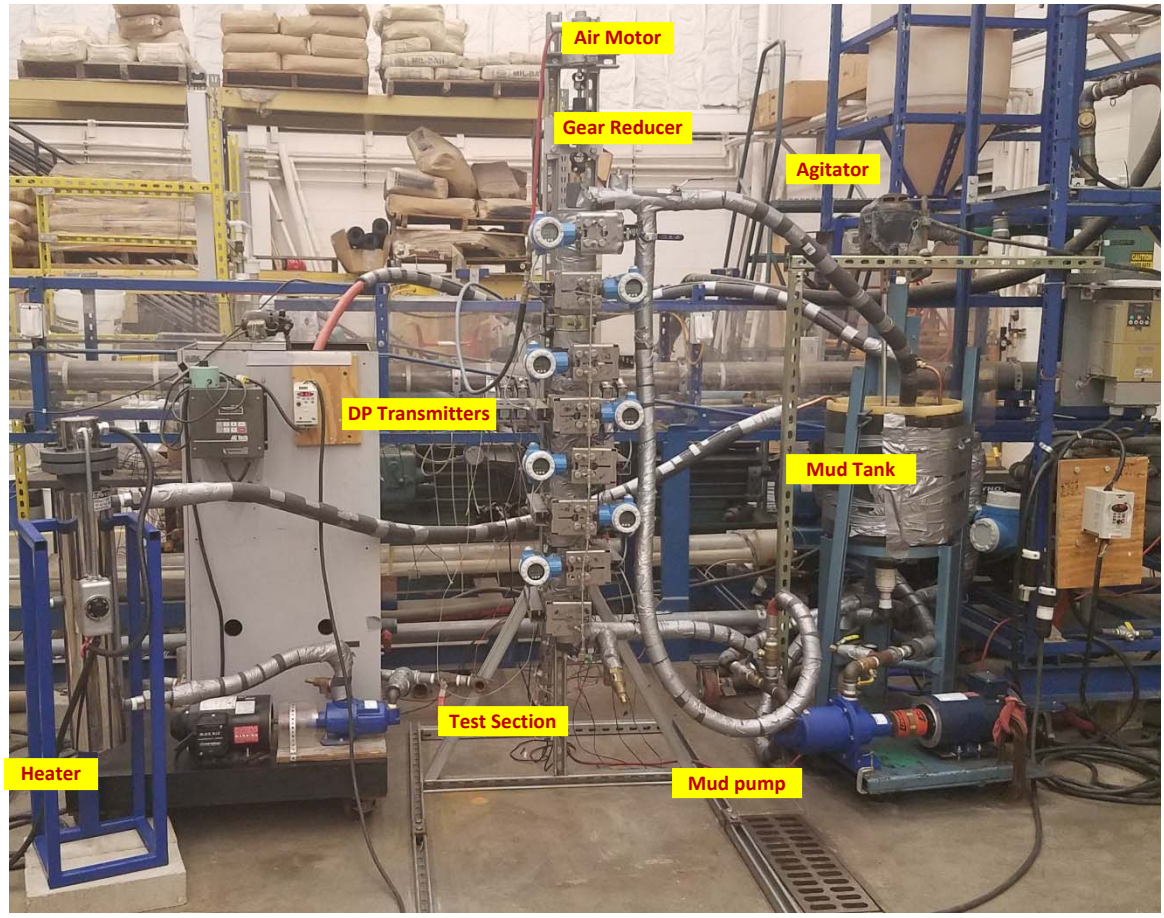

Fig. 5.2: Photo of flow loop setup

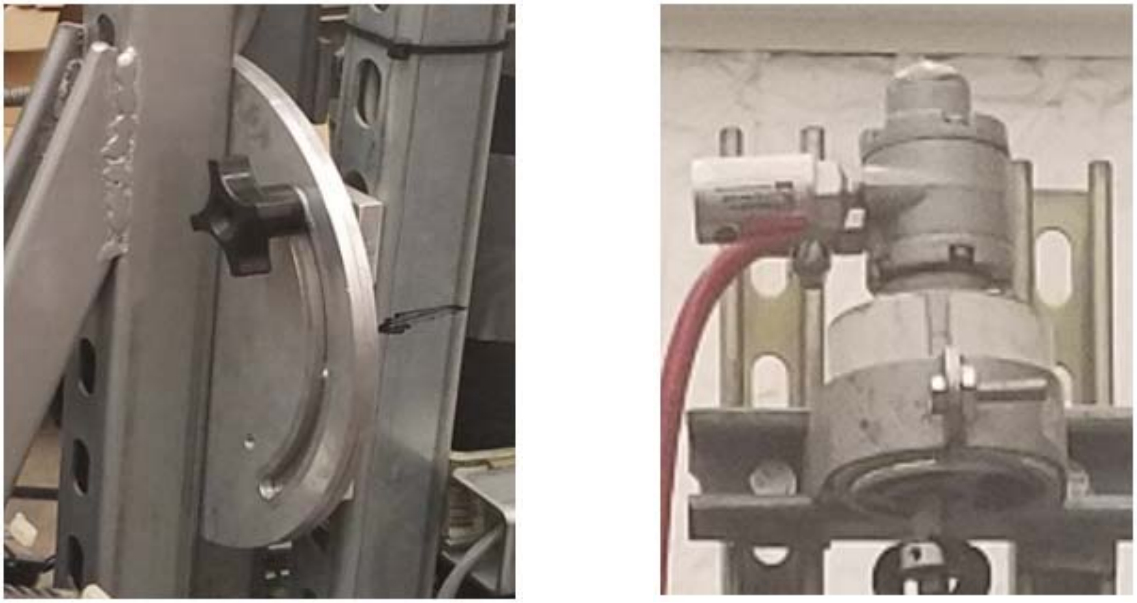

(a) **(b)**

Fig. 5.3: Flow loop parts: a) pivot point; and b) air motor

5.5. Preparation of Test Sample

Numerous batches of weighted OBM samples were prepared to have the required amount of mud (38-liter) for testing. The preparation procedures for weighted OBM were described in Section 4.4; however, only the regular barite was used. The test sample had a mud weight of 1413.8 kg/m^3.

5.6. Test Procedures

The differential pressure transmitters were calibrated with water before the test sample was introduced into the flow loop system. Also, the temperature sensor was calibrated with known temperature values. Water was pumped out of the system and the weighted OBM was poured into the mud tank and circulated into the flow loop system. To start a test, the test section was tilted to the desired inclination angle and secured in position, and the air motor was not turned on. Then, the weighted OBM was mixed in the mud tank and at the same time circulated by the Moyno pump at a high flow rate to ensure homogeneous mixing. For the circulation, the Moyno pump sucked the weighted OBM from the mud tank and passed it through the Coriolis flow meter and the test section and back to the mud tank. While mud circulation was ongoing, the heating system was added by using the pump to circulate water from the water tank to the heater, and then, a copper coiled-tubing transports the water (that exits the heater) to the mud tank and back to the water tank. As the circulated water was heated, the temperature of the circulated mud increased. The circulation processes were monitored on the computer. Once the required test temperature of 49°C was attained, the heater and the pump were switched off. Thereafter, the Moyno pump was switched off and the valve at the inlet (bottom) of the test section was closed. However, the valve at the outlet (top) of the test section was left in its opened position so that the return line could be open to the atmosphere. If the test was at 0° inclination, the bypass line was

left in its closed position. Else, the bypass line was opened (by opening its valves) so that the mud from the inclined return line could drain into it. Additionally, if the test was desired under a dynamic condition, the air motor was turned on to achieve the needed pipe rotational speed. Else, the test section was ready for taking measurements under a static condition. Then, differential pressure readings were recorded on the computer for 1 hour.

5.7. Results and Discussion

Barite sag in a weighted OBM was investigated in a flow loop at 49°C, and varying pipe rotational speeds (0 and 46 rpm) and inclination angles (0, 25, and 50°). Normalized mud densities were calculated from differential pressure readings, and the results from the top and bottom sections of the mud column are presented and discussed.

5.7.1. Repeatability Tests

In order to assess the accuracy and reproducibility of measurements, repeated tests were performed. Results are presented in Figs. 5.4 through 5.6, and they demonstrate the accuracy (±13%) and reproducibility of the experimental measurements. The sources of the discrepancies are minor differences in test parameters, operating procedures, and instrument measuring errors. In addition, end effects have some contribution in the influence that the experiments experience. Efforts have been made to minimize the end effects by closing the inlet valve of the test section.

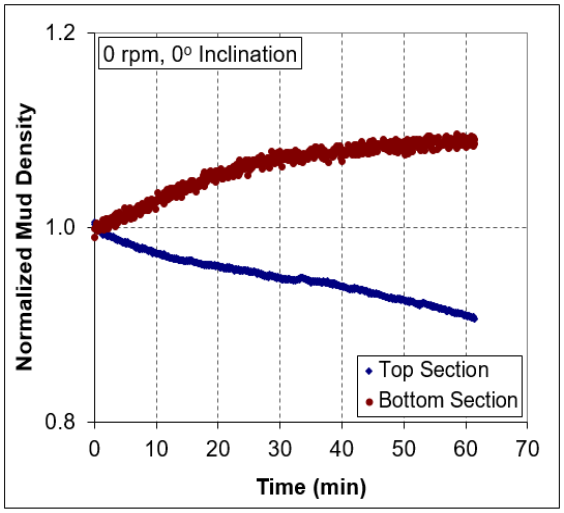

(a)

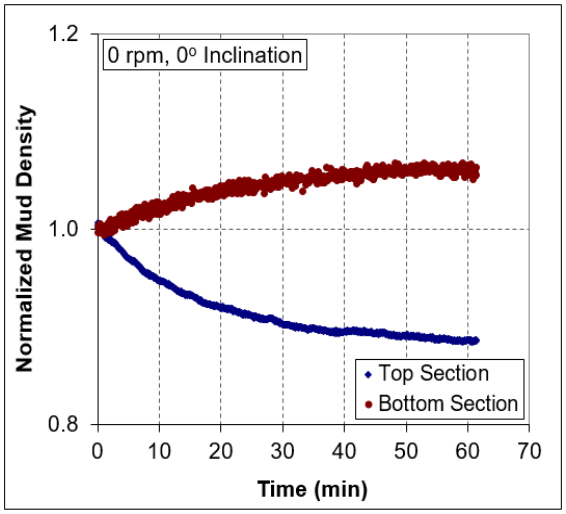

(b)

Fig. 5.4: Repeatability test for 0 rpm at 0° inclination: a) test 1; and b) test 2

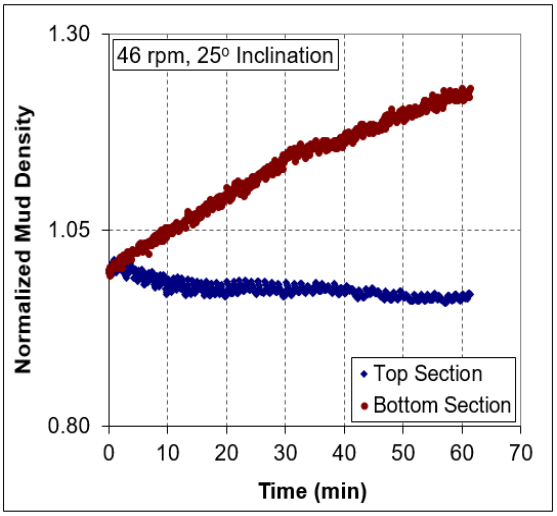

(a)

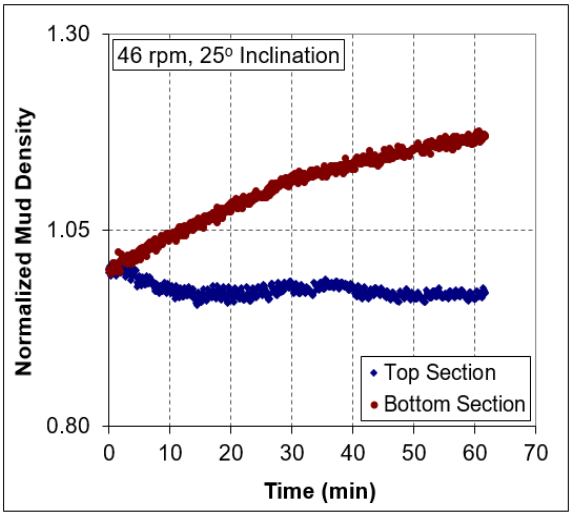

(b)

Fig. 5.5: Repeatability test for 46 rpm at 25° inclination: a) test 1; and b) test 2

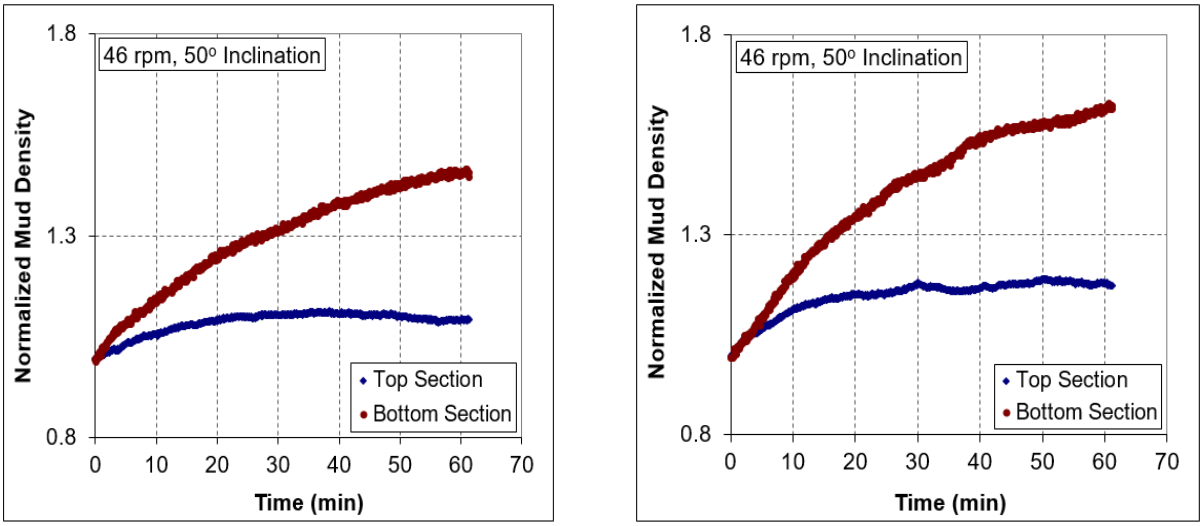

Fig. 5.6: Repeatability test for 46 rpm at 50° inclination: a) test 1; and b) test 2

5.7.2. Effect of Pipe Rotation on Barite Sag

The normalized mud density plots displayed in Figs. 5.7 through 5.9 illustrate the effect of pipe rotation on barite sag. The top and bottom sections of the mud column are depicted in Fig. 5.1. In a vertical configuration (Fig. 5.7), pipe rotation increased barite sag in the bottom section. This can be attributed to the shear thinning caused by pipe rotation. Also, barite sag was indicated earlier under dynamic condition (46 rpm) than under static condition (0 rpm). In inclined configuration (Figs. 5.8 and 5.9), this trend changed in the bottom section. Barite sag was observed earlier under static condition (0 rpm) than under dynamic condition (46 rpm). The observation was that barite sag quickly occurred under static condition (0 rpm) whereas it was gradually detected under dynamic condition (46 rpm) as time progressed. In addition to shear thinning, the inclination angle played a role in determining barite sag (Figs. 5.8 and 5.9).

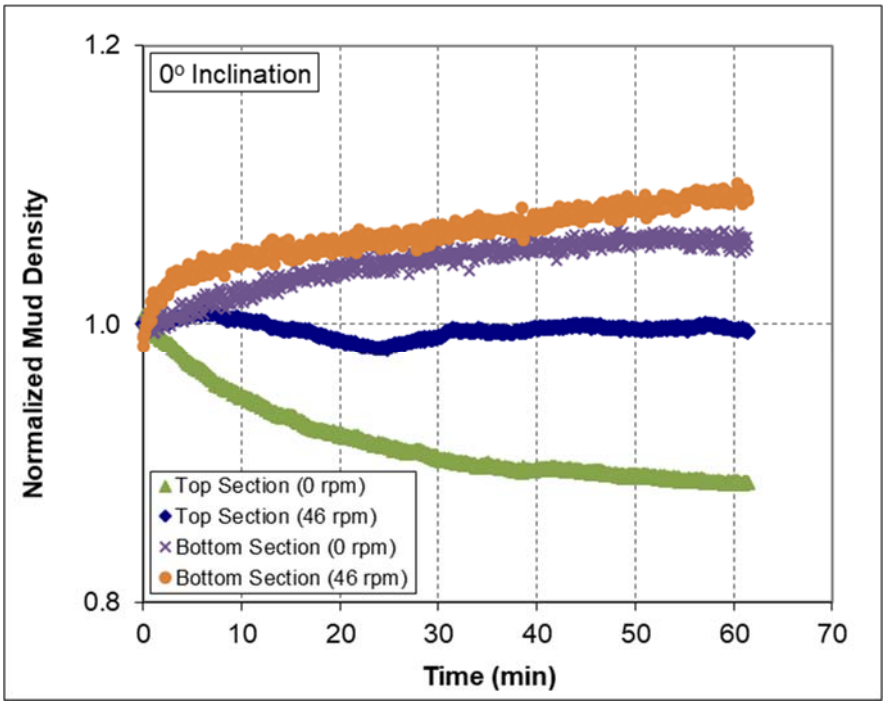

Fig. 5.7: Effect of pipe rotation on barite sag at 0° inclination

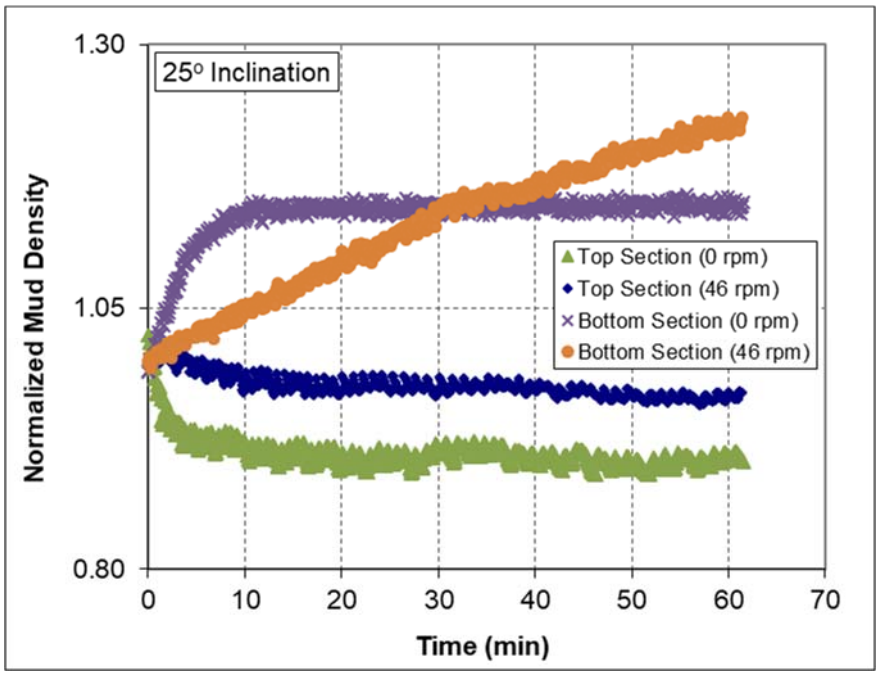

Fig. 5.8: Effect of pipe rotation on barite sag at 25° inclination

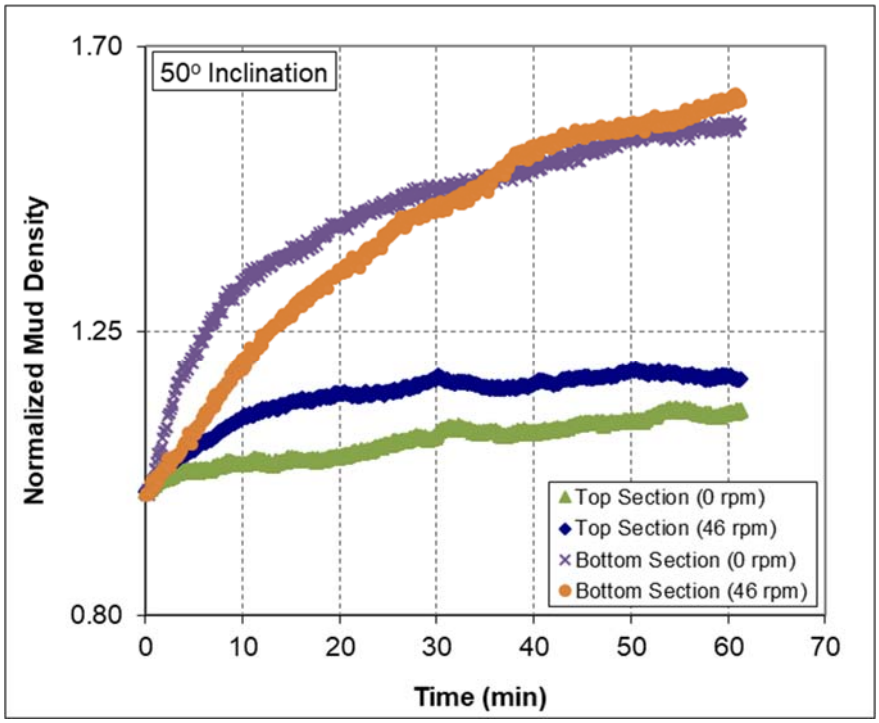

Fig. 5.9: Effect of pipe rotation on barite sag at 50° inclination

Barite deposition in the top section was different from the bottom section. In general, higher density profiles were observed in the top section under dynamic condition (46 rpm) than under static condition (0 rpm). These observed profiles suggest that higher amounts of barite particles entered the top section under the dynamic condition (pipe rotation) than under the static one. Therefore, in comparison to the static condition (0 rpm), more barite particles were available to replace the ones that settled out of the top section when pipe rotation was involved. Also, it is important to note that the densities of both top and bottom sections increased with time at a high inclination angle (50°). This indicates that a significant amount of barite was lost in the uppermost part of the test section, which is located above the top section.

5.7.3. Effect of Inclination Angle on Barite Sag

The normalized mud density plots presented in Figs. 5.10 and 5.11 display the effect of inclination angle on barite settling. As the inclination angle increased, barite sag increased in the bottom section. The observed increase in the bottom section can be attributed to the Boycott effect that exacerbated particle settling when the test section was inclined. In addition to the Boycott effect, pipe rotation played a role in the results presented in Figs. 5.11b and 5.11c. The Boycott effect had no influence on the results shown in Figs. 5.10a and 5.11a because the test section was not inclined. The mechanisms involved in Boycott settling were described in Section 2.3.2. The results of the top section displayed in Figs. 5.10c and 5.11c illustrate barite particle accumulation. These results suggest that the magnitude of barite sag induced at 50° inclination caused the entrance of large amounts of barite particles into the top section from the uppermost part (located above the top section) of the test section. Therefore, more than enough barite particles were available to replace the ones that settled out of the top section; hence, particle accumulation occurred.

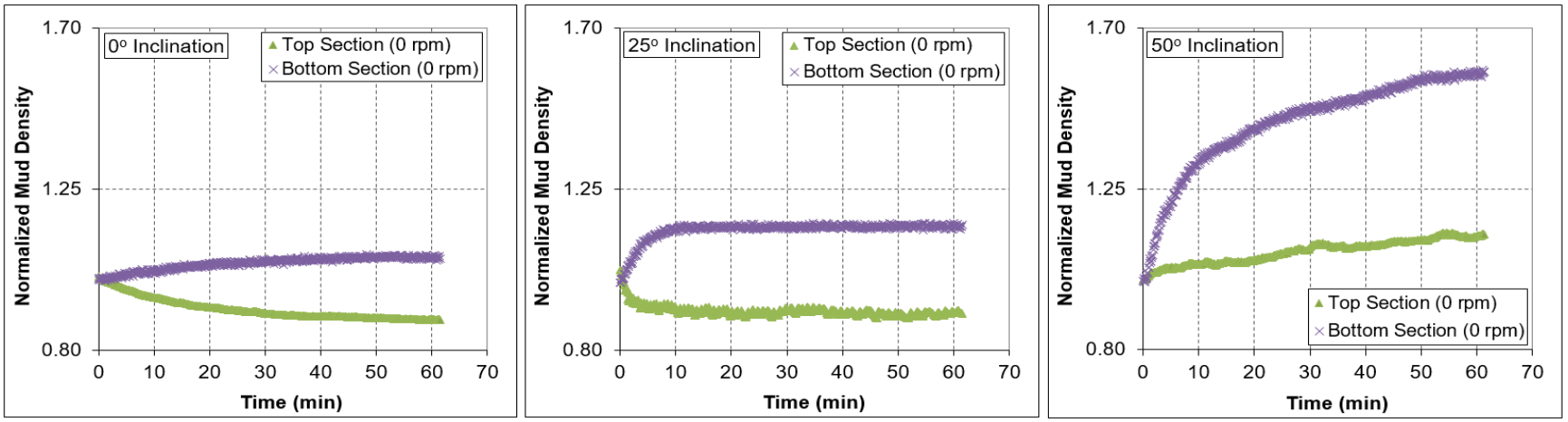

(a) **(b)** **(c)**

Fig. 5.10: Effect of inclination angle on barite sag at 0 rpm: a) at 0° inclination; b) at 25° inclination; and c) at 50° inclination

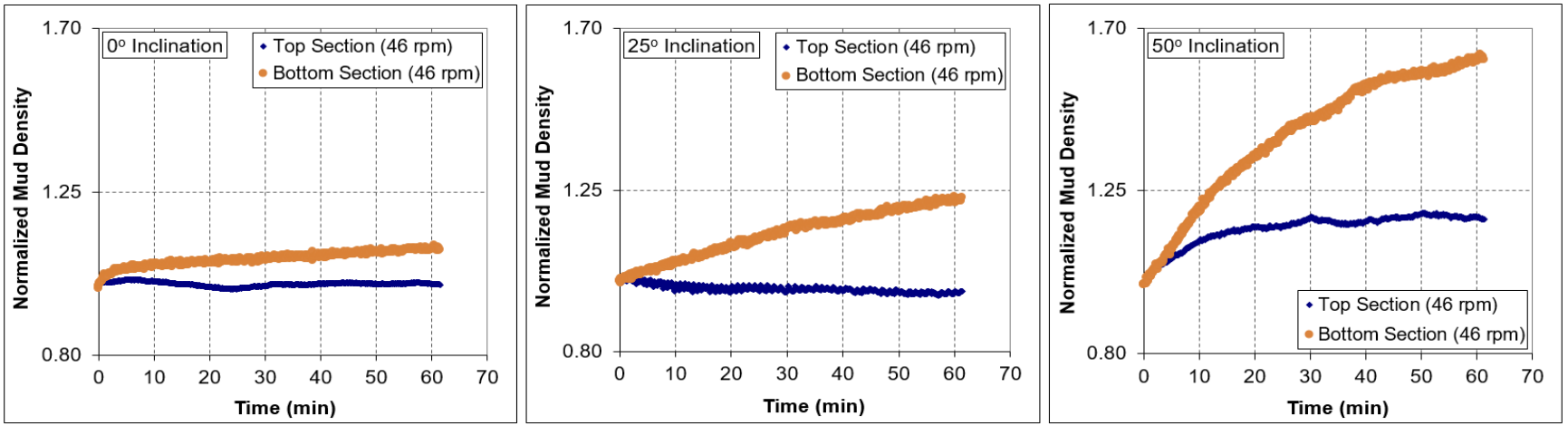

(a) **(b)** **(c)**

Fig. 5.11: Effect of inclination angle on barite sag at 46 rpm: a) at 0° inclination; b) at 25° inclination; and c) at 50° inclination

Chapter 6: Mathematical Modeling of Barite Sag

6.1. Overview

A special case of the sedimentation-consolidation model developed for a continuous thickener is solved numerically using the fully implicit finite difference method. This special case represents a settling column. The numerical solution is implemented using MATLAB, and simulation results are verified by the results of a previous work presented in the literature. Barite particle parameters, shear rate, and OBM rheological parameters are incorporated into the model through settling velocity calculations in order to model barite sag. This adaptation enabled the model to give reasonable predictions of experimental results obtained from the VSST method. A parametric study is performed using the developed barite sag simulator, and results are discussed.

6.2. Model Assumptions

The general assumptions inherited from the original model (Bürger and Concha, 1998; Bürger et al., 2000a) include the following:

- Solid particles are very small in relation to the settling vessel.
- Densities of solid particles are the same.
- The solid and liquid components of the suspension are incompressible, and there is no mass transfer between them.
- Solid particles do not flocculate or aggregate during settling.
- The solids only perform a one-dimensional compression motion.
- The solid and liquid parts demonstrate an elastic behavior.
- Gravity is the only external body force.

Additional assumptions include the following:

- The fluid is non-Newtonian, which is described by the Herschel-Bulkley model.
- The process is isothermal.
- The settling is happening in a sheared fluid.

6.3. Sedimentation-Consolidation Model

The separation of solid-liquid suspension under the influence of gravity is applied in many industries. A thickener is a cylindrical vessel used for solid-liquid separation (Bürger and Concha, 1998). For a thickener, there is a continuous inflow of feeding suspension at the top and a continuous discharge of sediment at the bottom (Fig. 6.1).

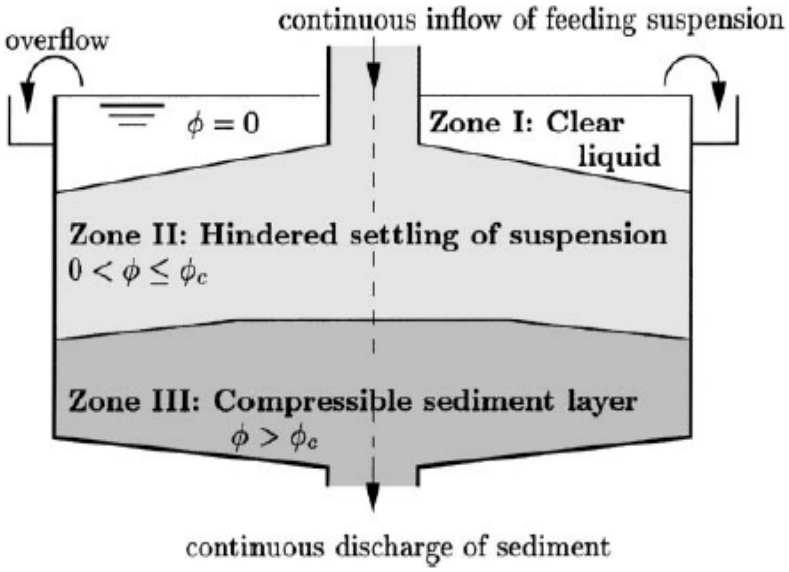

Fig. 6.1: Schematic of a continuous thickener (Bürger, 2000)

Bürger (2000) and Bürger et al. (2000a) used the principles of continuum mechanics to develop a transient phenomenological model for batch and continuous sedimentation of flocculated suspensions. Continuity equations (or local mass balances) and linear momentum

balances were written for the solid and liquid parts. The one-dimensional case of the derived model for estimating volumetric solids concentration is expressed below (Bürger, 2000):

$$\frac{\partial \phi}{\partial t} + \frac{\partial}{\partial z}[q(t)\phi + f_{bk}(\phi)] = \frac{\partial}{\partial z}\left[a(\phi)\frac{\partial \phi}{\partial z}\right] \tag{6.1}$$

where:

$$f_{bk}(\phi) = -\frac{\Delta\rho g \phi^2 (1-\phi)^2}{\alpha(\phi)} \tag{6.2}$$

$$a(\phi) = -\frac{f_{bk}(\phi)\sigma_e'(\phi)}{\Delta\rho g \phi} \tag{6.3}$$

$$\sigma_e'(\phi) = \frac{d\sigma_e}{d\phi}\begin{cases} = 0 \text{ for } \phi \le \phi_c \\ > 0 \text{ for } \phi > \phi_c \end{cases} \tag{6.4}$$

The initial condition is:

$$\phi(z, 0) = \phi_0(z), \quad z \in (0, L) \tag{6.5}$$

The boundary conditions are:

$$f_{bk}(\phi)|_{z=0} - a(\phi)\frac{\partial \phi}{\partial z}\Big|_{z=0} = 0 \tag{6.6}$$

$$\phi(L, t) = \phi_L(t), \quad t \in (0, T_m) \tag{6.7}$$

where ϕ is volumetric solids concentration; ϕ_c is critical concentration; q(t) is volume average velocity; $f_{bk}(\phi)$ is Kynch batch flux density function; $a(\phi)$ is diffusion coefficient; $\sigma_e(\phi)$ is effective solid stress function; $\alpha(\phi)$ is resistance coefficient; $\Delta\rho$ is solid-fluid mass density difference; g is acceleration due to gravity; t is time; T_m is maximum time; z is height; L is feeding level height.

A special case of this model is the settling column, and this is achieved when the bottom of the thickener is closed ($q \equiv 0$) and there is no feeding ($\phi_L = 0$) at the top. For practical applications, several $f_{bk}(\phi)$ and $\sigma_e(\phi)$ types proposed by different studies are used in numerical

solutions. In the work of Bürger et al. (1999), the $f_{bk}(\phi)$ type proposed by Richardson and Zaki (1954) was presented as:

$$f_{bk}(\phi) = v_{\infty}\phi(1-\phi)^{C+1} \tag{6.8}$$

Also, the $\sigma_e(\phi)$ determined by Becker (1982) was expressed as:

$$\sigma_e(\phi) = \begin{cases} 0 & \text{for } \phi \leq \phi_c \\ \alpha e^{\beta\phi} & \text{for } \phi > \phi_c \end{cases} \tag{6.9}$$

where v_{∞} is settling velocity of a single floc in an unbounded medium; C is exponent in the flux density function; α and β are parameters in the effective solid stress function. According to Bürger et al. (1999), the parameters in Eqs. 6.8 and 6.9 were derived by Becker (1982) based on experimental work conducted with Chilean copper ore tailings. The values of these parameters are: v_{∞} = -6.05 × 10^{-4} m/s; C = 11.59; ϕ_c = 0.23; α = 5.35 N/m^2; β = 17.9.

For the numerical solution of Bürger et al. (2000b), Eq. 6.1 and its initial and boundary conditions stated in Eqs. 6.5 – 6.7 are separated into three equations (each of the first two had an initial condition while the third had boundary conditions) using the operator splitting by finite differencing. Then, the three equations are solved by applying the conservative central method, a first order upwind method, and a variant of Nessyahu and Tadmor's method, respectively. Eventually, the numerical solution is obtained through a defined compact equation that combined the solutions of the three equations. For the simulation of batch settling of suspension presented in the work of Bürger et al. (2000b), a settling column that is closed at the bottom and without feed is considered. The $f_{bk}(\phi)$ and $\sigma_e(\phi)$ in Eqs. 6.8 and 6.9, and their values stated above are used. The other values used are: L = 6 m; initial homogeneous concentration, $\phi_0(z)$ = 0.123; $\Delta\rho = \rho_s - \rho_f$ = 1500 kg/m^3; g = 9.81 m/s^2; number of grid blocks, N = 300; number of time steps = 3000. The concentration profiles of their simulation, for different T_m values, are displayed in Fig. 6.2.

6.4. Fully Implicit Finite Difference Numerical Solution

In this work, the numerical solution of Eq. 6.1 was obtained by applying the fully implicit finite difference method. Equations 6.5 – 6.7 are implemented in this solution. The $f_{bk}(\phi)$ and $\sigma_e(\phi)$ in Eqs. 6.8 and 6.9, and the other values presented above are used in order to replicate the simulation results of the batch settling problem presented in the work of Bürger et al. (2000b). The full details of the numerical technique are provided in Appendix B. However, the steps followed are presented below.

- The boundary condition (Eq. 6.6) at the bottom interface (z = 0) is discretized, and the Newton-Raphson method is used to obtain the volumetric solids concentration in the fictitious block below the bottom block.
- Equation 6.1 is discretized, and the expression for the residual function is developed. With this expression, the residual functions for all the blocks are obtained.
- The boundary condition (Eq. 6.7) at the top interface (z = L) is implemented, and volumetric solids concentration in the fictitious block above the top block is evaluated.
- The elements of the Jacobian matrix from the bottom block, top block, and interior blocks are computed by differentiating the residual functions.

After completing the discretization and computational processes, the equations are programmed in MATLAB (Appendix C) and the input parameters stated at the beginning of this section are used. Figure 6.2 reveals that the results of this work give reasonable predictions of the simulation results of the batch settling problem presented in the work of Bürger et al. (2000b).

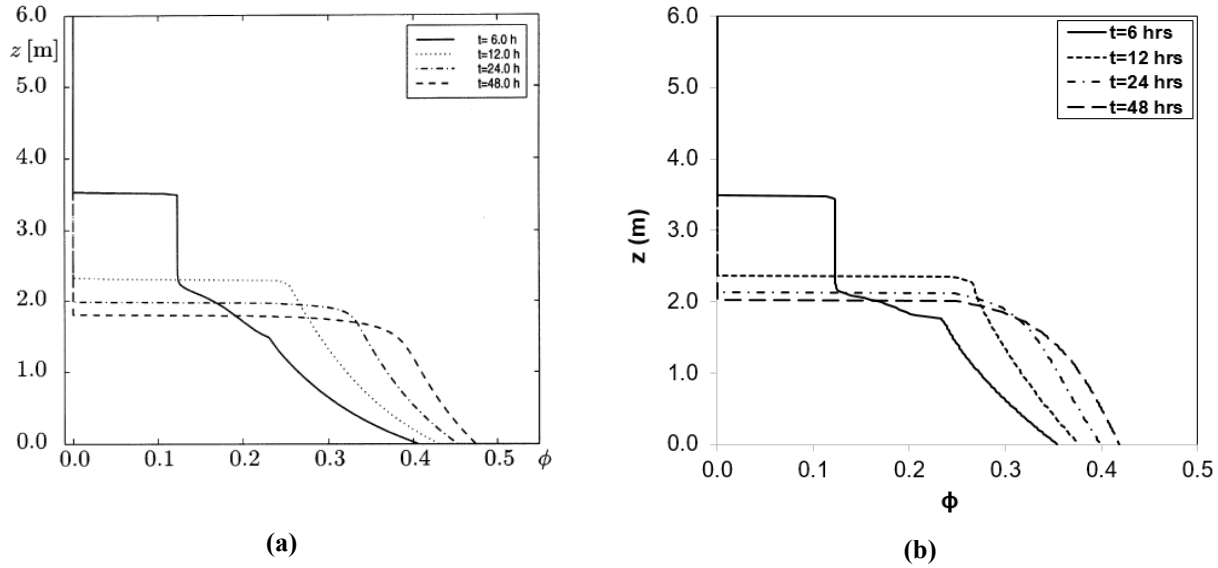

Fig. 6.2: Predicted concentration profiles for batch settling of suspension from: a) Bürger et al. (2000b); and b) this current work

6.5. Settling Velocity Calculation

The terminal settling velocity of a particle settling in a static fluid under steady state condition is expressed as (Bourgoyne et al., 1986):

$$v_\infty = \sqrt{\frac{4}{3}\frac{d_s}{f}\left(\frac{\rho_s - \rho_f}{\rho_f}\right)g} \tag{6.10}$$

where d_s is particle diameter; ρ_f is fluid density; ρ_s is particle density; f is the drag coefficient.

Under laminar flow condition, the drag coefficient is calculated as:

$$f = \frac{24}{N_{Re}} \tag{6.11}$$

For turbulent flow, the drag coefficient can be calculated as (Frank, 2006):

$$f = \frac{24}{N_{Re}} + \frac{6}{1+N_{Re}^{0.5}} + 0.4 \tag{6.12}$$

where N_{Re} is the Reynolds number, which is expressed as:

$$N_{Re} = \frac{\rho_f v_\infty d_s}{\mu_a} \tag{6.13}$$

where μ_a is the apparent viscosity.

The apparent viscosity of Herschel-Bulkley fluid is expressed as a function of shear rate.

$$\mu_a = \frac{\tau_y}{\dot{\gamma}_c} + K\dot{\gamma}_c^{n-1} \tag{6.14}$$

where τ_y is yield stress; K is consistency index; n is fluid behavior index; $\dot{\gamma}_c$ is the combined shear rate which represents the effects of rotational and axial flows in the annulus.

$$\dot{\gamma}_c = \sqrt{\dot{\gamma}_a^2 + \dot{\gamma}_r^2} \tag{6.15}$$

where $\dot{\gamma}_a$ is axial shear rate due to particle settling; $\dot{\gamma}_r$ is tangential shear rate due to rotation (primary flow due to drill string rotation). The axial shear rate due to particle settling is determined as:

$$\dot{\gamma}_a = \frac{v_\infty}{d_s} \tag{6.16}$$

The tangential shear rate due to rotation is expressed as (Bourgoyne et al., 1986):

$$\dot{\gamma}_r = r\frac{d\omega}{dr} \tag{6.17}$$

where r is any radius between the bob radius and the rotor radius; ω is angular velocity.

The final expression, from the derivations of Bourgoyne et al. (1986), is:

$$\dot{\gamma}_r = \frac{5.066N_{sp}}{r^2} \tag{6.18}$$

where N_{sp} is rotor speed, rpm; r is used in cm.

6.6. Model Predictions of VSST Results

Having reproduced the simulation results of the batch settling problem presented in the work of Bürger et al. (2000b), the fully implicit finite difference numerical solution is now adapted to predict the barite sag measurements presented in Section 4.6.3. The VSST results and rotational speeds are converted to ϕ and $\dot{\gamma}_r$, respectively. The values of C = 33.5; ϕ_c = 0.25; α = 2 N/m^2; β = 7.28 are used. The input values from Chapter 4 are: L = 0.09 m; T_m = 30 mins; $\phi_0(z)$ = 0.164; ρ_s = 3767.1 kg/m^3; ρ_f = 953.7 kg/m^3; τ_y = 2.479 Pa; K = 0.6 Pas^n; n = 0.659. The number of

grid blocks used to obtain a numerical solution is 90, the number of time steps used during the simulation is 3600, and g = 9.81 m/s^2. In this case, ρ_f is the density of the unweighted OBM, and its rheological parameters at 49°C are used as simulation input parameters. Figures 6.3 and 6.4 compare the predictions of the model with VSST measurements (barite concentration at the collection well of the Sag Shoe after 30 minutes). The results demonstrate reasonable agreement between model predictions and experimental (VSST) measurements.

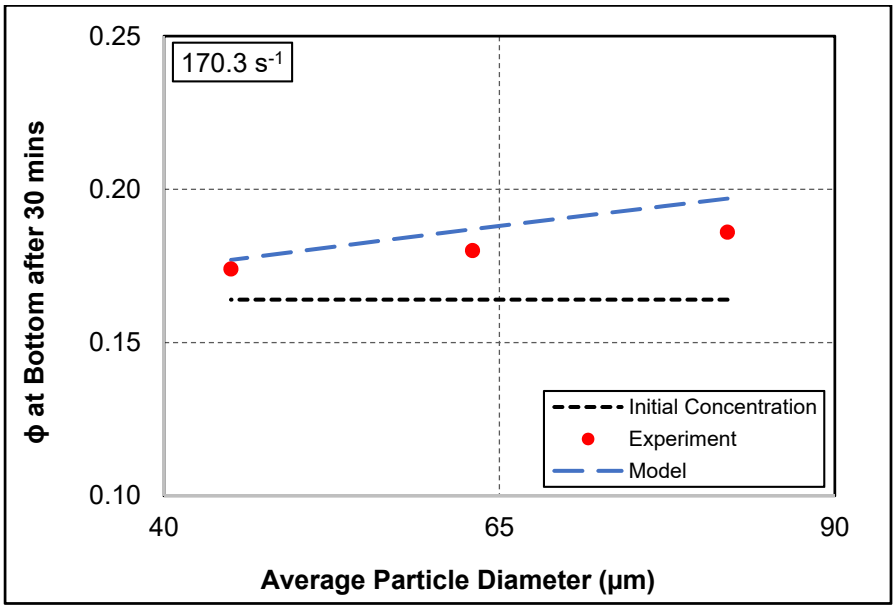

Fig. 6.3: Comparison of model predictions with VSST data for barite types with different D50 values

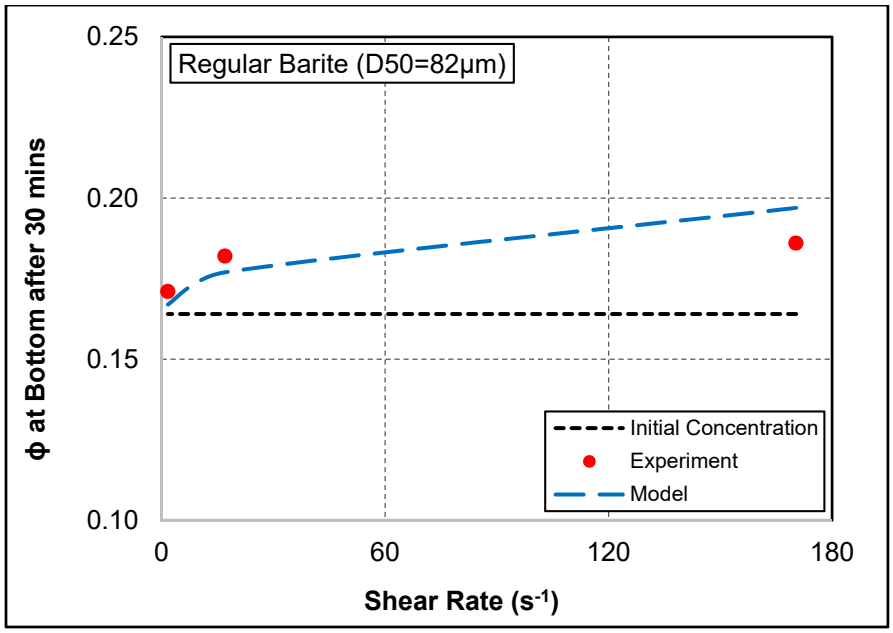

Fig. 6.4: Comparison of model predictions with VSST data for regular barite at different shear rates

6.7. Parametric Studies and Discussion

With the same input parameters used for the prediction of VSST results, a parametric study is performed with the developed barite sag simulator. Figures 6.5 through 6.8 illustrate the effects of particle size and OBM rheological parameters on barite sag. The similar trends observed with shear rate can be attributed to shear thinning. Figure 6.5 shows that barite sag will decrease as particle size reduces. This is mainly because the specific surface area of the particles increases with reduction of particle size. This leads to a disproportionate reduction of gravitational force in relation to hydrodynamic drag which is a function of the surface area of the particles. Besides this, barite sag is influenced by the rheological properties of the mud. It decreases as the rheological parameters (τ_y, K, n) increase (Figs. 6.6 through 6.8), however, the effect of yield stress will reduce at high shear rates because its presence will be concealed once the mud resistance to the onset of flow is overpowered $\left(\frac{\tau_y}{\dot{\gamma}_c} \rightarrow 0\right)$. At low shear rates, the effects of K and n become negligible because the yield stress term $\left(\frac{\tau_y}{\dot{\gamma}_c}\right)$ in the apparent viscosity function (Eq.

6.14) dominates the other term, which involves consistency index and fluid behavior index ($K\dot{\gamma}_c^{n-1}$). At high shear rates, the consistency index directly affects the apparent viscosity of the mud. Figure 6.7 suggests that initial increments in the apparent viscosity of the mud can rapidly reduce barite sag. The fluid behavior index describes the degree of shear thinning, which influences barite sag. Shear thinning and barite sag decrease simultaneously as fluid behavior index increases.

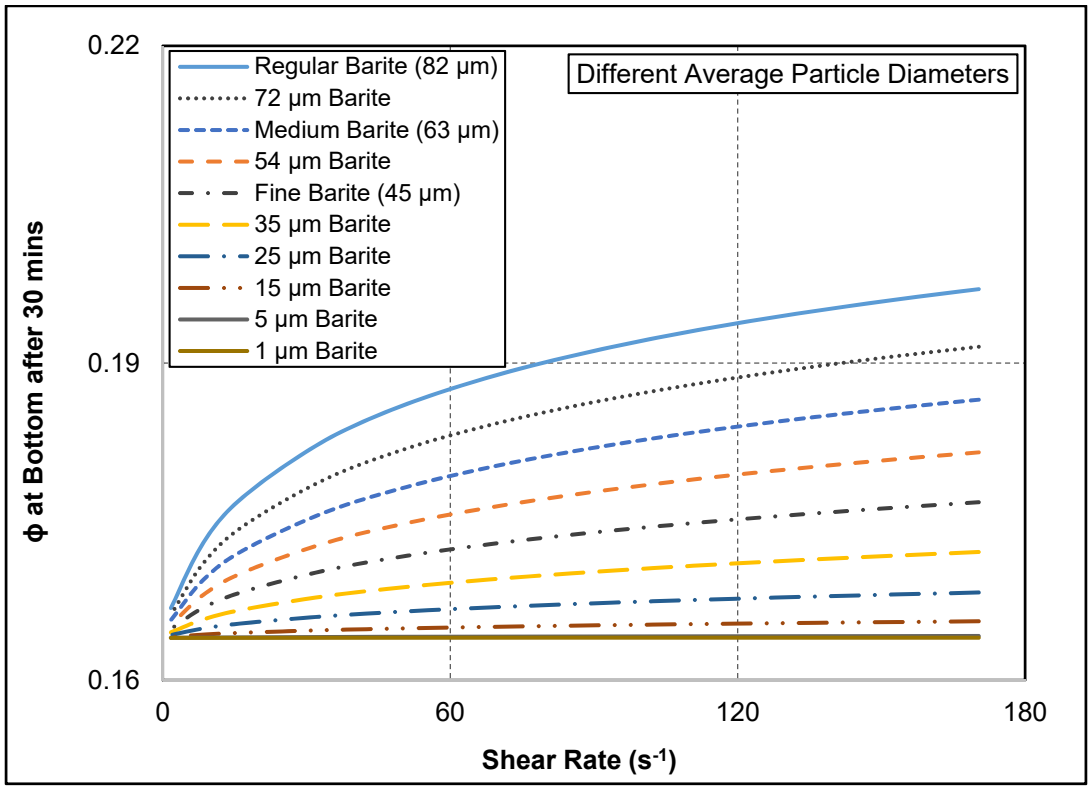

Fig. 6.5: Parametric studies on barite sag showing the effect of particle size

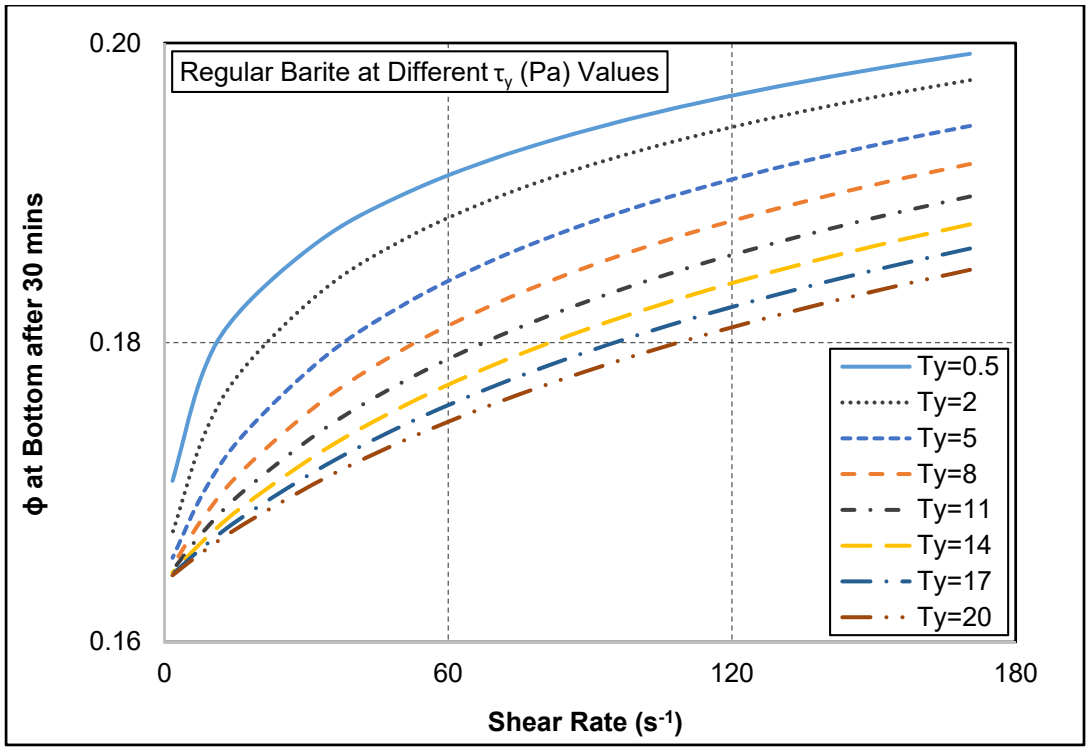

Fig. 6.6: Parametric studies on barite sag showing the effect of yield stress

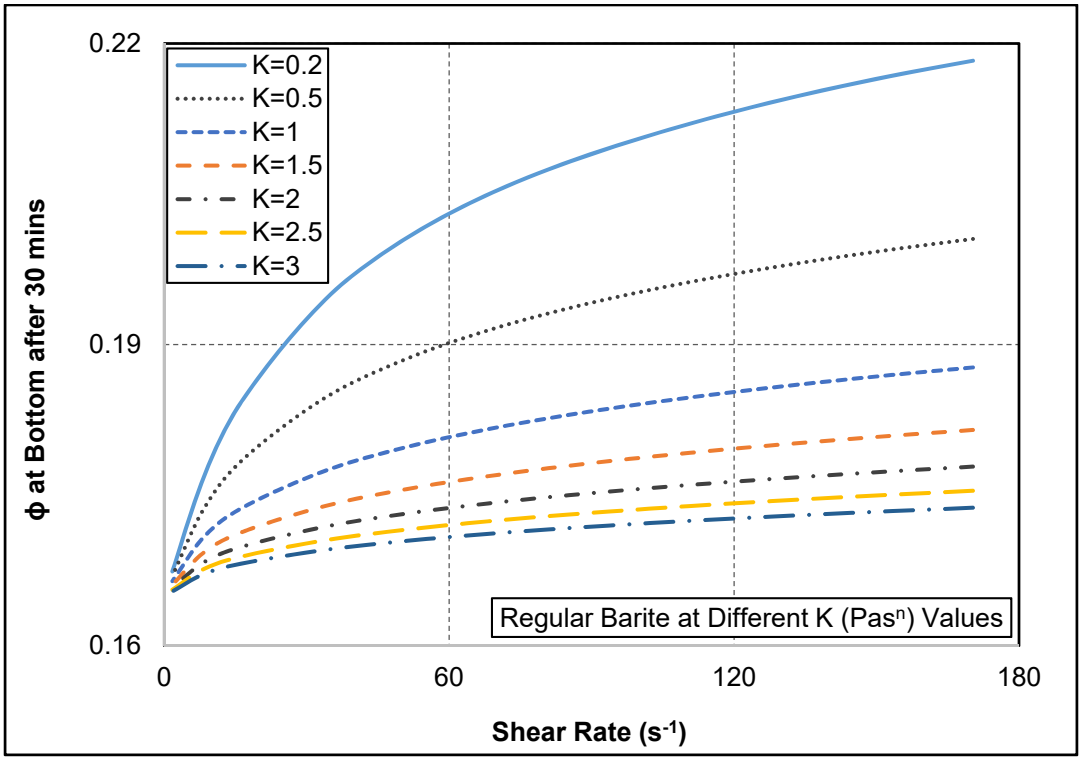

Fig. 6.7: Parametric studies on barite sag showing the effect of consistency index

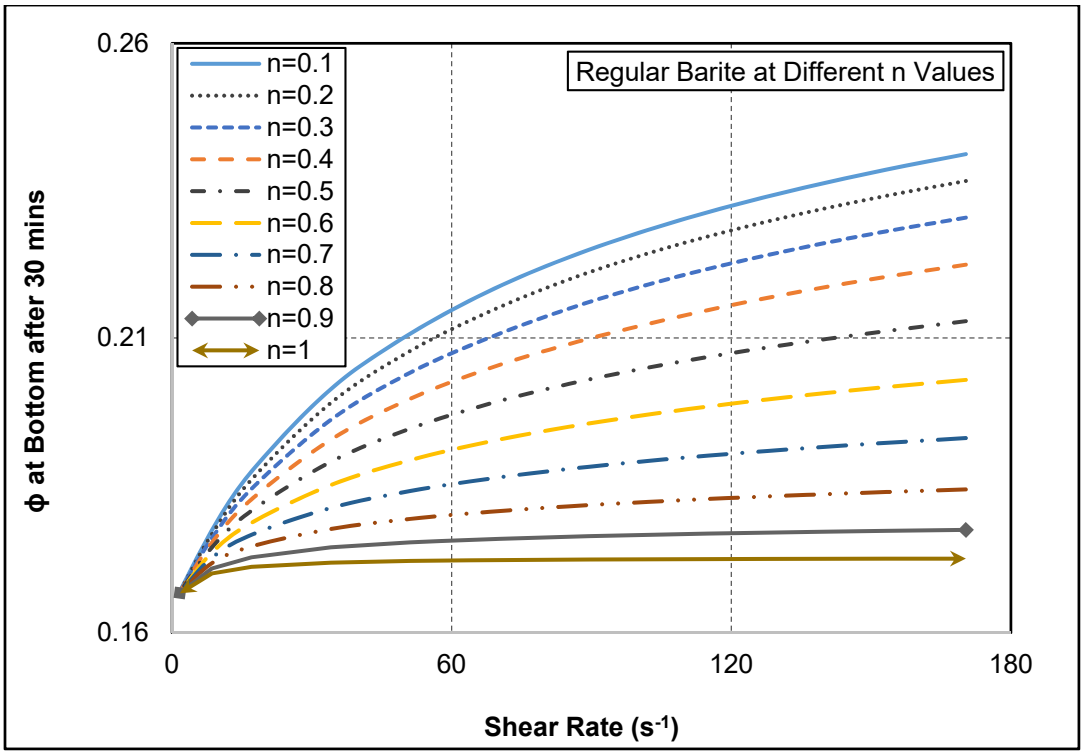

Fig. 6.8: Parametric studies on barite sag showing the effect of fluid behavior index

Chapter 7: Conclusions and Recommendations

7.1. Conclusions

A comprehensive study has been conducted to investigate barite sag. Both experimental and theoretical approaches have been considered in the investigation. The following conclusions can be drawn from this investigation.

- The major factors affecting barite sag are: particle size, inclination angle, mud viscous properties, and rotational speed.
- The normalized rheological parameters (normalized yield stress and normalized consistency index) of OBMs showed higher reduction with temperature (up to 66°C) than that of WBMs, and this explains the vulnerability of OBM to barite sag issues.
- The VSST results indicated that barite sag increased as average particle diameter and rotational speed increased up to 82 μm and 100 rpm, respectively. The increase in barite sag with rotational speed increment is attributed to shear thinning.
- The flow loop results (normalized mud densities) revealed that barite sag increased in the bottom section of the mud column as pipe rotational speed increased from 0 to 46 rpm. However, as inclination angle increased up to 50°, sagging initially slowed down in the bottom section due to pipe rotation and later increased as time progressed. The increase in barite sag with pipe rotation and inclination angle is attributed to shear thinning and the Boycott effect, respectively.
- The top section of the mud column showed less sagging when pipe rotation is involved. This is caused by the higher amounts of barite particles that entered this section, hence, more barite particles were available to replace the ones that settled out the section. But, at

inclination angle of 50°, barite particle accumulation occurred in the top section due to the high magnitude of barite sag.

- The barite sag model developed in this study reasonably predicts the VSST measurements. The model indicates that barite sag increases with particle size and shear rate. The sagging tendency decreases as viscous properties of the mud increases.
- This research facilitates the understanding of barite sag, and it will help in minimizing the drilling problems (such as lost circulation, wellbore instability, and stuck pipe) associated with it.

7.2. Recommendations

In the future, some additional research can be done. Hence, it is recommended to:

- Conduct experimental studies on the rheology of OBM and its continuous phase up to a temperature beyond 87°C. This will extend the temperature range applicability of the rheological models.
- Investigate barite sag in flow loop at higher rotational speeds (greater than 46 rpm).
- Study the effect of annular velocity on barite sag in flow loop.
- Model the Boycott effect on barite sag when pipe inclination is involved.

Nomenclature

d_s	Particle diameter
m_s	Particle mass
r_s	Particle radius
V_s	Particle volume
a	Empirical constant
b	Empirical constant
c_1	Empirical constant
c_2	Empirical constant
$A_{\tau yo}$	Fluid parameter
$B_{\tau yo}$	Fluid parameter
$C_{\tau yo}$	Fluid parameter
A_{Ko}	Fluid parameter
B_{Ko}	Fluid parameter
A_{no}	Fluid parameter
B_{no}	Fluid parameter
C_{no}	Fluid parameter
$A_{\tau y}$	Fluid parameter
$B_{\tau y}$	Fluid parameter
A_K	Fluid parameter
B_K	Fluid parameter
C_K	Fluid parameter

D_K	Fluid parameter
A_n	Fluid parameter
B_n	Fluid parameter
C_n	Fluid parameter
K	Consistency index of the OBM at temperature T
K_o	Consistency index of the OBM at the reference temperature
n	Fluid behavior index of the OBM at temperature T
n_o	Fluid behavior index of the OBM at the reference temperature
e	Integer
$T_{\tau ys}$	Vertical component of the yield stress force acting on a spherical particle
F_g	Gravity force
F_b	Buoyancy force
F	Net force acting on the particle
g	Acceleration due to gravity
G′	Elastic modulus
k	Correlation constant
k_o	Fluid rheological parameter
k_1	Fluid rheological parameter
Ka	Constant representing inclination angle
Kv	Constant representing annular velocity
Kr	Constant representing rotary speed
Kz	Constant representing well section length
$MW_{initial}$	Initial mud weight

MW_{bottom}	Mud weight at the bottom
MW_{top}	Mud weight at the top
P	Pressure
P_o	Atmospheric pressure
S	Sag index
$S_D(t)$	Dynamic sedimentation index
S_R	Sag register
T	Temperature
T_o	Reference temperature
V*	Complex viscosity
v_∞	Settling velocity of a single particle
w	Fluid velocity in axial direction
WT1	Weight of syringe + cannula + original mud
WT2	Weight of syringe + cannula + mud from collection well
A_1	Notation used in discretization
A_2	Notation used in discretization
A_3	Notation used in discretization
A_4	Notation used in discretization
A_5	Notation used in discretization
$a(\phi)$	Diffusion coefficient
C	Exponent in the flux density function
f	Drag coefficient
N_{Re}	Reynolds number

N_{sp}	Rotor speed
r	Any radius between the bob radius and the rotor radius
N	Number of grid blocks
i	Grid block number
$i \pm \frac{1}{2}$	Interface between grid blocks
m	Time level of computation (where m is old time level; $m+1$ is new time level)
f_i^{m+1}	Residual function
F_i	Matrix of residual functions
J	Jacobian matrix
J^{-1}	Inverse of the Jacobian matrix
$f_{bk}(\phi)$	Kynch batch flux density function
L	Feeding level height
q(t)	Volume average velocity
t	Time
T_m	Maximum time
z	Height

Greek Letters

η_s	Suspension viscosity
η_o	Continuous phase viscosity
η_r	Relative viscosity
ϕ_d	Volume fraction of the dispersed phase

η_{ld}, η_d	Viscosity of dispersed phase
γ	Ratio of radii of particle and cell
$\tilde{\gamma}_e$	Interfacial retardation viscosity
ψ	Equation parameter
β_e	Viscosity parameter
β_2	Viscosity parameter
τ	Shear stress
$\dot{\gamma}$	Shear rate
μ	Viscosity
μ_a	Apparent viscosity
μ_p	Plastic viscosity
μ_{pa}	Plastic viscosity at atmospheric pressure condition
$\beta(T)$	Piezo-viscous coefficient
β_o	Empirical parameter
β_1	Empirical parameter
α_K	Empirical constant
β_K	Empirical constant
ΔMW	Mud weight difference derived from a VSST
ΔMW_b	Difference of the maximum and minimum mud weight obtained during bottoms-up circulation
τ_y	Yield stress of the OBM at temperature T
τ_{yo}	Yield stress of the OBM at the reference temperature

μ_{CP}	Apparent viscosity of the continuous phase at a shear rate of 511 s^{-1}
ρ_s	Particle density
ρ_f	Fluid density
μ_f	Fluid viscosity
$\Delta\rho$	Density difference between particle and base fluid
ϕ	Volumetric solids concentration
ϕ_c	Critical concentration
ϕ_L	Feeding concentration at height L
$\phi_0(z)$	Initial homogeneous concentration
ϕ_0	Volumetric solids concentration in the fictitious block below the bottom block
ϕ_{N+1}	Volumetric solids concentration in the fictitious block above the top block
α	Parameter in the effective solid stress function
β	Parameter in the effective solid stress function
$\alpha(\phi)$	Resistance coefficient
$\sigma_e(\phi)$	Effective solid stress function
Δt	Time step
Δz	Grid size
$\dot{\gamma}_a$	Axial shear rate due to particle settling
$\dot{\gamma}_c$	Combined shear rate
$\dot{\gamma}_r$	Tangential shear rate due to rotation
ω	Angular velocity

Acronyms

DHAST	Dynamic High-Angle Sag Tester
ECD	Equivalent circulating density
HPHT	High pressure and high temperature
LAO	Linear-alpha-olefin
LTMOs	Low-Toxicity Mineral Oils
MW	Mud weight
MWM	Micronized Weight Material
OBM	Oil-based mud
WBM	Water-based mud
OWR	Oil-water ratio
O/W	Oil-in-water
W/O	Water-in-oil
VFD	Variable frequency drive
VST	Viscometer Sag Test
VSST	Viscometer Sag Shoe Test

References

Ackerson, B. J. (1990). Shear induced order and shear processing of model hard sphere suspensions. Journal of Rheology, 34(4), 553–590.

Al-Bagoury, M. (2014). Micronized Ilmenite - A non-damaging non-sagging new weight material for drilling fluids. SPE Bergen One Day Seminar.

Al-Bagoury, M., & Steele, C. D. (2012). A new, alternative weight material for drilling fluids. IADC/SPE Drilling Conference and Exhibition.

Amani, M. (2012). The rheological properties of oil-based mud under high pressure and high temperature conditions. Advances in Petroleum Exploration and Development, 3(2), 21–30.

Becker, R. (1982). Espesamiento continuo, diseno y simulación de espesadores, Engineering Thesis, Department of Metallurgical Engineering, University of Concepción.

Bern, P. A., van Oort, E., Neusstadt, B., Ebeltoft, H., Zurdo, C., Zamora, M., & Slater, K. (1998). Barite sag: Measurement, modelling and management. IADC/SPE Asia Pacific Drilling Technology.

Bern, P. A., Zamora, M., Hemphill, A. T., Marshall, D., Beardmore, D., Omland, T. H., & Morton, E. K. (2010). Field monitoring of weight-material sag. AADE Fluids Conference and Exhibition.

Bern, P. A., Zamora, M., Slater, K. S., & Hearn, P. J. (1996). The influence of drilling variables on barite sag. SPE Annual Technical Conference and Exhibition.

Beydoun, D., Guang, D., Chhabra, R. P., & Raper, J. A. (1998). Particle settling in oil-in-water emulsions. Powder Technology, 97(1), 72–76.

Bourgoyne Jr., A. T., Millheim, K. K., Chenevert, M. E., & Young Jr., F. S. (1986). Applied drilling engineering. SPE Textbook Series, Volume 2. Society of Petroleum Engineers.

Boycott, A. E. (1920). Sedimentation of blood corpuscles. Nature 104 (2621), 532.

Bürger, R. (2000). Phenomenological foundation and mathematical theory of sedimentation–consolidation processes. Chemical Engineering Journal 80, 177–188.

Bürger, R., Bustos, M. C., & Concha, F. (1999). Settling velocities of particulate systems: 9. Phenomenological theory of sedimentation processes: numerical simulation of the transient behaviour of flocculated suspensions in an ideal batch or continuous thickener. International Journal of Mineral Processing, 55(4), 267–282.

Bürger, R, & Concha, F. (1998). Mathematical model and numerical simulation of the settling of flocculated suspensions. International Journal of Multiphase Flow, 24, 1005–1023.

Bürger, R., Evje, S., Karlsen, K. H., & Lie, K. -A. (2000b). Numerical methods for the simulation of the settling of flocculated suspensions. Chemical Engineering Journal, 80(1–3), 91–104.

Bürger, R., Wendland, W. L., & Concha, F. (2000a). Model equations for gravitational sedimentation-consolidation processes. ZAMM-Journal of Applied Mathematics and Mechanics/Zeitschrift für Angewandte Mathematik und Mechanik, 80(2), 79–92.

Burrows, K., Carbajal, D., Kirsner, J., & Owen, B. (2004). Benchmark Performance: Zero Barite Sag and Significantly Reduced Downhole Losses with the Industry's First Clay-Free Synthetic-Based Fluid. In IADC/SPE Drilling Conference.

Caenn, R., & Chillingar, G. V. (1996). Drilling fluids: State of the art. Journal of Petroleum Science and Engineering, 14(3–4), 221–230.

Carbajal, D. L., Burress, C. N., Shumway, W., & Zhang, Y. (2009). Combining proven anti-sag technologies for HPHT North Sea applications: clay-free oil-based fluid and synthetic, sub-micron weight material. SPE/IADC Drilling Conference and Exhibition.

Davison, J. M., Clary, S., Saasen, A., Allouche, M., Bodin, D., & Nguyen, V-A. (1999). Rheology of various drilling fluid systems under deepwater drilling conditions and the importance of accurate predictions of downhole fluid hydraulics. SPE Annual Technical Conference and Exhibition.

Dedegil, M. Y. (1987). Drag coefficient and settling velocity of particles in non-Newtonian suspensions. Journal of Fluids Engineering, 109(3), 319-323.

Derkach, S. R. (2009). Rheology of emulsions. Advances in Colloid and Interface Science, 151(1–2), 1–23.

De Wolfe, R. C., Coffin, G. B., & Byrd, R. V. (1983). Effects of temperature & pressure rheology of less toxic oil muds. Offshore Europe. Society of Petroleum Engineers.

DHAST[SM] Dynamic High Angle settling test service analyzes potential for sag. http://www.halliburton.com/content/dam/ps/public/bar/contents/Data_Sheets/web/Sales_Data_Sheets/SDS-025.pdf.

Dingsøyr, E., Pedersen, E., & Taugbøl, K. (2004). Oil based drilling fluids with tailor-made rheological properties: results from a multivariate analysis. Annual Transactions of the Nordic Rheology Society, 12.

Dye, W., Hemphill, T., Gusler, W., & Mullen, G. (2001). Correlation of ultralow-shear-rate viscosity and dynamic barite sag. SPE Drilling & Completion, 16(01), 27–34.

Dye, W., Mullen, G., & Gusler, W. (2003). Drilling processes: the other half of the barite sag equation. SPE Asia Pacific Oil and Gas Conference and Exhibition.

Einstein, A. 1906. A new determination of molecular dimensions. Annalen der Physik (4) (19), 289–306.

Elkatatny, S. M., Nasr-El-Din, H. A., & Al-Bagoury, M. (2012). Evaluation of micronized ilmenite as weighting material in water-based drilling fluids for HPHT applications. SPE Kuwait International Petroleum Conference and Exhibition.

Ezeakacha, C. P., & Salehi, S. (2019a). A holistic approach to characterize mud loss using dynamic mud filtration data. Journal of Energy Resources Technology, 141(7), 072903.

Ezeakacha, C. P., & Salehi, S. (2019b). Experimental and statistical investigation of drilling fluid loss in porous media: part 2 (fractures). Journal of Natural Gas Science and Engineering, 65, 257–266.

Fakoya, M. F., & Ahmed, R. M. (2018). A generalized model for apparent viscosity of oil-based muds. Journal of Petroleum Science and Engineering, 165, 777–785.

Fimreite, G., Asko, A., Massam, J., Taugbol, K., Omland, T. H., Svanes, K., Kroken, W., Andreassen, E., & Saasen, A. (2004). Invert emulsion fluids for drilling through narrow hydraulic windows. IADC/SPE Drilling Conference.

Frank, M. W. (2006). Viscous fluid flow, third edition. McGraw-Hill.

Gast, A. P., & Russel, W. B. (1998). Simple ordering in complex fluids. Physics Today, 51, 24–31.

Gregoire, M. R., Hodder, M. H., Peng, S., & Massam, J. (2009). Successful drilling of a deviated, ultra-HTHP well using a micronised barite fluid. SPE/IADC Drilling Conference and Exhibition.

Growcock, F. B., Andrews, S. L., & Frederick, T. P. (1994). Physicochemical properties of synthetic drilling fluids. IADC/SPE Drilling Conference.

Growcock, F. B., & Frederick, T. P. (1996). Operational limits of synthetic drilling fluids. SPE Drilling & Completion, 11(03), 132–136.

Hanson, P. M., Trigg Jr, T. K., Rachal, G., & Zamora, M. (1990). Investigation of barite "sag" in weighted drilling fluids in highly deviated wells. SPE Annual Technical Conference and Exhibition.

Hashemian, Y. (2012a). Prediction of barite sag in horizontal annular flow. SPE Annual Technical Conference and Exhibition.

Hashemian, Y. A. (2012b). Experimental study and modeling of barite sag in annular flow (Doctoral dissertation, University of Tulsa).

Hashemian, Y., Miska, S., Yu, M., Ozbayoglu, E., & Takach, N. (2014). Numerical simulation and experiments of barite sag in horizontal annulus. American Journal of Numerical Analysis 2 (1): 14–19.

Hemphill, T. (2009). Comparisons of barite sag measurements and numerical prediction. National Technical Conference & Exhibition.

Hemphill, T., Campos, W., & Pilehvari, A. (1993). Yield-power law model more accurately predicts mud rheology. Oil & Gas Journal, 91(34).

Hemphill, T., & Larsen, T. I. (1996). Hole-cleaning capabilities of water- and oil-based drilling fluids: A comparative experimental study. SPE Drilling & Completion, 11(04), 201–207.

Hemphill, T., & Rojas, J. C. (2004). Improved prediction of barite sag using a fluid dynamics approach. AADE Drilling Fluid Conference.

Hermoso, J., Martínez-Boza, F., & Gallegos, C. (2014). Combined effect of pressure and temperature on the viscous behaviour of all-oil drilling fluids. Oil & Gas Science and Technology – Rev. IFP Energies nouvelles, 69(7), 1283–1296.

Herzhaft, B., Peysson, Y., Isambourg, P., Delepoulle, A., & Abdoulaye, T. (2001). Rheological Properties of Drilling Muds in Deep Offshore Conditions. SPE/IADC Drilling Conference.

Herzhaft, B., Rousseau, L., Neau, L., Moan, M., & Bossard, F. (2003). Influence of temperature and clays/emulsion microstructure on oil-based mud low shear rate rheology. SPE Journal, 8(03), 211–217.

Houwen, O. H., & Geehan, T. (1986). Rheology of oil-base muds. SPE Annual Technical Conference and Exhibition.

Ihenacho, P. C., Burby, M., Nasr, G. G., & Enyi, G. C. (2016). 50/50 oil-water ratio invert emulsion drilling mud using vegetable oil as continuous phase. International Journal of Chemical, Molecular, Nuclear, Materials and Metallurgical Engineering, 10(3), 298–301.

Jamison, D., & Clements, W. (1990) A new test method to characterize settling/sag tendencies of drilling fluids in extended reach drilling. ASME Drilling Technology Symposium.

Jefferson, D.T. (1991). New procedure helps monitor sag in the field. Energy Sources Technology Conference and Exhibition.

Jha, P. K., Mahto, V., & Saxena, V. K. (2014). Emulsion based drilling fluids: an overview. International Journal of ChemTech Research, 6(4), 2306–2315.

Kenny, P., & Hemphill, T. (1996). Hole-cleaning capabilities of an ester-based drilling fluid system. SPE Drilling & Completion, 11(01), 3–9.

Khalil, M., & Mohamed Jan, B. (2012). Herschel-Bulkley rheological parameters of a novel environmentally friendly lightweight biopolymer drilling fluid from xanthan gum and starch. Journal of Applied Polymer Science, 124(1), 595–606.

Kulkarni, S. D., Savari, S., Murphy, R., Hemphill, T., & Jamison, D. E. (2014). "Improvised" barite sag analysis for better drilling-fluid planning in extreme drilling environments. AADE Fluids Technical Conference and Exhibition.

Lamb, H. (1895). Viscosity, in: Hydrodynamics, Chapter 11.

Li, W., Zhao, X., Ji, Y., Peng, H., Chen, B., Liu, L., & Han, X. (2016). Investigation of Biodiesel-Based Drilling Fluid, Part 1: Biodiesel Evaluation, Invert-Emulsion Properties, and Development of a Novel Emulsifier Package. SPE Journal, 21(05), 1755–1766.

Mason, T. G., Bibette, J., & Weitz, D. A. (1996). Yielding and flow of monodisperse emulsions. Journal of Colloid and Interface Science, 179(2), 439–448.

Massam, J., Popplestone, A., & Burn, A. (2004). A unique technical solution to barite sag in drilling fluids. AADE Drilling Fluids Conference.

McKee, J. D. A., Dowrick, K., & Astleford, S. J. (1995). A new development towards improved synthetic based mud performance. SPE/IADC Drilling Conference.

McNerlin, B., & Oakey, N. D. (2011). Barite sag occurrence and resolution during Angolan completion operations. SPE Annual Technical Conference and Exhibition.

Muherei, M. A. (2016). Common versus Herschel-Bulkley drilling fluid models: Effect of their rheological parameters on dynamic particle settling velocity. American Scientific Research Journal for Engineering, Technology, and Sciences (ASRJETS), 16(1), 155–177.

Murphy, R. J., Jamison, D. E., Hemphill, T., Bell, S. A., & Albrecht, C. E. (2006). Apparatus for measuring the dynamic solids settling rates in drilling fluids. SPE Annual Technical Conference and Exhibition.

Murphy, R. J., Jamison, D. E., Hemphill, T., Bell, S. A., & Albrecht, C. E. (2008). Measuring and predicting dynamic sag. SPE Drilling & Completion, 23(02), 142–149.

Nguyen, T. C. (2009). Predicting dynamic barite sag in oil based drilling fluids (Doctoral dissertation, University of Tulsa).

Nguyen, T. C., Miska, S., Saasen, A., & Maxey, J. (2014). A quantitative study of the combined effect of drilling parameters on barite sag in oil-based drilling fluids. AADE National Technical Conference and Exhibition.

Nguyen, T., Miska, S., Yu, M., Takach, N., Ahmed, R., Saasen, A., Omland, T. H., & Maxey, J. (2011). Experimental study of dynamic barite sag in oil-based drilling fluids using a modified rotational viscometer and a flow loop. Journal of Petroleum Science and Engineering, 78(1), 160–165.

Omland, T. H. (2009). Particle settling in non-Newtonian drilling fluids (Doctoral dissertation, The University of Stavanger).

Omland, T. H., Albertsen, T., Taugbøl, K., Saasen, A., Svanes, K., & Amundsen, P. A. (2006). The effect of the synthetic- and oil-based drilling fluid's internal water-phase composition on barite sag. SPE Drilling & Completion, 21(02), 91–98.

Omland, T. H., Øvsthus, J., Svanes, K., Saasen, A., Jacob, H-J., Sveen, T., Hodne, H., & Amundsen, P. A. (2004). Weighting material sag. Annual Transactions of the Nordic Rheology Society, 12, 115–122.

Omland, T. H., Saasen, A., & Amundsen, P. A. (2007). Detection techniques determining weighting material sag in drilling fluid and relationship to rheology. Annual Transactions of the Nordic Rheology Society, 15, 277.

Ofite Sag Shoe assembly instruction manual. http://www.ofite.com/publications/instructions/121-130-22-instructions/file.

Parvizinia, A., Ahmed, R. M., & Osisanya, S. O. (2011). Experimental study on the phenomenon of barite sag. International Petroleum Technology Conference.

Paslay, P. R., Sathuvalli, U. B., & Payne, M. L. (2007). A phenomenological approach to analysis of barite sag in drilling muds. SPE Annual Technical Conference and Exhibition.

Phan-Thien, N., & Pham, D. C. (1997). Differential multiphase models for polydispersed suspensions and particulate solids. Journal of Non-Newtonian Fluid Mechanics, 72(2-3), 305–318.

Politte, M. D. (1985). Invert oil mud rheology as a function of temperature and pressure. SPE/IADC Drilling Conference.

Richardson, J. F., & Zaki, W. N. (1954). The sedimentation of a suspension of uniform spheres under conditions of viscous flow. Chemical Engineering Science, 3(2), 65–73.

Saasen, A. (2002). Sag of Weight Materials in Oil Based Drilling Fluids. IADC/SPE Asia Pacific Drilling Technology.

Saasen, A., Berntsen, M., Løklingholm, G., Igeltjørn, H., & Åsnes, K. (2001). The Effect of Drilling Fluid Base-Oil Properties on Occupational Hygiene and the Marine Environment. SPE Drilling & Completion, 16(03), 150–153.

Saasen, A., Liu, D., & Marken, C. D. (1995). Prediction of barite sag potential of drilling fluids from rheological measurements. SPE/IADC Drilling Conference.

Savari, S., Kulkarni, S., Maxey, J., & Teke, K. (2013). A comprehensive approach to barite sag analysis on field muds. AADE National Technical Conference and Exhibition.

Scott, P. D., Zamora, M., & Aldea, C. (2004). Barite-sag management: challenges, strategies, opportunities. IADC/SPE Drilling Conference.

Sinclair, A. R. (1970). Rheology of viscous fracturing fluids. Journal of Petroleum Technology, 22(06), 711–719.

Skalle, P., Backe, K. R., Lyomov, S. K., & Sveen, J. (1999). Barite segregation in inclined boreholes. Journal of Canadian Petroleum Technology, 38(13), 1–6.

Smith, H. V., & Arnold, K. E. (1987). Crude oil emulsions, in: Petroleum Engineering Handbook, Chapter 19, 1–34. Society of Petroleum Engineers.

Tadros, T. F. (2013). Emulsion Formation, Stability, and Rheology, in: Emulsion Formation and Stability. Wiley-VCH Verlag GmbH & Co. KGaA, Germany, 1–75.

Taugbøl, K., Gunnar, F., Prebensen, O. I., Kaare, S., Omland, T. H., Svela, P. E., & Breivik, D. H. (2005). Development and field testing of a unique high temperature and high pressure (HTHP) oil based drilling fluid with minimum rheology and maximum sag stability. Offshore Europe.

Taylor, G. I. (1932). The viscosity of a fluid containing small drops of another fluid. Proceedings of the Royal Society of London. Series A, Containing Papers of a Mathematical and Physical Character, 138(834), 41–48.

Tehrani, A. (2007). Behaviour of suspensions and emulsions in drilling fluids. Annual Transactions of the Nordic Rheology Society, 15.

Tehrani, M. A., Cliffe, A., Onwuzulike, I., & Froud-Williams, J. (2011). New laboratory technique for barite sag measurements. Offshore Mediterranean Conference and Exhibition.

Tehrani, A., & Popplestone, A. (2007). Can you improve rheology and mitigate barite sag in invert emulsion fluids through brine phase treatment? AADE National Technical Conference and Exhibition.

Tehrani, A., Popplestone, A., & Ayansina, T. (2009). Barite sag in invert-emulsion drilling fluids. Offshore Mediterranean Conference and Exhibition.

Tehrani, A., Zamora, M., & Power, D. (2004). Role of rheology in barite sag in SBM and OBM. AADE Drilling Fluids Conference.

Vajargah, A. K., Sullivan, G., & Oort, E. van. (2016). Automated fluid rheology and ECD management. SPE Deepwater Drilling and Completions Conference.

Van Zanten, R., Miller, J. J., & Baker, C. (2012). Improved stability of invert emulsion fluids. IADC/SPE Drilling Conference and Exhibition.

Wagle, V. B., Kulkarni, D., & Maghrabi, S. (2012). A great way to make your invert emulsion fluids green! SPE Asia Pacific Oil and Gas Conference and Exhibition.

Xiao, J., Nasr-El-Din, H. A., & Al-Bagoury, M. (2013). Evaluation of micronized ilmenite as a weighting material in oil-based drilling fluids for HPHT applications. SPE European Formation Damage Conference and Exhibition.

Yaron, I., & Gal-Or, B. (1972). On viscous flow and effective viscosity of concentrated suspensions and emulsions. Rheologica Acta, 11(3–4), 241–252.

Zamora, M. (2009). Mechanisms, measurement and mitigation of barite sag. Offshore Mediterranean Conference and Exhibition.

Zamora, M. (2011). Taming of the shoe. AADE National Technical Conference and Exhibition.

Zamora, M., & Bell, R. (2004). Improved wellsite test for monitoring barite sag. AADE Drilling Fluids Conference.

Zamora, M., & Jefferson, D. (1994). Controlling barite sag can reduce drilling problems. Oil & Gas Journal, 92(7).

Appendix A: OBM Rheological Parameters

Table A.1: OBM rheological parameters at organophilic clay concentration of 2.9 g/L and different volume fraction of the dispersed phase

ϕ_d = 0.14						
T (°C)	**τ_y (Pa)**	**K (Pas^n)**	**n**	**τ_y/τ_{yo}**	**K/K_o**	**n/n_o**
24	1.406	0.290	0.814	1	1	1
38	1.051	0.242	0.768	0.748	0.834	0.944
52	1.075	0.155	0.768	0.764	0.535	0.944
66	0.775	0.152	0.727	0.551	0.523	0.893
79	0.491	0.160	0.680	0.349	0.551	0.836
87	0.581	0.134	0.680	0.413	0.464	0.836
ϕ_d = 0.23						
T (°C)	**τ_y (Pa)**	**K (Pas^n)**	**n**	**τ_y/τ_{yo}**	**K/K_o**	**n/n_o**
24	9.604	0.964	0.711	1	1	1
38	7.063	0.715	0.680	0.735	0.742	0.956
52	5.233	0.718	0.617	0.545	0.746	0.867
66	4.744	0.495	0.616	0.494	0.514	0.866
79	3.984	0.381	0.615	0.415	0.395	0.865
87	3.264	0.335	0.610	0.340	0.347	0.858
ϕ_d = 0.32						
T (°C)	**τ_y (Pa)**	**K (Pas^n)**	**n**	**τ_y/τ_{yo}**	**K/K_o**	**n/n_o**
24	23.315	1.448	0.711	1	1	1
38	17.999	1.051	0.680	0.772	0.726	0.956
52	11.601	1.243	0.580	0.498	0.858	0.816
66	9.241	1.356	0.526	0.396	0.937	0.739
79	6.409	1.001	0.524	0.275	0.691	0.737
87	5.421	0.895	0.525	0.233	0.618	0.739

Table A.2: OBM rheological parameters at organophilic clay concentration of 8.6 g/L and different volume fraction of the dispersed phase

ϕ_d = 0.14						
T (°C)	**τ_y (Pa)**	**K (Pas^n)**	**n**	**τ_y/τ_{yo}**	**K/K_o**	**n/n_o**
24	2.698	0.321	0.814	1	1	1
38	1.984	0.266	0.768	0.735	0.827	0.944
52	1.953	0.176	0.768	0.724	0.548	0.944
66	1.365	0.168	0.727	0.506	0.524	0.893
79	1.018	0.173	0.682	0.377	0.538	0.838
87	0.898	0.149	0.683	0.333	0.463	0.839
ϕ_d = 0.23						
T (°C)	**τ_y (Pa)**	**K (Pas^n)**	**n**	**τ_y/τ_{yo}**	**K/K_o**	**n/n_o**
24	12.764	1.072	0.711	1	1	1
38	9.092	0.769	0.680	0.712	0.717	0.956
52	6.796	0.792	0.617	0.532	0.739	0.867
66	5.424	0.515	0.616	0.425	0.481	0.866
79	4.527	0.390	0.615	0.355	0.364	0.865
87	3.648	0.334	0.616	0.286	0.311	0.866
ϕ_d = 0.32						
T (°C)	**τ_y (Pa)**	**K (Pas^n)**	**n**	**τ_y/τ_{yo}**	**K/K_o**	**n/n_o**
24	25.605	1.495	0.711	1	1	1
38	19.708	1.117	0.680	0.770	0.747	0.956
52	13.849	1.289	0.600	0.541	0.862	0.844
66	10.058	1.413	0.526	0.393	0.946	0.739
79	8.132	1.101	0.524	0.318	0.737	0.737
87	6.876	0.969	0.525	0.269	0.649	0.739

Table A.3: OBM rheological parameters at organophilic clay concentration of 17.1 g/L and different volume fraction of the dispersed phase

ϕ_d = 0.14						
T (°C)	**τ_y (Pa)**	**K (Pas^n)**	**n**	**τ_y/τ_{yo}**	**K/K_o**	**n/n_o**
24	4.303	0.362	0.814	1	1	1
38	3.558	0.301	0.768	0.827	0.831	0.944
52	3.354	0.201	0.761	0.779	0.554	0.935
66	2.620	0.187	0.727	0.609	0.515	0.893
79	2.032	0.199	0.681	0.472	0.548	0.836
87	1.953	0.169	0.683	0.454	0.465	0.839
ϕ_d = 0.23						
T (°C)	**τ_y (Pa)**	**K (Pas^n)**	**n**	**τ_y/τ_{yo}**	**K/K_o**	**n/n_o**
24	12.745	1.260	0.711	1	1	1
38	10.050	0.874	0.680	0.789	0.693	0.956
52	7.606	0.855	0.617	0.597	0.678	0.867
66	6.373	0.579	0.616	0.500	0.459	0.866
79	5.784	0.442	0.615	0.454	0.350	0.865
87	5.139	0.376	0.616	0.403	0.299	0.866
ϕ_d = 0.32						
T (°C)	**τ_y (Pa)**	**K (Pas^n)**	**n**	**τ_y/τ_{yo}**	**K/K_o**	**n/n_o**
24	31.333	1.793	0.711	1	1	1
38	24.644	1.309	0.680	0.787	0.730	0.956
52	18.020	1.395	0.603	0.575	0.778	0.848
66	13.745	1.695	0.531	0.439	0.946	0.746
79	11.908	1.280	0.529	0.380	0.714	0.744
87	10.414	1.136	0.525	0.332	0.634	0.739

Appendix B: Fully Implicit Finite Difference Method

Recall Eqs. 6.1 – 6.9.

$$\frac{\partial \phi}{\partial t} + \frac{\partial}{\partial z}\left[q(t)\phi + f_{bk}(\phi)\right] = \frac{\partial}{\partial z}\left[a(\phi)\frac{\partial \phi}{\partial z}\right] \tag{B.1}$$

where:

$$f_{bk}(\phi) = -\frac{\Delta\rho g \phi^2 (1-\phi)^2}{\alpha(\phi)} \tag{B.2}$$

$$a(\phi) = -\frac{f_{bk}(\phi)\sigma_e'(\phi)}{\Delta\rho g \phi} \tag{B.3}$$

$$\sigma_e'(\phi) = \frac{d\sigma_e}{d\phi}\begin{cases} = 0 \ \text{ for } \phi \le \phi_c \\ > 0 \ \text{ for } \phi > \phi_c \end{cases} \tag{B.4}$$

The initial condition is:

$$\phi(z,0) = \phi_0(z), \quad z \in (0, L) \tag{B.5}$$

The boundary conditions are:

$$f_{bk}(\phi)|_{z=0} - a(\phi)\frac{\partial \phi}{\partial z}\Big|_{z=0} = 0 \tag{B.6}$$

$$\phi(L,t) = \phi_L(t), \quad t \in (0, T) \tag{B.7}$$

In the work of Bürger et al. (1999), the $f_{bk}(\phi)$ type proposed by Richardson and Zaki (1954) is:

$$f_{bk}(\phi) = v_\infty \phi (1-\phi)^{C+1} \tag{B.8}$$

Also, the $\sigma_e(\phi)$ determined by Becker (1982) is:

$$\sigma_e(\phi) = \begin{cases} 0 \ \text{ for } \phi \le \phi_c \\ \alpha e^{\beta\phi} \ \text{ for } \phi > \phi_c \end{cases} \tag{B.9}$$

Let $A_1 = v_\infty$, $A_2 = C+1$, $A_3 = \alpha$, $A_4 = \beta$, and $A_5 = \Delta\rho$. Therefore, Eq. B.8 becomes:

$$f_{bk}(\phi) = A_1 \phi (1-\phi)^{A_2} \tag{B.10}$$

Equation B.3 becomes:

$$a(\phi) = -\frac{f_{bk}(\phi)\sigma_e'(\phi)}{A_5 g \phi} \tag{B.11}$$

From Eq. B.4, Eq. B.9 is differentiated to give:

$$\sigma_e'(\phi) = \begin{cases} 0 & \text{for } \phi \le \phi_c \\ A_3 A_4 e^{A_4 \phi} & \text{for } \phi > \phi_c \end{cases} \tag{B.12}$$

The discretization procedure is illustrated in Fig. B.1. The needed ϕ is evaluated at the center of the grid block while $f_{bk}(\phi)$, $a(\phi)$, and $\sigma_e(\phi)$ are evaluated at the interface between grid blocks.

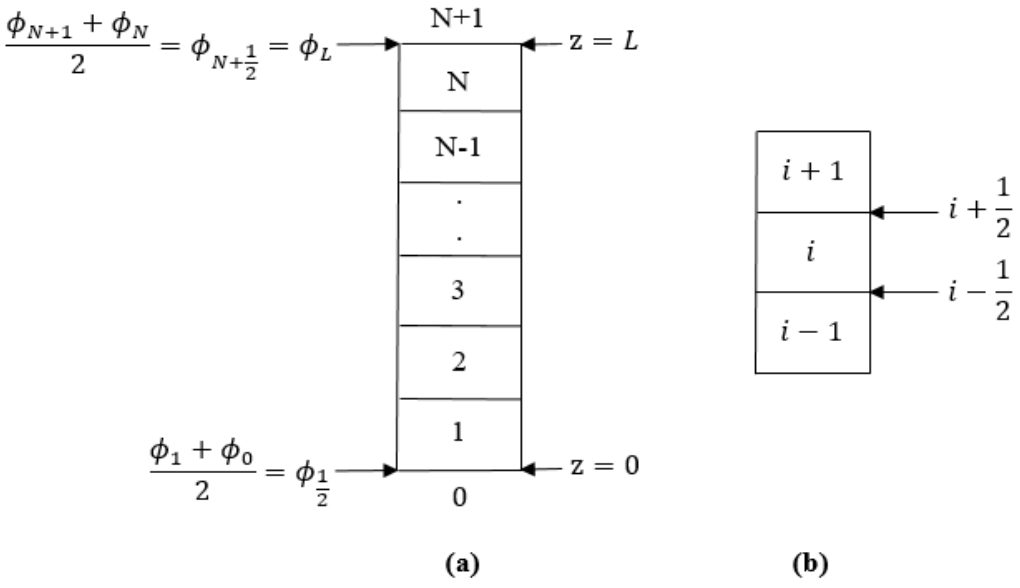

Fig. B.1: Grid block schematic

In Fig. B.1, ϕ_0 is volumetric solids concentration in the fictitious block below the bottom block; ϕ_{N+1} is volumetric solids concentration in the fictitious block above the top block; i is grid block number; $i \pm \frac{1}{2}$ is interface between grid blocks.

First, the boundary condition at the bottom interface (z = 0) is discretized. Hence, Eq. B.6 becomes:

$$f_{bk,\frac{1}{2}}^{m+1} - a_{\frac{1}{2}}^{m+1} \left(\frac{\phi_1^{m+1} - \phi_0^{m+1}}{\Delta z} \right) = 0 \tag{B.13}$$

where m indicates the time level of computation (m is old time level; $m+1$ is new time level); Δz is grid size.

Substituting Eq. B.11 into Eq. B.13 gives:

$$f_{bk,\frac{1}{2}}^{m+1} = -\frac{f_{bk,\frac{1}{2}}^{m+1}\sigma_{e,\frac{1}{2}}^{\prime,m+1}}{A_5 g \phi_{\frac{1}{2}}^{m+1}}\left(\frac{\phi_1^{m+1}-\phi_0^{m+1}}{\Delta z}\right) \tag{B.14}$$

$$\left(\frac{\phi_1^{m+1}-\phi_0^{m+1}}{\Delta z}\right) = -\frac{A_5 g \phi_{\frac{1}{2}}^{m+1}}{\sigma_{e,\frac{1}{2}}^{\prime,m+1}} \tag{B.15}$$

Volumetric solids concentration at the bottom interface is:

$$\phi_{\frac{1}{2}}^{m+1} = \frac{\phi_1^{m+1}+\phi_0^{m+1}}{2} \Longrightarrow \phi_0^{m+1} = 2\phi_{\frac{1}{2}}^{m+1} - \phi_1^{m+1} \tag{B.16}$$

With the appropriate differential of σ_e^{m+1} at the bottom interface, ϕ_0^{m+1} is evaluated.

$$\sigma_{e,\frac{1}{2}}^{\prime,m+1} = \begin{cases} 0, & \phi_{\frac{1}{2}}^{m+1} \le \phi_c = 0.23 \\ A_3 A_4 e^{A_4 \phi_{\frac{1}{2}}^{m+1}}, & \phi_{\frac{1}{2}}^{m+1} > \phi_c; \left(\frac{\phi_1^{m+1}-\phi_0^{m+1}}{\Delta z}\right) = -\frac{A_5 g \phi_{\frac{1}{2}}^{m+1}}{\sigma_{e,\frac{1}{2}}^{\prime,m+1}} = -\frac{A_5 g \phi_{\frac{1}{2}}^{m+1}}{A_3 A_4 e^{A_4 \phi_{\frac{1}{2}}^{m+1}}} = \end{cases}$$

$$-\frac{A_5 g\left(\phi_1^{m+1}+\phi_0^{m+1}\right)}{2A_3 A_4 e^{\frac{A_4}{2}\left(\phi_1^{m+1}+\phi_0^{m+1}\right)}} \tag{B.17}$$

From Eq. B.17, when $\phi_{\frac{1}{2}}^{m+1} \le \phi_c$, then $a_{\frac{1}{2}}^{m+1} = 0$. Therefore:

$$f_{bk,\frac{1}{2}}^{m+1} = 0 = A_1 \phi_{\frac{1}{2}}^{m+1}\left(1-\phi_{\frac{1}{2}}^{m+1}\right)^{A_2} \Longrightarrow 1-\phi_{\frac{1}{2}}^{m+1} = 0; \text{ Since } \phi_{\frac{1}{2}}^{m+1} \neq 0 \Longrightarrow \phi_{\frac{1}{2}}^{m+1} =$$

$$1 \Longrightarrow \phi_0^{m+1} = 2 - \phi_1^{m+1} \tag{B.18}$$

From Eq. B.17, when $\phi_{\frac{1}{2}}^{m+1} > \phi_c$, ϕ_0^{m+1} will be obtained by iteration using the Newton-Raphson method as shown below:

$$\frac{\phi_1^{m+1}-\phi_0^{m+1}}{\Delta z} = -\frac{A_5 g\left(\phi_1^{m+1}+\phi_0^{m+1}\right)}{2A_3 A_4 e^{\frac{A_4}{2}\left(\phi_1^{m+1}+\phi_0^{m+1}\right)}} \tag{B.19}$$

$$f_{\phi_0}^{m+1} = \frac{\phi_1^{m+1} - \phi_0^{m+1}}{\Delta z} + \frac{A_5 g\left(\phi_1^{m+1} + \phi_0^{m+1}\right)}{2A_3 A_4 e^{\frac{A_4}{2}\left(\phi_1^{m+1} + \phi_0^{m+1}\right)}} \tag{B.20}$$

$$\frac{\partial f_{\phi_0}^{m+1}}{\partial \phi_0^{m+1}} = \frac{-1}{\Delta z} +$$

$$\left[\frac{\left(2A_3 A_4 e^{\frac{A_4}{2}\left(\phi_1^{m+1} + \phi_0^{m+1}\right)}\right) A_5 g - \left(A_5 g\left(\phi_1^{m+1} + \phi_0^{m+1}\right)\right) A_3 (A_4)^2 e^{\frac{A_4}{2}\left(\phi_1^{m+1} + \phi_0^{m+1}\right)}}{4(A_3)^2 (A_4)^2 e^{A_4\left(\phi_1^{m+1} + \phi_0^{m+1}\right)}}\right] \tag{B.21}$$

Having discretized the boundary condition at the bottom interface, Eq. B.1 will now be discretized. Since the settling column is closed at the bottom, q ≡ 0. Equation B.1 becomes:

$$\frac{\phi_i^{m+1} - \phi_i^m}{\Delta t} + \frac{f_{bk,i+\frac{1}{2}}^{m+1} - f_{bk,i-\frac{1}{2}}^{m+1}}{\Delta z} = \frac{\left(a(\phi)\frac{\partial \phi}{\partial z}\right)_{i+\frac{1}{2}}^{m+1} - \left(a(\phi)\frac{\partial \phi}{\partial z}\right)_{i-\frac{1}{2}}^{m+1}}{\Delta z} \tag{B.22}$$

$$\frac{\phi_i^{m+1} - \phi_i^m}{\Delta t} + \frac{f_{bk,i+\frac{1}{2}}^{m+1} - f_{bk,i-\frac{1}{2}}^{m+1}}{\Delta z} = \frac{a_{i+\frac{1}{2}}^{m+1}\left(\frac{\phi_{i+1}^{m+1} - \phi_i^{m+1}}{\Delta z}\right) - a_{i-\frac{1}{2}}^{m+1}\left(\frac{\phi_i^{m+1} - \phi_{i-1}^{m+1}}{\Delta z}\right)}{\Delta z} \tag{B.23}$$

$$\frac{\phi_i^{m+1} - \phi_i^m}{\Delta t} + \frac{f_{bk,i+\frac{1}{2}}^{m+1} - f_{bk,i-\frac{1}{2}}^{m+1}}{\Delta z} = \frac{a_{i+\frac{1}{2}}^{m+1}(\phi_{i+1}^{m+1} - \phi_i^{m+1}) - a_{i-\frac{1}{2}}^{m+1}(\phi_i^{m+1} - \phi_{i-1}^{m+1})}{\Delta z^2} \tag{B.24}$$

$$\phi_i^{m+1} - \phi_i^m + \frac{\Delta t}{\Delta z}\left(f_{bk,i+\frac{1}{2}}^{m+1} - f_{bk,i-\frac{1}{2}}^{m+1}\right) = \frac{\Delta t}{\Delta z^2}\left[a_{i+\frac{1}{2}}^{m+1}\left(\phi_{i+1}^{m+1} - \phi_i^{m+1}\right) - a_{i-\frac{1}{2}}^{m+1}\left(\phi_i^{m+1} - \phi_{i-1}^{m+1}\right)\right] \tag{B.25}$$

where Δt is time step.

The expression for the residual function, f_i^{m+1}, will now be written. This applies to blocks 2 – (N-1).

$$f_i^{m+1} = \phi_i^{m+1} - \phi_i^m + \frac{\Delta t}{\Delta z}\left(f_{bk,i+\frac{1}{2}}^{m+1} - f_{bk,i-\frac{1}{2}}^{m+1}\right) - \frac{\Delta t}{\Delta z^2}\left[a_{i+\frac{1}{2}}^{m+1}\left(\phi_{i+1}^{m+1} - \phi_i^{m+1}\right) - a_{i-\frac{1}{2}}^{m+1}\left(\phi_i^{m+1} - \phi_{i-1}^{m+1}\right)\right] \tag{B.26}$$

where:

$$f_{bk,i+\frac{1}{2}}^{m+1} = A_1 \phi_{i+\frac{1}{2}}^{m+1} \left(1 - \phi_{i+\frac{1}{2}}^{m+1}\right)^{A_2} \tag{B.27}$$

$$f_{bk,i-\frac{1}{2}}^{m+1} = A_1 \phi_{i-\frac{1}{2}}^{m+1} \left(1 - \phi_{i-\frac{1}{2}}^{m+1}\right)^{A_2} \tag{B.28}$$

$$a_{i+\frac{1}{2}}^{m+1} = -\frac{f_{bk,i+\frac{1}{2}}^{m+1} \sigma_{e,i+\frac{1}{2}}^{\prime,m+1}}{A_5 g \phi_{i+\frac{1}{2}}^{m+1}} \tag{B.29}$$

$$a_{i-\frac{1}{2}}^{m+1} = -\frac{f_{bk,i-\frac{1}{2}}^{m+1} \sigma_{e,i-\frac{1}{2}}^{\prime,m+1}}{A_5 g \phi_{i-\frac{1}{2}}^{m+1}} \tag{B.30}$$

$$\sigma_{e,i+\frac{1}{2}}^{\prime,m+1} = \begin{cases} 0, \ \phi_{i+\frac{1}{2}}^{m+1} \leq \phi_c = 0.23 \\ A_3 A_4 e^{A_4 \phi_{i+\frac{1}{2}}^{m+1}}, \ \phi_{i+\frac{1}{2}}^{m+1} > \phi_c \end{cases} \tag{B.31}$$

$$\sigma_{e,i-\frac{1}{2}}^{\prime,m+1} = \begin{cases} 0, \ \phi_{i-\frac{1}{2}}^{m+1} \leq \phi_c = 0.23 \\ A_3 A_4 e^{A_4 \phi_{i-\frac{1}{2}}^{m+1}}, \ \phi_{i-\frac{1}{2}}^{m+1} > \phi_c \end{cases} \tag{B.32}$$

$$\phi_{i+\frac{1}{2}}^{m+1} = \frac{\phi_{i+1}^{m+1} + \phi_i^{m+1}}{2} \tag{B.33}$$

$$\phi_{i-\frac{1}{2}}^{m+1} = \frac{\phi_i^{m+1} + \phi_{i-1}^{m+1}}{2} \tag{B.34}$$

Using Eq. B.26, the residual function for block 1 is:

$$f_1^{m+1} = \phi_1^{m+1} - \phi_1^m + \frac{\Delta t}{\Delta z}\left(f_{bk,\frac{3}{2}}^{m+1} - f_{bk,\frac{1}{2}}^{m+1}\right) - \frac{\Delta t}{\Delta z^2}\left[a_{\frac{3}{2}}^{m+1}(\phi_2^{m+1} - \phi_1^{m+1}) - a_{\frac{1}{2}}^{m+1}(\phi_1^{m+1} - \phi_0^{m+1})\right] \tag{B.35}$$

where:

$$f_{bk,\frac{3}{2}}^{m+1} = A_1 \phi_{\frac{3}{2}}^{m+1} \left(1 - \phi_{\frac{3}{2}}^{m+1}\right)^{A_2} \tag{B.36}$$

$$f_{bk,\frac{1}{2}}^{m+1} = A_1 \phi_{\frac{1}{2}}^{m+1} \left(1 - \phi_{\frac{1}{2}}^{m+1}\right)^{A_2} \tag{B.37}$$

$$a_{\frac{3}{2}}^{m+1} = -\frac{f_{bk,\frac{3}{2}}^{m+1} \sigma_{e,\frac{3}{2}}^{\prime,m+1}}{A_5 g \phi_{\frac{3}{2}}^{m+1}} \tag{B.38}$$

$$a_{\frac{1}{2}}^{m+1} = -\frac{f_{bk,\frac{1}{2}}^{m+1} \sigma_{e,\frac{1}{2}}^{\prime,m+1}}{A_5 g \phi_{\frac{1}{2}}^{m+1}} \tag{B.39}$$

$$\sigma_{e,\frac{3}{2}}^{\prime,m+1} = \begin{cases} 0, & \phi_{\frac{3}{2}}^{m+1} \le \phi_c = 0.23 \\ A_3 A_4 e^{A_4 \phi_{\frac{3}{2}}^{m+1}}, & \phi_{\frac{3}{2}}^{m+1} > \phi_c \end{cases} \tag{B.40}$$

$$\sigma_{e,\frac{1}{2}}^{\prime,m+1} = \begin{cases} 0, & \phi_{\frac{1}{2}}^{m+1} \le \phi_c = 0.23 \\ A_3 A_4 e^{A_4 \phi_{\frac{1}{2}}^{m+1}}, & \phi_{\frac{1}{2}}^{m+1} > \phi_c \end{cases} \tag{B.41}$$

$$\phi_{\frac{3}{2}}^{m+1} = \frac{\phi_1^{m+1} + \phi_2^{m+1}}{2} \tag{B.42}$$

$$\phi_{\frac{1}{2}}^{m+1} = \frac{\phi_0^{m+1} + \phi_1^{m+1}}{2} \tag{B.43}$$

From Eqs. B.18 and B.19,

$$\phi_0^{m+1} = \begin{cases} 2 - \phi_1^{m+1}, & \phi_{\frac{1}{2}}^{m+1} \le \phi_c = 0.23 \\ \frac{\phi_1^{m+1} - \phi_0^{m+1}}{\Delta z} = -\frac{A_5 g \left(\phi_1^{m+1} + \phi_0^{m+1}\right)}{2 A_3 A_4 e^{\frac{A_4}{2}\left(\phi_1^{m+1} + \phi_0^{m+1}\right)}}, & \phi_{\frac{1}{2}}^{m+1} > \phi_c \end{cases} \tag{B.44}$$

From Eq. B.44, when $\phi_{\frac{1}{2}}^{m+1} > \phi_c$, ϕ_0^{m+1} will be obtained by iteration using the Newton-Raphson method as shown in Eqs. B.20 and B.21.

Again, using Eq. B.26, the residual function for block N is:

$$f_N^{m+1} = \phi_N^{m+1} - \phi_N^m + \frac{\Delta t}{\Delta z}\left(f_{bk,N+\frac{1}{2}}^{m+1} - f_{bk,N-\frac{1}{2}}^{m+1}\right) - \frac{\Delta t}{\Delta z^2}\left[a_{N+\frac{1}{2}}^{m+1}(\phi_{N+1}^{m+1} - \phi_N^{m+1}) - a_{N-\frac{1}{2}}^{m+1}(\phi_N^{m+1} - \phi_{N-1}^{m+1})\right] \quad \text{(B.45)}$$

where:

$$f_{bk,N+\frac{1}{2}}^{m+1} = A_1\phi_{N+\frac{1}{2}}^{m+1}\left(1 - \phi_{N+\frac{1}{2}}^{m+1}\right)^{A_2} \quad \text{(B.46)}$$

$$f_{bk,N-\frac{1}{2}}^{m+1} = A_1\phi_{N-\frac{1}{2}}^{m+1}\left(1 - \phi_{N-\frac{1}{2}}^{m+1}\right)^{A_2} \quad \text{(B.47)}$$

$$a_{N+\frac{1}{2}}^{m+1} = -\frac{f_{bk,N+\frac{1}{2}}^{m+1}\sigma_{e,N+\frac{1}{2}}^{\prime,m+1}}{A_5 g\phi_{N+\frac{1}{2}}^{m+1}} \quad \text{(B.48)}$$

$$a_{N-\frac{1}{2}}^{m+1} = -\frac{f_{bk,N-\frac{1}{2}}^{m+1}\sigma_{e,N-\frac{1}{2}}^{\prime,m+1}}{A_5 g\phi_{N-\frac{1}{2}}^{m+1}} \quad \text{(B.49)}$$

$$\sigma_{e,N+\frac{1}{2}}^{\prime,m+1} = \begin{cases} 0, & \phi_{N+\frac{1}{2}}^{m+1} \le \phi_c = 0.23 \\ A_3A_4e^{A_4\phi_{N+\frac{1}{2}}^{m+1}}, & \phi_{N+\frac{1}{2}}^{m+1} > \phi_c \end{cases} \quad \text{(B.50)}$$

$$\sigma_{e,N-\frac{1}{2}}^{\prime,m+1} = \begin{cases} 0, & \phi_{N-\frac{1}{2}}^{m+1} \le \phi_c = 0.23 \\ A_3A_4e^{A_4\phi_{N-\frac{1}{2}}^{m+1}}, & \phi_{N-\frac{1}{2}}^{m+1} > \phi_c \end{cases} \quad \text{(B.51)}$$

In the expression for $\phi_{N+\frac{1}{2}}^{m+1}$, the top boundary condition is implemented to evaluate ϕ_{N+1}^{m+1} as shown below:

$$\phi_{N+\frac{1}{2}}^{m+1} = \frac{\phi_{N+1}^{m+1} + \phi_N^{m+1}}{2} \Longrightarrow \phi_{N+1}^{m+1} = 2\phi_{N+\frac{1}{2}}^{m+1} - \phi_N^{m+1} = 2\phi_L - \phi_N^{m+1} \quad \text{(B.52)}$$

$$\phi_{N-\frac{1}{2}}^{m+1} = \frac{\phi_N^{m+1} + \phi_{N-1}^{m+1}}{2} \quad \text{(B.53)}$$

Now, the elements of the Jacobian matrix need to be computed by differentiating the residual functions. The elements of the Jacobian matrix from block 1 is evaluated as:

$$\frac{\partial f_1^{m+1}}{\partial \phi_1^{m+1}} = 1 + \frac{\Delta t}{\Delta z}\left(\frac{\partial f_{bk,\frac{3}{2}}^{m+1}}{\partial \phi_1^{m+1}} - \frac{\partial f_{bk,\frac{1}{2}}^{m+1}}{\partial \phi_1^{m+1}}\right) - \frac{\Delta t}{\Delta z^2}\left[a_{\frac{3}{2}}^{m+1}(-1) + (\phi_2^{m+1} - \phi_1^{m+1})\frac{\partial a_{\frac{3}{2}}^{m+1}}{\partial \phi_1^{m+1}} - a_{\frac{1}{2}}^{m+1}\left(1 - \frac{\partial \phi_0^{m+1}}{\partial \phi_1^{m+1}}\right) - (\phi_1^{m+1} - \phi_0^{m+1})\frac{\partial a_{\frac{1}{2}}^{m+1}}{\partial \phi_1^{m+1}}\right] \quad \text{(B.54)}$$

$$\frac{\partial f_1^{m+1}}{\partial \phi_2^{m+1}} = \frac{\Delta t}{\Delta z}\left(\frac{\partial f_{bk,\frac{3}{2}}^{m+1}}{\partial \phi_2^{m+1}} - \cancel{\frac{\partial f_{bk,\frac{1}{2}}^{m+1}}{\partial \phi_2^{m+1}}}^{=0}\right) - \frac{\Delta t}{\Delta z^2}\left[a_{\frac{3}{2}}^{m+1}(1) + (\phi_2^{m+1} - \phi_1^{m+1})\frac{\partial a_{\frac{3}{2}}^{m+1}}{\partial \phi_2^{m+1}} - 0 - 0\right] \quad \text{(B.55)}$$

The differential of $f_{bk,\frac{1}{2}}^{m+1}$ goes to zero in Eq. B.55 because ϕ_2 is not adjacent to $\phi_{\frac{1}{2}}$. Equation B.55 becomes:

$$\frac{\partial f_1^{m+1}}{\partial \phi_2^{m+1}} = \frac{\Delta t}{\Delta z}\left(\frac{\partial f_{bk,\frac{3}{2}}^{m+1}}{\partial \phi_2^{m+1}}\right) - \frac{\Delta t}{\Delta z^2}\left[a_{\frac{3}{2}}^{m+1} + (\phi_2^{m+1} - \phi_1^{m+1})\frac{\partial a_{\frac{3}{2}}^{m+1}}{\partial \phi_2^{m+1}}\right] \quad \text{(B.56)}$$

The derivation of each differential in the elements of the Jacobian matrix from block 1 is shown below:

$$\frac{\partial f_{bk,\frac{3}{2}}^{m+1}}{\partial \phi_1^{m+1}} = \frac{\partial f_{bk,\frac{3}{2}}^{m+1}}{\partial \phi_{\frac{3}{2}}^{m+1}} \times \frac{\partial \phi_{\frac{3}{2}}^{m+1}}{\partial \phi_1^{m+1}} \quad \text{(B.57)}$$

$$\frac{\partial f_{bk,\frac{3}{2}}^{m+1}}{\partial \phi_{\frac{3}{2}}^{m+1}} = -A_1 A_2 \phi_{\frac{3}{2}}^{m+1}\left(1 - \phi_{\frac{3}{2}}^{m+1}\right)^{A_2 - 1} + A_1\left(1 - \phi_{\frac{3}{2}}^{m+1}\right)^{A_2} \quad \text{(B.58)}$$

$$\frac{\partial \phi_{\frac{3}{2}}^{m+1}}{\partial \phi_1^{m+1}} = \frac{1}{2} \quad \text{(B.59)}$$

$$\frac{\partial f_{bk,\frac{1}{2}}^{m+1}}{\partial \phi_1^{m+1}} = \frac{\partial f_{bk,\frac{1}{2}}^{m+1}}{\partial \phi_{\frac{1}{2}}^{m+1}} \times \frac{\partial \phi_{\frac{1}{2}}^{m+1}}{\partial \phi_1^{m+1}} \quad \text{(B.60)}$$

$$\frac{\partial f_{bk,\frac{1}{2}}^{m+1}}{\partial \phi_{\frac{1}{2}}^{m+1}} = -A_1 A_2 \phi_{\frac{1}{2}}^{m+1}\left(1-\phi_{\frac{1}{2}}^{m+1}\right)^{A_2-1} + A_1\left(1-\phi_{\frac{1}{2}}^{m+1}\right)^{A_2} \tag{B.61}$$

$$\frac{\partial \phi_{\frac{1}{2}}^{m+1}}{\partial \phi_1^{m+1}} = \frac{1}{2} \tag{B.62}$$

$$\frac{\partial a_{\frac{3}{2}}^{m+1}}{\partial \phi_1^{m+1}} = \frac{\partial a_{\frac{3}{2}}^{m+1}}{\partial \phi_{\frac{3}{2}}^{m+1}} \times \frac{\partial \phi_{\frac{3}{2}}^{m+1}}{\partial \phi_1^{m+1}} \tag{B.63}$$

$$\frac{\partial a_{\frac{3}{2}}^{m+1}}{\partial \phi_{\frac{3}{2}}^{m+1}} = -\left[\frac{A_5 g \phi_{\frac{3}{2}}^{m+1}\left[f_{bk,\frac{3}{2}}^{m+1}\left(\frac{\partial \sigma_{e,\frac{3}{2}}^{\prime,m+1}}{\partial \phi_{\frac{3}{2}}^{m+1}}\right)+\sigma_{e,\frac{3}{2}}^{\prime,m+1}\left(\frac{\partial f_{bk,\frac{3}{2}}^{m+1}}{\partial \phi_{\frac{3}{2}}^{m+1}}\right)\right]-f_{bk,\frac{3}{2}}^{m+1}\sigma_{e,\frac{3}{2}}^{\prime,m+1}(A_5 g)}{A_5^2 g^2\left(\phi_{\frac{3}{2}}^{m+1}\right)^2}\right] \tag{B.64}$$

$$\sigma_{e,\frac{3}{2}}^{\prime,m+1} = \begin{cases} 0, \ \phi_{\frac{3}{2}}^{m+1} \le \phi_c = 0.23; & \frac{\partial \sigma_{e,\frac{3}{2}}^{\prime,m+1}}{\partial \phi_{\frac{3}{2}}^{m+1}} = 0 \\ A_3 A_4 e^{A_4 \phi_{\frac{3}{2}}^{m+1}}, \ \phi_{\frac{3}{2}}^{m+1} > \phi_c; & \frac{\partial \sigma_{e,\frac{3}{2}}^{\prime,m+1}}{\partial \phi_{\frac{3}{2}}^{m+1}} = A_3 A_4^2 e^{A_4 \phi_{\frac{3}{2}}^{m+1}} \end{cases} \tag{B.65}$$

$\frac{\partial \phi_0^{m+1}}{\partial \phi_1^{m+1}}$ will be evaluated from Eq. B.44. When $\phi_{\frac{1}{2}}^{m+1} \le \phi_c$,

$$\frac{\partial \phi_0^{m+1}}{\partial \phi_1^{m+1}} = -1 \tag{B.66}$$

When $\phi_{\frac{1}{2}}^{m+1} > \phi_c$, $\frac{\partial \phi_0^{m+1}}{\partial \phi_1^{m+1}}$ will be obtained by iteration using the Newton-Raphson method as shown below:

$$\phi_0^{m+1} = \phi_1^{m+1} + \frac{A_5 g \Delta z\left(\phi_1^{m+1}+\phi_0^{m+1}\right)}{2A_3 A_4 e^{\frac{A_4}{2}\left(\phi_1^{m+1}+\phi_0^{m+1}\right)}} \tag{B.67}$$

$$\frac{\partial \phi_0^{m+1}}{\partial \phi_1^{m+1}} = 1 + \left[\frac{\left(2A_3 A_4 e^{\frac{A_4}{2}\left(\phi_1^{m+1}+\phi_0^{m+1}\right)}\right)A_5 g \Delta z\left(1+\frac{\partial \phi_0^{m+1}}{\partial \phi_1^{m+1}}\right)-\left(A_5 g \Delta z\left(\phi_1^{m+1}+\phi_0^{m+1}\right)\right)A_3 (A_4)^2\left(1+\frac{\partial \phi_0^{m+1}}{\partial \phi_1^{m+1}}\right)e^{\frac{A_4}{2}\left(\phi_1^{m+1}+\phi_0^{m+1}\right)}}{4(A_3)^2 (A_4)^2 e^{A_4\left(\phi_1^{m+1}+\phi_0^{m+1}\right)}}\right] \tag{B.68}$$

$$f_{\frac{\partial\phi_0^{m+1}}{\partial\phi_1^{m+1}}} = \frac{\partial\phi_0^{m+1}}{\partial\phi_1^{m+1}} - 1 -$$

$$\left[\frac{\left(2A_3A_4e^{\frac{A_4}{2}\left(\phi_1^{m+1}+\phi_0^{m+1}\right)}\right)A_5g\Delta z\left(1+\frac{\partial\phi_0^{m+1}}{\partial\phi_1^{m+1}}\right)-\left(A_5g\Delta z\left(\phi_1^{m+1}+\phi_0^{m+1}\right)\right)A_3(A_4)^2\left(1+\frac{\partial\phi_0^{m+1}}{\partial\phi_1^{m+1}}\right)e^{\frac{A_4}{2}\left(\phi_1^{m+1}+\phi_0^{m+1}\right)}}{4(A_3)^2(A_4)^2e^{A_4\left(\phi_1^{m+1}+\phi_0^{m+1}\right)}}\right] \tag{B.69}$$

$$\frac{\partial f_{\frac{\partial\phi_0^{m+1}}{\partial\phi_1^{m+1}}}}{\partial\frac{\partial\phi_0^{m+1}}{\partial\phi_1^{m+1}}} = 1 - \left[\frac{\left(2A_3A_4e^{\frac{A_4}{2}\left(\phi_1^{m+1}+\phi_0^{m+1}\right)}\right)A_5g\Delta z-\left(A_5g\Delta z\left(\phi_1^{m+1}+\phi_0^{m+1}\right)\right)A_3(A_4)^2e^{\frac{A_4}{2}\left(\phi_1^{m+1}+\phi_0^{m+1}\right)}}{4(A_3)^2(A_4)^2e^{A_4\left(\phi_1^{m+1}+\phi_0^{m+1}\right)}}\right] \tag{B.70}$$

$$\frac{\partial a_{\frac{1}{2}}^{m+1}}{\partial\phi_1^{m+1}} = \frac{\partial a_{\frac{1}{2}}^{m+1}}{\partial\phi_{\frac{1}{2}}^{m+1}} \times \frac{\partial\phi_{\frac{1}{2}}^{m+1}}{\partial\phi_1^{m+1}} \tag{B.71}$$

$$\frac{\partial a_{\frac{1}{2}}^{m+1}}{\partial\phi_{\frac{1}{2}}^{m+1}} = -\left[\frac{A_5g\phi_{\frac{1}{2}}^{m+1}\left[f_{bk,\frac{1}{2}}^{m+1}\left(\frac{\partial\sigma_{e,\frac{1}{2}}^{\prime,m+1}}{\partial\phi_{\frac{1}{2}}^{m+1}}\right)+\sigma_{e,\frac{1}{2}}^{\prime,m+1}\left(\frac{\partial f_{bk,\frac{1}{2}}^{m+1}}{\partial\phi_{\frac{1}{2}}^{m+1}}\right)\right]-f_{bk,\frac{1}{2}}^{m+1}\sigma_{e,\frac{1}{2}}^{\prime,m+1}(A_5g)}{A_5^2g^2\left(\phi_{\frac{1}{2}}^{m+1}\right)^2}\right] \tag{B.72}$$

$$\sigma_{e,\frac{1}{2}}^{\prime,m+1} = \begin{cases} 0,\ \phi_{\frac{1}{2}}^{m+1} \le \phi_c = 0.23; & \frac{\partial\sigma_{e,\frac{1}{2}}^{\prime,m+1}}{\partial\phi_{\frac{1}{2}}^{m+1}} = 0 \\ A_3A_4e^{A_4\phi_{\frac{1}{2}}^{m+1}},\ \phi_{\frac{1}{2}}^{m+1} > \phi_c; & \frac{\partial\sigma_{e,\frac{1}{2}}^{\prime,m+1}}{\partial\phi_{\frac{1}{2}}^{m+1}} = A_3A_4^2e^{A_4\phi_{\frac{1}{2}}^{m+1}} \end{cases} \tag{B.73}$$

$$\frac{\partial f_{bk,\frac{3}{2}}^{m+1}}{\partial\phi_2^{m+1}} = \frac{\partial f_{bk,\frac{3}{2}}^{m+1}}{\partial\phi_{\frac{3}{2}}^{m+1}} \times \frac{\partial\phi_{\frac{3}{2}}^{m+1}}{\partial\phi_2^{m+1}} \tag{B.74}$$

$$\frac{\partial\phi_{\frac{3}{2}}^{m+1}}{\partial\phi_2^{m+1}} = \frac{1}{2} \tag{B.75}$$

$$\frac{\partial a_{\frac{3}{2}}^{m+1}}{\partial\phi_2^{m+1}} = \frac{\partial a_{\frac{3}{2}}^{m+1}}{\partial\phi_{\frac{3}{2}}^{m+1}} \times \frac{\partial\phi_{\frac{3}{2}}^{m+1}}{\partial\phi_2^{m+1}} \tag{B.76}$$

Also, the elements of the Jacobian matrix from block N is evaluated as:

$$\frac{\partial f_N^{m+1}}{\partial \phi_N^{m+1}} = 1 + \frac{\Delta t}{\Delta z}\left(\frac{\partial f_{bk,N+\frac{1}{2}}^{m+1}}{\partial \phi_N^{m+1}} - \frac{\partial f_{bk,N-\frac{1}{2}}^{m+1}}{\partial \phi_N^{m+1}}\right) - \frac{\Delta t}{\Delta z^2}\left[a_{N+\frac{1}{2}}^{m+1}\left(\frac{\partial \phi_{N+1}^{m+1}}{\partial \phi_N^{m+1}} - 1\right) + (\phi_{N+1}^{m+1} - \phi_N^{m+1})\frac{\partial a_{N+\frac{1}{2}}^{m+1}}{\partial \phi_N^{m+1}} - a_{N-\frac{1}{2}}^{m+1}(1) - (\phi_N^{m+1} - \phi_{N-1}^{m+1})\frac{\partial a_{N-\frac{1}{2}}^{m+1}}{\partial \phi_N^{m+1}}\right] \quad \text{(B.77)}$$

$$\frac{\partial f_N^{m+1}}{\partial \phi_{N-1}^{m+1}} = \frac{\Delta t}{\Delta z}\left(\cancel{\frac{\partial f_{bk,N+\frac{1}{2}}^{m+1}}{\partial \phi_{N-1}^{m+1}}}^{=0} - \frac{\partial f_{bk,N-\frac{1}{2}}^{m+1}}{\partial \phi_{N-1}^{m+1}}\right) - \frac{\Delta t}{\Delta z^2}\left[0 + 0 - a_{N-\frac{1}{2}}^{m+1}(-1) - (\phi_N^{m+1} - \phi_{N-1}^{m+1})\frac{\partial a_{N-\frac{1}{2}}^{m+1}}{\partial \phi_{N-1}^{m+1}}\right] \quad \text{(B.78)}$$

Equation B.78 becomes:

$$\frac{\partial f_N^{m+1}}{\partial \phi_{N-1}^{m+1}} = -\frac{\Delta t}{\Delta z}\left(\frac{\partial f_{bk,N-\frac{1}{2}}^{m+1}}{\partial \phi_{N-1}^{m+1}}\right) - \frac{\Delta t}{\Delta z^2}\left[a_{N-\frac{1}{2}}^{m+1} - (\phi_N^{m+1} - \phi_{N-1}^{m+1})\frac{\partial a_{N-\frac{1}{2}}^{m+1}}{\partial \phi_{N-1}^{m+1}}\right] \quad \text{(B.79)}$$

The derivation of each differential in the elements of the Jacobian matrix from block N is shown below:

$$\frac{\partial f_{bk,N+\frac{1}{2}}^{m+1}}{\partial \phi_N^{m+1}} = \frac{\partial f_{bk,N+\frac{1}{2}}^{m+1}}{\partial \phi_{N+\frac{1}{2}}^{m+1}} \times \frac{\partial \phi_{N+\frac{1}{2}}^{m+1}}{\partial \phi_N^{m+1}} \quad \text{(B.80)}$$

$$\frac{\partial f_{bk,N+\frac{1}{2}}^{m+1}}{\phi_{N+\frac{1}{2}}^{m+1}} = -A_1 A_2 \phi_{N+\frac{1}{2}}^{m+1}\left(1 - \phi_{N+\frac{1}{2}}^{m+1}\right)^{A_2-1} + A_1\left(1 - \phi_{N+\frac{1}{2}}^{m+1}\right)^{A_2} \quad \text{(B.81)}$$

$$\frac{\partial \phi_{N+\frac{1}{2}}^{m+1}}{\partial \phi_N^{m+1}} = \frac{1}{2} \quad \text{(B.82)}$$

$$\frac{\partial f_{bk,N-\frac{1}{2}}^{m+1}}{\partial \phi_N^{m+1}} = \frac{\partial f_{bk,N-\frac{1}{2}}^{m+1}}{\partial \phi_{N-\frac{1}{2}}^{m+1}} \times \frac{\partial \phi_{N-\frac{1}{2}}^{m+1}}{\partial \phi_N^{m+1}} \quad \text{(B.83)}$$

$$\frac{\partial f_{bk,N-\frac{1}{2}}^{m+1}}{\partial \phi_{N-\frac{1}{2}}^{m+1}} = -A_1 A_2 \phi_{N-\frac{1}{2}}^{m+1}\left(1 - \phi_{N-\frac{1}{2}}^{m+1}\right)^{A_2-1} + A_1\left(1 - \phi_{N-\frac{1}{2}}^{m+1}\right)^{A_2} \quad \text{(B.84)}$$

$$\frac{\partial \phi_{N-\frac{1}{2}}^{m+1}}{\partial \phi_N^{m+1}} = \frac{1}{2} \quad \text{(B.85)}$$

From Eq. B.52,

$$\frac{\partial \phi_{N+1}^{m+1}}{\partial \phi_{N}^{m+1}} = -1 \tag{B.86}$$

$$\frac{\partial a_{N+\frac{1}{2}}^{m+1}}{\partial \phi_{N}^{m+1}} = \frac{\partial a_{N+\frac{1}{2}}^{m+1}}{\partial \phi_{N+\frac{1}{2}}^{m+1}} \times \frac{\partial \phi_{N+\frac{1}{2}}^{m+1}}{\partial \phi_{N}^{m+1}} \tag{B.87}$$

$$\frac{\partial a_{N+\frac{1}{2}}^{m+1}}{\partial \phi_{N+\frac{1}{2}}^{m+1}} = -\left[\frac{A_5 g \phi_{N+\frac{1}{2}}^{m+1}\left[f_{bk,N+\frac{1}{2}}^{m+1}\left(\frac{\partial \sigma'^{,m+1}_{e,N+\frac{1}{2}}}{\partial \phi_{N+\frac{1}{2}}^{m+1}}\right)+\sigma'^{,m+1}_{e,N+\frac{1}{2}}\left(\frac{\partial f_{bk,N+\frac{1}{2}}^{m+1}}{\partial \phi_{N+\frac{1}{2}}^{m+1}}\right)\right]-f_{bk,N+\frac{1}{2}}^{m+1}\sigma'^{,m+1}_{e,N+\frac{1}{2}}(A_5 g)}{A_5^2 g^2\left(\phi_{N+\frac{1}{2}}^{m+1}\right)^2}\right] \tag{B.88}$$

$$\sigma'^{,m+1}_{e,N+\frac{1}{2}} = \begin{cases} 0, \ \phi_{N+\frac{1}{2}}^{m+1} \le \phi_c = 0.23; & \frac{\partial \sigma'^{,m+1}_{e,N+\frac{1}{2}}}{\partial \phi_{N+\frac{1}{2}}^{m+1}} = 0 \\ A_3 A_4 e^{A_4 \phi_{N+\frac{1}{2}}^{m+1}}, \ \phi_{N+\frac{1}{2}}^{m+1} > \phi_c; & \frac{\partial \sigma'^{,m+1}_{e,N+\frac{1}{2}}}{\partial \phi_{N+\frac{1}{2}}^{m+1}} = A_3 A_4^2 e^{A_4 \phi_{N+\frac{1}{2}}^{m+1}} \end{cases} \tag{B.89}$$

$$\frac{\partial a_{N-\frac{1}{2}}^{m+1}}{\partial \phi_{N}^{m+1}} = \frac{\partial a_{N-\frac{1}{2}}^{m+1}}{\partial \phi_{N-\frac{1}{2}}^{m+1}} \times \frac{\partial \phi_{N-\frac{1}{2}}^{m+1}}{\partial \phi_{N}^{m+1}} \tag{B.90}$$

$$\frac{\partial a_{N-\frac{1}{2}}^{m+1}}{\partial \phi_{N-\frac{1}{2}}^{m+1}} = -\left[\frac{A_5 g \phi_{N-\frac{1}{2}}^{m+1}\left[f_{bk,N-\frac{1}{2}}^{m+1}\left(\frac{\partial \sigma'^{,m+1}_{e,N-\frac{1}{2}}}{\partial \phi_{N-\frac{1}{2}}^{m+1}}\right)+\sigma'^{,m+1}_{e,N-\frac{1}{2}}\left(\frac{\partial f_{bk,N-\frac{1}{2}}^{m+1}}{\partial \phi_{N-\frac{1}{2}}^{m+1}}\right)\right]-f_{bk,N-\frac{1}{2}}^{m+1}\sigma'^{,m+1}_{e,N-\frac{1}{2}}(A_5 g)}{A_5^2 g^2\left(\phi_{N-\frac{1}{2}}^{m+1}\right)^2}\right] \tag{B.91}$$

$$\sigma'^{,m+1}_{e,N-\frac{1}{2}} = \begin{cases} 0, \ \phi_{N-\frac{1}{2}}^{m+1} \le \phi_c = 0.23; & \frac{\partial \sigma'^{,m+1}_{e,N-\frac{1}{2}}}{\partial \phi_{N-\frac{1}{2}}^{m+1}} = 0 \\ A_3 A_4 e^{A_4 \phi_{N-\frac{1}{2}}^{m+1}}, \ \phi_{N-\frac{1}{2}}^{m+1} > \phi_c; & \frac{\partial \sigma'^{,m+1}_{e,N-\frac{1}{2}}}{\partial \phi_{N-\frac{1}{2}}^{m+1}} = A_3 A_4^2 e^{A_4 \phi_{N-\frac{1}{2}}^{m+1}} \end{cases} \tag{B.92}$$

$$\frac{\partial f_{bk,N-\frac{1}{2}}^{m+1}}{\partial \phi_{N-1}^{m+1}} = \frac{\partial f_{bk,N-\frac{1}{2}}^{m+1}}{\partial \phi_{N-\frac{1}{2}}^{m+1}} \times \frac{\partial \phi_{N-\frac{1}{2}}^{m+1}}{\partial \phi_{N-1}^{m+1}} \tag{B.93}$$

$$\frac{\partial \phi_{N-\frac{1}{2}}^{m+1}}{\partial \phi_{N-1}^{m+1}} = \frac{1}{2} \tag{B.94}$$

$$\frac{\partial a_{N-\frac{1}{2}}^{m+1}}{\partial \phi_{N-1}^{m+1}} = \frac{\partial a_{N-\frac{1}{2}}^{m+1}}{\partial \phi_{N-\frac{1}{2}}^{m+1}} \times \frac{\partial \phi_{N-\frac{1}{2}}^{m+1}}{\partial \phi_{N-1}^{m+1}} \tag{B.95}$$

Similarly, the elements of the Jacobian matrix from blocks 2 – (N-1) is evaluated as:

$$\frac{\partial f_i^{m+1}}{\partial \phi_i^{m+1}} = 1 + \frac{\Delta t}{\Delta z}\left(\frac{\partial f_{bk,i+\frac{1}{2}}^{m+1}}{\partial \phi_i^{m+1}} - \frac{\partial f_{bk,i-\frac{1}{2}}^{m+1}}{\partial \phi_i^{m+1}}\right) - \frac{\Delta t}{\Delta z^2}\left[a_{i+\frac{1}{2}}^{m+1}(-1) + \left(\phi_{i+1}^{m+1} - \phi_i^{m+1}\right)\frac{\partial a_{i+\frac{1}{2}}^{m+1}}{\partial \phi_i^{m+1}} - \right.$$

$$\left. a_{i-\frac{1}{2}}^{m+1}(1) - \left(\phi_i^{m+1} - \phi_{i-1}^{m+1}\right)\frac{\partial a_{i-\frac{1}{2}}^{m+1}}{\partial \phi_i^{m+1}}\right] \tag{B.96}$$

$$\frac{\partial f_i^{m+1}}{\partial \phi_{i+1}^{m+1}} = \frac{\Delta t}{\Delta z}\left(\frac{\partial f_{bk,i+\frac{1}{2}}^{m+1}}{\partial \phi_{i+1}^{m+1}} - \cancel{\frac{\partial f_{bk,i-\frac{1}{2}}^{m+1}}{\partial \phi_{i+1}^{m+1}}}^{=0}\right) - \frac{\Delta t}{\Delta z^2}\left[a_{i+\frac{1}{2}}^{m+1}(1) + \left(\phi_{i+1}^{m+1} - \phi_i^{m+1}\right)\frac{\partial a_{i+\frac{1}{2}}^{m+1}}{\partial \phi_{i+1}^{m+1}} - 0 - 0\right] \tag{B.97}$$

Equation B.97 becomes:

$$\frac{\partial f_i^{m+1}}{\partial \phi_{i+1}^{m+1}} = \frac{\Delta t}{\Delta z}\left(\frac{\partial f_{bk,i+\frac{1}{2}}^{m+1}}{\partial \phi_{i+1}^{m+1}}\right) - \frac{\Delta t}{\Delta z^2}\left[a_{i+\frac{1}{2}}^{m+1} + \left(\phi_{i+1}^{m+1} - \phi_i^{m+1}\right)\frac{\partial a_{i+\frac{1}{2}}^{m+1}}{\partial \phi_{i+1}^{m+1}}\right] \tag{B.98}$$

$$\frac{\partial f_i^{m+1}}{\partial \phi_{i-1}^{m+1}} = \frac{\Delta t}{\Delta z}\left(\cancel{\frac{\partial f_{bk,i+\frac{1}{2}}^{m+1}}{\partial \phi_{i-1}^{m+1}}}^{=0} - \frac{\partial f_{bk,i-\frac{1}{2}}^{m+1}}{\partial \phi_{i-1}^{m+1}}\right) - \frac{\Delta t}{\Delta z^2}\left[0 + 0 - a_{i-\frac{1}{2}}^{m+1}(-1) - (\phi_i^{m+1} - \phi_{i-1}^{m+1})\frac{\partial a_{i-\frac{1}{2}}^{m+1}}{\partial \phi_{i-1}^{m+1}}\right] \tag{B.99}$$

Equation B.99 becomes:

$$\frac{\partial f_i^{m+1}}{\partial \phi_{i-1}^{m+1}} = -\frac{\Delta t}{\Delta z}\left(\frac{\partial f_{bk,i-\frac{1}{2}}^{m+1}}{\partial \phi_{i-1}^{m+1}}\right) - \frac{\Delta t}{\Delta z^2}\left[a_{i-\frac{1}{2}}^{m+1} - \left(\phi_i^{m+1} - \phi_{i-1}^{m+1}\right)\frac{\partial a_{i-\frac{1}{2}}^{m+1}}{\partial \phi_{i-1}^{m+1}}\right] \tag{B.100}$$

The derivation of each differential in the elements of the Jacobian matrix from blocks 2 – (N-1) is shown below:

$$\frac{\partial f_{bk,i+\frac{1}{2}}^{m+1}}{\partial \phi_i^{m+1}} = \frac{\partial f_{bk,i+\frac{1}{2}}^{m+1}}{\partial \phi_{i+\frac{1}{2}}^{m+1}} \times \frac{\partial \phi_{i+\frac{1}{2}}^{m+1}}{\partial \phi_i^{m+1}} \tag{B.101}$$

$$\frac{\partial f_{bk,i+\frac{1}{2}}^{m+1}}{\partial \phi_{i+\frac{1}{2}}^{m+1}} = -A_1 A_2 \phi_{i+\frac{1}{2}}^{m+1} \left(1 - \phi_{i+\frac{1}{2}}^{m+1}\right)^{A_2 - 1} + A_1 \left(1 - \phi_{i+\frac{1}{2}}^{m+1}\right)^{A_2} \tag{B.102}$$

$$\frac{\partial \phi_{i+\frac{1}{2}}^{m+1}}{\partial \phi_i^{m+1}} = \frac{1}{2} \tag{B.103}$$

$$\frac{\partial f_{bk,i-\frac{1}{2}}^{m+1}}{\partial \phi_i^{m+1}} = \frac{\partial f_{bk,i-\frac{1}{2}}^{m+1}}{\partial \phi_{i-\frac{1}{2}}^{m+1}} \times \frac{\partial \phi_{i-\frac{1}{2}}^{m+1}}{\partial \phi_i^{m+1}} \tag{B.104}$$

$$\frac{\partial f_{bk,i-\frac{1}{2}}^{m+1}}{\partial \phi_{i-\frac{1}{2}}^{m+1}} = -A_1 A_2 \phi_{i-\frac{1}{2}}^{m+1} \left(1 - \phi_{i-\frac{1}{2}}^{m+1}\right)^{A_2 - 1} + A_1 \left(1 - \phi_{i-\frac{1}{2}}^{m+1}\right)^{A_2} \tag{B.105}$$

$$\frac{\partial \phi_{i-\frac{1}{2}}^{m+1}}{\partial \phi_i^{m+1}} = \frac{1}{2} \tag{B.106}$$

$$\frac{\partial a_{i+\frac{1}{2}}^{m+1}}{\partial \phi_i^{m+1}} = \frac{\partial a_{i+\frac{1}{2}}^{m+1}}{\partial \phi_{i+\frac{1}{2}}^{m+1}} \times \frac{\partial \phi_{i+\frac{1}{2}}^{m+1}}{\partial \phi_i^{m+1}} \tag{B.107}$$

$$\frac{\partial a_{i+\frac{1}{2}}^{m+1}}{\partial \phi_{i+\frac{1}{2}}^{m+1}} = -\left[\frac{A_5 g \phi_{i+\frac{1}{2}}^{m+1}\left[f_{bk,i+\frac{1}{2}}^{m+1}\left(\frac{\partial \sigma'^{,m+1}_{e,i+\frac{1}{2}}}{\partial \phi_{i+\frac{1}{2}}^{m+1}}\right) + \sigma'^{,m+1}_{e,i+\frac{1}{2}}\left(\frac{\partial f_{bk,i+\frac{1}{2}}^{m+1}}{\partial \phi_{i+\frac{1}{2}}^{m+1}}\right)\right] - f_{bk,i+\frac{1}{2}}^{m+1} \sigma'^{,m+1}_{e,i+\frac{1}{2}} (A_5 g)}{A_5^2 g^2 \left(\phi_{i+\frac{1}{2}}^{m+1}\right)^2}\right] \tag{B.108}$$

$$\sigma'^{,m+1}_{e,i+\frac{1}{2}} = \begin{cases} 0, \ \phi_{i+\frac{1}{2}}^{m+1} \le \phi_c = 0.23; & \frac{\partial \sigma'^{,m+1}_{e,i+\frac{1}{2}}}{\partial \phi_{i+\frac{1}{2}}^{m+1}} = 0 \\ A_3 A_4 e^{A_4 \phi_{i+\frac{1}{2}}^{m+1}}, \ \phi_{i+\frac{1}{2}}^{m+1} > \phi_c; & \frac{\partial \sigma'^{,m+1}_{e,i+\frac{1}{2}}}{\partial \phi_{i+\frac{1}{2}}^{m+1}} = A_3 A_4^2 e^{A_4 \phi_{i+\frac{1}{2}}^{m+1}} \end{cases} \tag{B.109}$$

$$\frac{\partial a_{i-\frac{1}{2}}^{m+1}}{\partial \phi_i^{m+1}} = \frac{\partial a_{i-\frac{1}{2}}^{m+1}}{\partial \phi_{i-\frac{1}{2}}^{m+1}} \times \frac{\partial \phi_{i-\frac{1}{2}}^{m+1}}{\partial \phi_i^{m+1}} \tag{B.110}$$

$$\frac{\partial a_{i-\frac{1}{2}}^{m+1}}{\partial \phi_{i-\frac{1}{2}}^{m+1}} = -\left[\frac{A_5 g \phi_{i-\frac{1}{2}}^{m+1}\left[f_{bk,i-\frac{1}{2}}^{m+1}\left(\frac{\partial \sigma'^{,m+1}_{e,i-\frac{1}{2}}}{\partial \phi_{i-\frac{1}{2}}^{m+1}}\right)+\sigma'^{,m+1}_{e,i-\frac{1}{2}}\left(\frac{\partial f_{bk,i-\frac{1}{2}}^{m+1}}{\partial \phi_{i-\frac{1}{2}}^{m+1}}\right)\right]-f_{bk,i-\frac{1}{2}}^{m+1}\sigma'^{,m+1}_{e,i-\frac{1}{2}}(A_5 g)}{A_5^2 g^2\left(\phi_{i-\frac{1}{2}}^{m+1}\right)^2}\right] \tag{B.111}$$

$$\sigma'^{,m+1}_{e,i-\frac{1}{2}} = \begin{cases} 0, \ \phi_{i-\frac{1}{2}}^{m+1} \le \phi_c = 0.23; & \frac{\partial \sigma'^{,m+1}_{e,i-\frac{1}{2}}}{\partial \phi_{i-\frac{1}{2}}^{m+1}} = 0 \\ A_3 A_4 e^{A_4 \phi_{i-\frac{1}{2}}^{m+1}}, \ \phi_{i-\frac{1}{2}}^{m+1} > \phi_c; & \frac{\partial \sigma'^{,m+1}_{e,i-\frac{1}{2}}}{\partial \phi_{i-\frac{1}{2}}^{m+1}} = A_3 A_4^2 e^{A_4 \phi_{i-\frac{1}{2}}^{m+1}} \end{cases} \tag{B.112}$$

$$\frac{\partial f_{bk,i+\frac{1}{2}}^{m+1}}{\partial \phi_{i+1}^{m+1}} = \frac{\partial f_{bk,i+\frac{1}{2}}^{m+1}}{\partial \phi_{i+\frac{1}{2}}^{m+1}} \times \frac{\partial \phi_{i+\frac{1}{2}}^{m+1}}{\partial \phi_{i+1}^{m+1}} \tag{B.113}$$

$$\frac{\partial \phi_{i+\frac{1}{2}}^{m+1}}{\partial \phi_{i+1}^{m+1}} = \frac{1}{2} \tag{B.114}$$

$$\frac{\partial a_{i+\frac{1}{2}}^{m+1}}{\partial \phi_{i+1}^{m+1}} = \frac{\partial a_{i+\frac{1}{2}}^{m+1}}{\partial \phi_{i+\frac{1}{2}}^{m+1}} \times \frac{\partial \phi_{i+\frac{1}{2}}^{m+1}}{\partial \phi_{i+1}^{m+1}} \tag{B.115}$$

$$\frac{\partial f_{bk,i-\frac{1}{2}}^{m+1}}{\partial \phi_{i-1}^{m+1}} = \frac{\partial f_{bk,i-\frac{1}{2}}^{m+1}}{\partial \phi_{i-\frac{1}{2}}^{m+1}} \times \frac{\partial \phi_{i-\frac{1}{2}}^{m+1}}{\partial \phi_{i-1}^{m+1}} \tag{B.116}$$

$$\frac{\partial \phi_{i-\frac{1}{2}}^{m+1}}{\partial \phi_{i-1}^{m+1}} = \frac{1}{2} \tag{B.117}$$

$$\frac{\partial a_{i-\frac{1}{2}}^{m+1}}{\partial \phi_{i-1}^{m+1}} = \frac{\partial a_{i-\frac{1}{2}}^{m+1}}{\partial \phi_{i-\frac{1}{2}}^{m+1}} \times \frac{\partial \phi_{i-\frac{1}{2}}^{m+1}}{\partial \phi_{i-1}^{m+1}} \tag{B.118}$$

Appendix C: Implementation of Numerical Solution in MATLAB

Having completed the discretization and computational processes, the equations are programmed in MATLAB. To obtain ϕ_0^{m+1} when $\phi_{\frac{1}{2}}^{m+1} > \phi_c$, the Newton-Raphson method is executed with Eqs. B.20 and B.21 as presented below:

$$\phi_0^{m+1} = (\phi_0^{m+1})_{Guess} - \frac{f_{\phi_0}^{m+1}}{\left(\frac{\partial f_{\phi_0}^{m+1}}{\partial \phi_0^{m+1}}\right)} \tag{C.1}$$

On the right-hand side of Eq. C.1, ϕ_0^{m+1} is replaced with $(\phi_0^{m+1})_{Guess}$. Iteration is repeated until convergence is achieved.

Similarly, to obtain $\frac{\partial \phi_0^{m+1}}{\partial \phi_1^{m+1}}$ when $\phi_{\frac{1}{2}}^{m+1} > \phi_c$, the Newton-Raphson method is implemented with Eqs. B.69 and B.70 as shown below:

$$\frac{\partial \phi_0^{m+1}}{\partial \phi_1^{m+1}} = \left(\frac{\partial \phi_0^{m+1}}{\partial \phi_1^{m+1}}\right)_{Guess} - \frac{\left(f \frac{\partial \phi_0^{m+1}}{\partial \phi_1^{m+1}}\right)}{\left(\frac{\partial f \frac{\partial \phi_0^{m+1}}{\partial \phi_1^{m+1}}}{\partial \frac{\partial \phi_0^{m+1}}{\partial \phi_1^{m+1}}}\right)} \tag{C.2}$$

On the right-hand side of Eq. C.2, $\frac{\partial \phi_0^{m+1}}{\partial \phi_1^{m+1}}$ is replaced with $\left(\frac{\partial \phi_0^{m+1}}{\partial \phi_1^{m+1}}\right)_{Guess}$. Iteration is repeated until convergence is achieved.

The residual functions for all the blocks are assembled into a matrix as displayed below:

$$F_i = \begin{bmatrix} f_N^{m+1} \\ f_{N-1}^{m+1} \\ f_{N-2}^{m+1} \\ \vdots \\ \vdots \\ f_4^{m+1} \\ f_3^{m+1} \\ f_2^{m+1} \\ f_1^{m+1} \end{bmatrix} \tag{C.3}$$

where F_i is matrix of residual functions.

The elements of the Jacobian matrix from all the blocks are assembled as shown below:

$$J = \begin{bmatrix} \frac{\partial f_N^{m+1}}{\partial \phi_N^{m+1}} & \frac{\partial f_N^{m+1}}{\partial \phi_{N-1}^{m+1}} & 0 & 0 & 0 & 0 & 0 & 0 & 0 \\ \frac{\partial f_{N-1}^{m+1}}{\partial \phi_N^{m+1}} & \frac{\partial f_{N-1}^{m+1}}{\partial \phi_{N-1}^{m+1}} & \frac{\partial f_{N-1}^{m+1}}{\partial \phi_{N-2}^{m+1}} & 0 & 0 & 0 & 0 & 0 & 0 \\ 0 & \frac{\partial f_{N-2}^{m+1}}{\partial \phi_{N-1}^{m+1}} & \frac{\partial f_{N-2}^{m+1}}{\partial \phi_{N-2}^{m+1}} & \frac{\partial f_{N-2}^{m+1}}{\partial \phi_{N-3}^{m+1}} & 0 & 0 & 0 & 0 & 0 \\ 0 & 0 & \vdots & \vdots & \vdots & 0 & 0 & 0 & 0 \\ 0 & 0 & 0 & \vdots & \vdots & \vdots & 0 & 0 & 0 \\ 0 & 0 & 0 & 0 & \frac{\partial f_4^{m+1}}{\partial \phi_5^{m+1}} & \frac{\partial f_4^{m+1}}{\partial \phi_4^{m+1}} & \frac{\partial f_4^{m+1}}{\partial \phi_3^{m+1}} & 0 & 0 \\ 0 & 0 & 0 & 0 & 0 & \frac{\partial f_3^{m+1}}{\partial \phi_4^{m+1}} & \frac{\partial f_3^{m+1}}{\partial \phi_3^{m+1}} & \frac{\partial f_3^{m+1}}{\partial \phi_2^{m+1}} & 0 \\ 0 & 0 & 0 & 0 & 0 & 0 & \frac{\partial f_2^{m+1}}{\partial \phi_3^{m+1}} & \frac{\partial f_2^{m+1}}{\partial \phi_2^{m+1}} & \frac{\partial f_2^{m+1}}{\partial \phi_1^{m+1}} \\ 0 & 0 & 0 & 0 & 0 & 0 & 0 & \frac{\partial f_1^{m+1}}{\partial \phi_2^{m+1}} & \frac{\partial f_1^{m+1}}{\partial \phi_1^{m+1}} \end{bmatrix} \tag{C.4}$$

where J is Jacobian matrix. This J is an $N \times N$ matrix, and also, it is a tridiagonal matrix because this is a one-dimensional problem.

To obtain ϕ_i^{m+1}, the Newton-Raphson method is implemented as presented below:

$$\begin{bmatrix} \phi_N^{m+1} \\ \phi_{N-1}^{m+1} \\ \phi_{N-2}^{m+1} \\ \vdots \\ \vdots \\ \phi_4^{m+1} \\ \phi_3^{m+1} \\ \phi_2^{m+1} \\ \phi_1^{m+1} \end{bmatrix} = \begin{bmatrix} \phi_N^{m+1} \\ \phi_{N-1}^{m+1} \\ \phi_{N-2}^{m+1} \\ \vdots \\ \vdots \\ \phi_4^{m+1} \\ \phi_3^{m+1} \\ \phi_2^{m+1} \\ \phi_1^{m+1} \end{bmatrix}_{Guess} - J^{-1} \begin{bmatrix} f_N^{m+1} \\ f_{N-1}^{m+1} \\ f_{N-2}^{m+1} \\ \vdots \\ \vdots \\ f_4^{m+1} \\ f_3^{m+1} \\ f_2^{m+1} \\ f_1^{m+1} \end{bmatrix} \tag{C.5}$$

where J^{-1} is the inverse of the Jacobian matrix. On the right-hand side of Eq. C.5, ϕ_i^{m+1} is replaced with $(\phi_i^{m+1})_{Guess}$. Iteration is repeated until convergence is achieved.